ISBN 978-82-326-1020-4 (printed version)
ISBN 978-82-326-1021-1 (electronic version)
ISSN 1503-8181

Doctoral theses at NTNU, 2015:182

Arturo Jesús Ortega Malca

Dynamic Response of Flexible Risers due to Unsteady Slug Flow

Doctoral Thesis

Arturo Jesús Ortega Malca

Doctoral theses at NTNU, 2015:182

NTNU
Norwegian University of
Science and Technology
Faculty of Engineering
Science and Technology
Department of MarineTechnology

NTNU – Trondheim
Norwegian University of
Science and Technology

NTNU – Trondheim
Norwegian University of
Science and Technology

NTNU

Arturo Jesús Ortega Malca

Dynamic Response of Flexible Risers due to Unsteady Slug Flow

Thesis for the degree of Philosophiae Doctor

Trondheim, September 2015

Norwegian University of Science and Technology

NTNU – Trondheim
Norwegian University of
Science and Technology

NTNU
Norwegian University of Science and Technology

Thesis for the degree of Philosophiae Doctor

ISBN 978-82-326-1020-4 (printed version)
ISBN 978-82-326-1021-1 (electronic version)
ISSN 1503-8181

Doctoral theses at NTNU, 2015:182

Printed by Skipnes Kommunikasjon as

I want to dedicate this work to my daughters Martha Camila and Romina Victoria, and also to my wife Pilar for the love and patience they gave me during these years as a PhD student.

Abstract

In this work the influence of unsteady slug flow on the dynamic response of flexible risers is analysed using a computational tool consisting of one program for prediction of slug flow development, and another program for calculation of dynamic response of the riser. Both programs apply a time integration method, and since slug flow leads to dynamic response of the riser, and riser dynamics influences slug flow behaviour, the two codes exchange feedback of information during the integration process. Information exchange is established by building a computer federation of programs based on High Level Architecture (HLA). The federation is composed of two standalone in-house computer codes. The first one is a two-phase flow code which simulates unsteady slug flow through pipes and risers using a Lagrangian tracking model. The second one is a program for static and dynamic global riser analysis based on a two dimensional non-linear finite element formulation. Using the HLA rules, a communication interface was built, so the two programs are able to perform synchronized time integration with mutual feedback of information for each time step.

The slug flow – riser dynamics interaction is a complex problem. The riser response depends on the slug flow behaviour, and the slug flow development is influenced by the riser configuration. Displacement response of the riser and the influence of them on the slug flow development have been studied for different flexible riser configurations carrying different liquid and gas flow rates. Results have shown the importance of using complete mathematical models for each phenomena and the importance of a strong interface of communication in order to predict a realistic behaviour of the slug flow - riser dynamics interaction. Analysis on the influence of the slug flow on the effective tension and bending moment of a flexible riser was studied showing increment of axial and bending stresses. Moreover, the simulations have demonstrated the importance to use a full non-linear finite element model for the riser dynamics, because the riser response influence strongly on the slug flow behaviour. Finally, the numerical results were validated against experimental data showing a reasonable agreement.

Preface

This thesis is submitted to the Norwegian University of Science and Technology (NTNU) for partial fulfilment of the requirements for the degree of philosophiae doctor.

This doctoral work has been performed at the Department of Marine Technology, NTNU, Trondheim, with Professor Carl Martin Larsen as main supervisor and with Professor Ole Jørgen Nydal as co-supervisor.

The financial support from the Research Council of Norway through Centre for Ships and Ocean Structures (CeSOS) is gratefully acknowledged.

Acknowledgements

I want to acknowledge my supervisor Professor Carl Martin Larsen for his guidance and the confidence given to me for carrying out this project. Professor Carl introduced me into the world of the fluid-structure interaction and put me in the front of this *Quixotism*.

Also I want to express my gratitude to my co-supervisor Professor Ole Jørgen Nydal for reinforcing my knowledge on multiphase flow and for allowing me the use his two-phase flow code.

Furthermore I feel grateful to my PhD colleague: Ausberto Rivera for his orientation on riser dynamics, finite element and for the long evening discussions that always were fruitful. Also I want to say thanks to classmates Tor Kjeldby for helping me to figure out the flow code, and to Ondrej Novak for adjusting the visualisation program.

Contents

List of Figures

List of Tables

Abbreviations

CFD	Computational Fluid Dynamic
CFL	Courant, Friedrichs and Lewy number
DEQ	Dynamic Equilibrium Equation
FEM	Finite Element Method
FIV	Flow Induced Vibration
FSI	Fluid – Structure Interaction
FVM	Finite Volume Method
GRA	Global Riser Analysis
HLA	High Level Architecture
MWL	Mean Water Level
OOP	Object Oriented Programming
RTI	Run Time Infrastructure
TDP	Touch down point
TFM	Two-Fluid Model

1. Introduction

Flexible risers are widely used for offshore oil and gas production. New petroleum reservoirs are being discovered in deeper water, requiring the construction of longer risers. Thus, this type of riser is becoming more vulnerable under environmental loads. The environmental loads can come from currents, waves and phenomena such as vortex-induced vibration (VIV). In addition to the environmental loads, flexible risers can also suffer loads from marine operations such as offset and vessel motion. The effects of these loads on the riser structure and methods to mitigate the damage have been thoroughly studied for years. However, another important load, which comes from a phenomenon called slug flow, suffers from a lack of information and investigation.

Slug flow is a transient two-phase flow pattern that can be generated inside the flexible riser during oil – gas production due to hydrodynamic instabilities generated at the border of the gas and liquid phase or by liquid accumulation at the deepest point of the flexible riser. The more common slug flow patterns which appear during an oil and gas production are *hydrodynamic slugging* and *severe slugging*.

Slug flow is characterized as a random and dynamic phenomenon where liquid plugs (slugs) interspersed with gas bubbles travel through the flexible riser. These generated slugs and bubbles have different sizes and velocities, which can also change as they travel through the flexible riser. This unsteady behavior of the slug flow imposes dynamic forces on the riser structure. These forces are mainly due to the variable mass distribution of the liquid and gas phases, which will generate a variable distribution of gravitational forces. As the riser is located inside the sea, these variable gravitational forces are represented by a variable change in the effective weight. Additionally, the changes in velocity direction of the slugs and bubbles in the bends of the riser produce a centripetal acceleration. This acceleration imposed on the fluid particles generates centripetal force, so the riser wall reacts to this force as a centrifugal force. The whole flexible riser acts against these forces (forces from the slug flow) increasing the wall

tension and bending moment, originating additional axial and bending stresses in the riser structure.

The development of slug flow is highly influenced by the flexible riser geometrical configuration where it is flowing. The physical characteristics of this two-phase flow, i.e., velocity, pressure, shape and density, come from the mass, momentum and energy fluid balance. Thus, time variation on the riser shape means change in the fluid momentum balance due to the change in position of the fluid mass inside the riser. This change in the internal fluid gravitational forces will influence the velocity and internal pressure of the two-phase flow, originating a new two-phase flow mass distribution along the riser.

The slug flow – flexible riser problem is categorized as a fluid-structure interaction (FSI) phenomenon. The two-phase flow imposes loads on the riser structure, and the response of the riser influences the development of the slug flow. The slug flow and riser dynamics is characterized as a complex and sensitive phenomenon. Mathematically, the slug flow is modeled by the fluid conservation equations, and in turn, the riser dynamics is ruled by the dynamic equilibrium equation. The equations of these models are characterized for being high non-linear differential equations.

Two alternatives are available to numerically simulate this fluid-structure interaction. The first is to create a monolithic computer program to implement the mathematical model of each phenomenon. The overall complexity, however, would become high, and further development of the program would need a close cooperation between the slug flow and the riser dynamics groups.

Alternatively, the mathematical model of each phenomenon could be implemented into independent, stand-alone programs, one to simulate the slug flow development and another to simulate the riser dynamics. By keeping the programs apart, each program might be developed independently This methodology allows the easier implementation of complex mathematical models and facilitates its later improvement, as the updating of one computer program would not influence the other one as long as the data flow between the programs remains unchanged. A key point in this methodology is the mutual feedback of information, which requires the programs to work concurrently and exchanging information along the time domain. This last alternative has been used in the development of this work. Thus, two in-house computer

programs have been connected by a communication interface. One program simulates the slug flow development, and the other predicts the riser dynamics. The variables that travel from one program to the other follow a series of rules defined by the communication interface.

This thesis is outlined as follows. First, the current state of the art based on previous investigation will be discussed, with highlights and commentary on its achievements. Next, the scope of this work will be described. An integrated analysis methodology has been developed to construct the communication interface between the two computer programs. In chapter 4 the theory on the two-phase flow and the slug flow pattern will be explained, together with a description of the mathematical model used to simulate this two-phase flow pattern numerically. Chapter 5 will address the validation of the riser dynamics code used for this thesis against recognized commercial software. Next, the communication methodology used to build the communication interface will be described in its own chapter. Then, key test cases regarding riser dynamics induced by slug flow are presented and the results analyzed. These cases are as follows:

1. Analysis of the effective tension variation due to a transient two-phase flow.
2. Analysis of linear and non-linear formulations of coupled systems.
3. Validation of the numerical approach against a laboratory-scale model.

Finally, the conclusions produced by this work and suggestions for further works are presented.

2. State of the Art

Despite the importance of analyzing the response of flexible risers originated by slug flow, only a few significant works have been found in the scientific literature.

One of the pioneer investigations on vibrations generated by unsteady two-phase flow was performed by Yih and Griffith [1]. Unsteady components of the momentum flux in a two-phase flow were measured by a beam-tee system. The effects of the average flow velocity, volumetric quality, system pressure, flow channel size and geometry on the unsteady momentum fluxes were observed. It was found that the fluctuation of momentum fluxes is important only in the low frequency range. The maximum values of unsteady momentum fluxes appeared in either the high void slug flow or the low annular flow regime.

A numerical study of a "plug" slug flow traveling through a hose in a catenary shape was conducted by Fylling et al. [2]. The "plug" slug travels along the riser with constant velocity and length. The dynamic equilibrium equation was solved considering the mass distribution, gravity and centripetal force generated by the travelling slug. However, the model did not consider the influence of the hose response on the slug development. In addition, slug "plug" travel with constant speed and length can be considered unrealistic or too conservative.

A general mathematical model involving flow and riser response was developed by Patel and Seyed [3]. Their numerical investigation in a flexible pipe showed a large variation in axial tension, so additional stress generated by the slug flow was predicted. However, in that work the slug flow was considered as a steady state flow, which is unrealistic. The loads against the riser came from the slug flow momentum, and a mixture flow density with sinusoidal variation was also assumed. In addition, the influence of the riser response on the slug flow behavior was not considered.

A series of measurements were performed by Riverin et al. [4]. These authors analyzed the effect of fluctuating two-phase air-water mixture forces on bends and tees. The work proposes correlations that relate the characteristics of the forces to the piping

geometry configuration and the two-phase flow parameters. Additionally, using a momentum flow balance, correlations regarding the two-phase flow void fraction and the magnitude of the forces were derived. Even when the two-phase flow patterns presented in the experiment were churn and bubbly, the correlations considering a slug flow were obtained.

An experimental investigation of the dynamic motion of a flexible riser considering an internal slug flow was conducted by Valdivia et al. [5]. A laboratory scale model was built based on a steel catenary riser prototype. Riser displacements and top tensions were recorded, and a numerical comparison was performed. A numerical model based in the work of Patel and Seyed [3] (steady state and sinusoidal slug density variation) was implemented in a global riser dynamic program. The validation showed that the simulation predicted periodic deformations and smaller top tension of the riser.

An analysis of experimental measurements was performed by Gama et al. [6]. Accelerations of pipe responses at the bends due to a travelling two-phase flow along L and U pipe configurations were recorded. The results indicated that the RMS values of the accelerations have a quadratic trend regarding the two-phase flow mixture velocity for different volume fractions.

Vibrations induced in a jumper due to an unsteady two-phase flow were numerically investigated by Pontaza and Menon [7]. This approach treated the question only as a flow induced-vibration problem. The dominant frequencies associated with its natural mode of vibration were determined. However, this analysis is uncoupled. The flow simulation is performed first, and then the time history forces are calculated and transferred to a finite element model for the structural response analysis. A 3D CFD model was used for the two-phase flow analysis, and a beam model was used for the structural analysis. The 3D models are also limited to short span risers.

Measurements and video recordings of the response of a flexible plastic hose undergoing severe slugging were performed by Ita [8]. Air and water with different flow rates were supplied through a catenary and lazy wave configurations in a laboratory scale facility. The videos show the deformation of the hose due to the liquid accumulation at the deepest zone, followed by the reformation of the hose configuration from the blow-out.

A series of measurements of riser vibrations induced by severe slugging was reported by Pessanha and et al. [9]. To reproduce the severe slugging phenomenon on a laboratory scale, a piping configuration consisting of leaning, horizontal and vertical pipes were set up. Time series responses of the accelerations of the leaning pipe are reported for different pressure discharges and pump rotations during blow-out and for liquid accumulation in the deepest region. The work reports that the highest vibrations generated for severe slugging are during the blow-out.

Currently, sophisticated software programs for global riser analysis (GRA) are available for the oil and gas industry. Most commercial software programs have a module for riser response by slug flow. The model implemented in these is similar to the model of Fylling et al. [2]. Similarly, programs that simulate multiphase flow are also available in the commercial market. However, these last programs are oriented to oil and gas production and flow assurance, with no relationship to riser dynamics.

3. Scope of work

The purpose of this work is to develop a system for coupled analysis of slug flow and riser dynamics by constructing a system for communication between stand-alone programs for slug flow and riser dynamics.

To create the system of systems, it was necessary to conduct a study of the set of equations to be sure that the mathematical models of the riser dynamics and the two-phase flow can represent dynamic flow through pipes with dynamic response.

Figure 1 shows a fluid particle flowing through a curved pipe segment. The change in flow direction means that a fluid particle will have an acceleration perpendicular to its flow direction, Larsen [10]. This acceleration requires a centripetal force F_n in the same direction, but the pipe will be subject to a resultant force in the opposite direction. This resultant force must be counteracted by an increase in the wall tension, a key result from this type of simulation.

For the case of slug flow, it is necessary to consider the contribution from each flow phase, i.e., liquid and gas, see Equation (1) and (2).

$$F_n = F_{n_l} + F_{n_g}; \qquad F_{n_k} = M_k a_{c_k}; \qquad a_{c_k} = \frac{u_k^2}{R} \tag{1}$$

$$W = W_l + W_g; \qquad W_k = M_k g \tag{2}$$

In these two equations F_n represents the normal equivalent force or centripetal force, and a_c stands for the centripetal acceleration. M, u and W are the mass, velocity and weight of the particle, respectively, R represents the radius of curvature, and g is the gravitational acceleration. Finally, the suffix k refers to the liquid l and gas g phases.

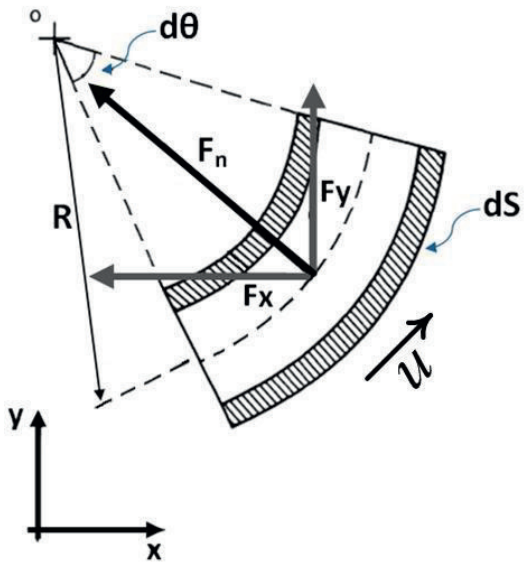

Figure 1. Fluid particle travelling along a pipe segment

3.1 Update of The Riser Dynamics Model

To simulate the riser dynamic response, an *in-house* code was used. This code considers forces from waves, buoyancy, top tension, riser weight and internal one/two-phase flow. This program can conduct a stepwise numerical integration of a riser subjected to these types of external forces.

Following the finite element formulation, the domain is discretized into elements, each considered as a two-dimensional beam with six degrees of freedom (beam column element).

A fully non-linear finite element formulation of the DEQ was used in which bending and geometric stiffness from tension are considered. The incremental formulation of the dynamic equilibrium equation for a discretized structure using a non-linear finite element method can be expressed by Equation (3), Paz [11].

$$M_{I_k}\Delta\ddot{r}_k + C_{I_k}\Delta\dot{r}_k + K_{I_k}\Delta r_k = F_{k+1}^{e\ *} - F_k^i \tag{3}$$

where k refers to the time step. The parameters $\Delta\ddot{r}, \Delta\dot{r}$ *and* Δr correspond to unknown increments in accelerations, velocities and displacements, respectively. M_I represents

the global structural incremental mass matrix (the average value within a time increment). The current mass matrix M^* accounts for the structural mass, the added mass of the surrounding water and the variable internal liquid and gas masses, see Equation (4).

$$M^* = M_{pipe} + M_{added} + M_l + M_g \tag{4}$$

Similarly, C_I stands for the global structural incremental damping matrix. A Rayleigh damping model is applied. The global structural incremental stiffness matrix K_I handles large displacements and rotations with small axial strains.

F^{e*} represents the time-varying external forces, and Equation (5) shows its vectorial formulation.

$$\vec{F}^{e*} = \sum \vec{F}^{e} + M_l\left(\vec{a}_{c_l} + \vec{g}\right) + M_g\left(\vec{a}_{c_g} + \vec{g}\right) \tag{5}$$

In this relationship, external environmental and operational loads are represented by $\sum F^e$. Contributions from the internal slug flow are represented by the centripetal force $M_k\, a_{ck}$ and by the gravity force $M_k\, g$.

Finally, F^i stands for the internal forces, namely, elastic, damping and inertial.

3.2 The Effective Tension and Effective Weight

The effective tension that affects the geometric stiffness is represented by Equation (6), confer Sparks [12]:

$$T_e = T_w + P_e A_e - P_i A_i - \dot{m}_l u_l - \dot{m}_g u_g \tag{6}$$

where T_w is the true tension (axial stress resultant), and P_e and P_i represent the external and internal pressure, respectively. Similarly, A_e and A_i represent the external and internal cross-sectional areas of the riser, respectively, and $\dot{m}_g$ *and* $\dot{m}_l$ are the gas and liquid mass flow rates, respectively. The direct relationship of the two-phase flow momentum to the effective tension is clear.

An additional important parameter to be considered is the effective weight: see Equation (7).

$$W_e = W_{dry\ pipe} + W_l + W_g - B \tag{7}$$

The first three terms on the right side of the relation represent the weight of the dry pipe and weights of the liquid and the gas phases, respectively. The last term represents the buoyancy: see Equation (8).

$$B = \frac{\pi}{4} D_o^2 \rho_w g \tag{8}$$

In this equation, D_o represents the external diameter and ρ_w is the sea density. The slug flow has an important influence on this parameter due to the transient distribution of the liquid and gas mass flow rate along the riser. The transient distribution of the liquid and gas masses are not considered in the mass matrix for the linear model, but only as variable gravity forces.

3.3 Update of The Two-Phase Flow Model

The fluid momentum equation is given in Equation (9) only as an illustration. For details regarding this equation, please refer to Chapter 4.

$$\begin{aligned} &\frac{\partial (M_k u_k)}{\partial t} + \oint_{A_k} \rho_k (u_k - u_b) u_k \, dS = \cdots \\ &-V_k \frac{\partial p}{\partial x} - M_k \mathrm{g} \cos\varphi \frac{\partial h_{D,l}}{\partial x} + \oint_{A_k} \tau_k \, dS - M_k \mathrm{g} \sin\varphi + \dot{M}_k^s u_k^s \end{aligned} \tag{9}$$

When working with the dynamic response of pipes, the change in pipe inclination affects two terms of the fluid momentum equation. The first is represented by

$$M_k g \cos\varphi \frac{\partial h_{D,l}}{\partial x} \tag{10}$$

which corresponds to the hydrostatic contribution induced by level gradients. The second is the gravity contribution shown in Equation (11):

$$-M_k g \sin\varphi \tag{11}$$

The sign of this term depends on whether it works against or in favor of the flow movements.

As two numerical methods are used in this work, finite element (FEM) and finite volume (FVM), it is necessary to have a procedure to transfer information between the fixed mesh distribution (finite elements) and the dynamic mesh distribution (slug tracking model – finite volume), see Figure 2.

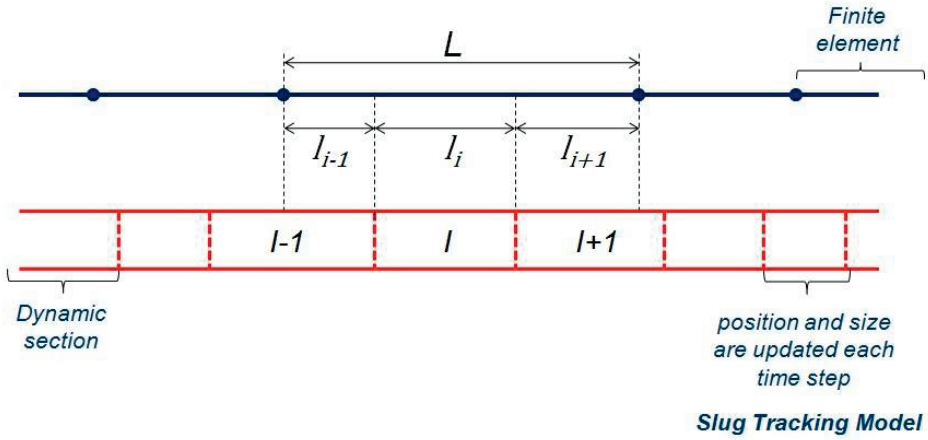

Figure 2. Management of the dynamic and constant mesh distributions

This transfer is accomplished by using a weighted average for the information to be shared. In the case of the liquid holdup, it is as follows:

$$\bar{H} = \frac{\int H dx}{\int dx} \tag{12}$$

3.4 Communication Interface

A communication interface was built to couple the riser dynamics code and the slug flow program using High Level Architecture (HLA). The HLA is a series of rules (open standard IEEE 1516) for distributed simulation systems [13],[14],[15]. It enables the reuse of existing software for new purposes. Computer programs written in different

programming languages can be coupled using this methodology, even if they work under different operating systems. In HLA, several simulation units, called *federates*, are combined to create one large simulation system, called *federation*. The *federation* of this work is depicted in Figure 3.

In this *federation*, the riser dynamics program and slug flow code work as *federates*. The riser dynamics program calculates the riser configuration for each time step, for which purpose it must receive the distribution of masses and velocities of each phase along the riser. On the other side, the slug flow program predicts these distributions for the liquid and gas phases and receives the geometrical configuration of the riser to perform these calculations. Thus, each program is the feedback of the other. All information flows through and is managed by the Run-Time Infrastructure (RTI), which works as an operating system [16]. An RTI from Pitch Technology [17] was used for the communication interface. The HLA allows the use of pre-built programing routines written in C++ for communication. These routines were adapted and linked to each program (*federate*). These routines work as *ambassadors* (HLA terminology). The RTI *ambassador* is used when a *federate* needs to talk with the RTI, and the *federate ambassador* is used when the RTI needs to talk with the *federate*.

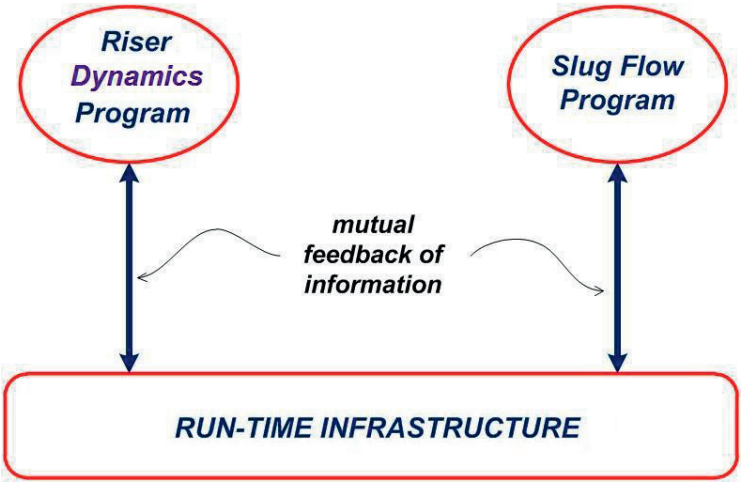

Figure 3. The constructed HLA *federation*

4. The Slug Flow

This chapter briefly describes the physical model of the transient slug flow program. A complete description of this program can be found in the work of Kjølaas [18]. The two-phase flow program is capable of simulating real life scenarios related to slug flow in two-phase flow oil and gas pipeline systems.

Slug flow is a flow pattern commonly encountered in multiphase oil and gas pipelines in hilly terrain. The characteristic feature of slug flow is the intermittent presence of liquid slugs and large gas bubbles. The length scales of slugs and bubbles can vary from a few pipe diameters to pipeline system lengths. Slugs may consist entirely of liquid or may contain entrained gas in the form of dispersed bubbles.

Slug flow makes up of slugs and bubbles with random lengths and velocities are called *hydrodynamic slugging*. That type of slug flow is generated mainly due to hydrodynamic instabilities at interface liquid and gas. *Severe slugging* is another type of slug flow. It is generated by liquid accumulation at the deepest point of riser. The *severe slugging* is characterized to have a cyclical behavior: slug formation, slug production, blowout, and liquid fall back.

For the numerical implementation, the flow domain is divided into slug regions and stratified flow regions using an adaptive grid. The scheme is a hybrid model based on combining a transient 1D two-fluid model (TFM) with a slug tracking model. The approach is based on an adaptive grid so that slug flow may be simulated without excessive grid refinement. A finite volume method (FVM) with a staggered grid is used, defining phase velocities at the cell faces, while other parameters are defined midway between the cell faces. The equations are linearized with respect to the unknown variables to obtain implicit time integration. The solution can thus be found efficiently using direct Gauss-elimination.

The 1D domain is defined by a list of consecutive pipes, each pipe having a specific length, inclination angle, diameter, and wall roughness. The numerical grid is defined by a list of sections of varying types (bubbles and slugs) and lengths along the riser. Bubble sections are sections that contain both gas and liquid, while slug sections contain only liquid (Figure 4).

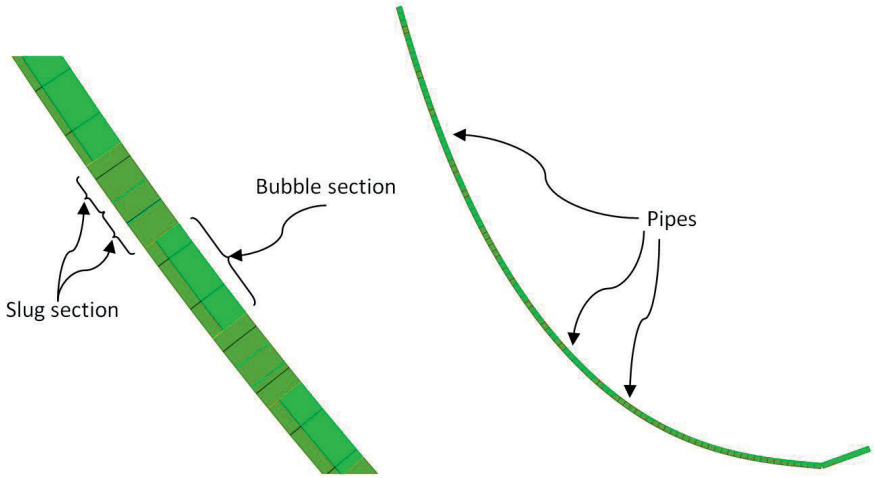

Figure 4. Riser geometry showing pipes, slug and bubble sections.

The physical model is based on the 1D two-fluid conservation equations. A finite volume method is used, and the equations are integrated in space and converted to the discretized form. The equations are solved in two steps. First, the momentum and pressure equations are solved simultaneously, allowing the phase velocities and pressures to be computed. Finally, the mass equations are solved, and then the phase masses are updated.

In the discretized equations, spatial indices are denoted by *j* in lower and upper case. For two-phase regions, a staggered grid is employed, defining velocities at cell faces (bubble section faces) using the subscript *j*. Scalar properties, such as pressure, density and phase fraction, are stored at bubble section centres defined using the subscript *J*. For slug regions, an integral procedure is used, so the subscript *j* defines the centres of slug sections, and the subscript *J* denotes the moving boundaries of slugs, see (Figure 5). Stratified regions are shown on the left, and slug regions are shown on the right. Solid lines indicate section borders, and dashed lines indicate section centres.

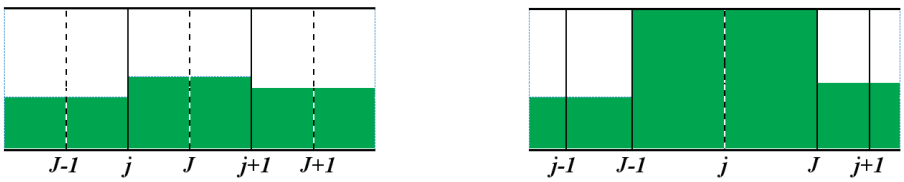

Figure 5. Regions and index notation in the dynamic grid

In 1D fluid flow modelling, closure relations are needed to account for the friction in the system. In the case of two-phase flow, there are three types of friction: gas-wall friction, liquid-wall friction and the interfacial friction between the gas and the liquid. In the flow code, frictional shear stress is expressed using the Darcy friction factor definition:

$$\tau = \frac{1}{8}\lambda\rho|u|u \tag{13}$$

Here, τ is the shear stress, λ is the friction factor, ρ is the phase density, and u is the phase velocity. The Haaland friction factor is applied for the shear stress between the fluids and the wall:

$$\frac{1}{\sqrt{\lambda_{kw}}} = -1.8\log\left[\frac{6.9}{\mathrm{Re}_k} + \left(\frac{\varepsilon}{3.7D_{h,k}}\right)^{1.11}\right] \quad ; \quad \mathrm{Re}_k = \frac{\rho_k D_{h,k} u_k}{\mu_k} \tag{14}$$

Here, Re_k is the Reynolds number for phase k, ε is the wall surface roughness, and $D_{h,k}$ is the hydraulic diameter.

For the gas and liquid phases, the hydraulic diameters $D_{h,k}$ are defined, respectively, as follows:

$$D_{h,g} = \frac{\pi D^2}{S_g + S_i} \quad ; \quad D_{h,l} = \frac{\pi D^2}{S_l} \tag{15}$$

where D is the pipe diameter, S_g and S_l are the gas and liquid wetted perimeters, respectively, and S_i is the width of the liquid interface.

The interfacial shear stress τ_i is modeled in much the same way as the wall shear stress:

$$\tau_i = \frac{1}{8} IFM\, \lambda_{gw}\rho_g \left|u_g - u_l\right|\left(u_g - u_l\right) \tag{16}$$

Here, IFM is the interfacial friction multiplier and is user defined. The default value for this parameter is 1, which is considered appropriate in the case of a smooth gas-liquid interface.

The fluid properties can be supplied as constant values, and an ideal equation of state for the gas phase is used to calculate the gas density. The pressure equation is resolved at cell centres and is obtained from the mass conservation equations and the equations of state for the two phases:

$$\sum_k \frac{V_k}{\rho_k}\left[\left(\frac{\partial \rho_k}{\partial p}\right)_{T_k}\frac{\partial p}{\partial t}+\left(\frac{\partial \rho_k}{\partial T_k}\right)_{p}\frac{\partial T_k}{\partial t}\right]+\frac{\partial V}{\partial t}+\sum_k \frac{1}{\rho_k}\oint_{A_k}\rho_k(u_k-u_b)\,dS=\sum_k \frac{\dot{M}_k^s}{\rho_k} \tag{17}$$

The variation of temperature over time in this work is neglected, assuming an isothermal system.

The momentum equation is resolved at the cell faces in the stratified flow regions and between the slug borders for slug regions. The integrated momentum equation for phase *k* is shown here:

$$\begin{aligned}&\frac{\partial(M_k u_k)}{\partial t}+\oint_{A_k}\rho_k(u_k-u_b)u_k\,dS=\cdots\\ &-V_k\frac{\partial p}{\partial x}-M_k g\cos\varphi\frac{\partial h_{D,l}}{\partial x}+\oint_{A_k}\tau_k\,dS-M_k g\sin\varphi+\dot{M}_k^s u_k^s\end{aligned} \tag{18}$$

The pressure terms are eliminated using the discretized form of the pressure equation, Equation (17), yielding an equation containing only phase velocities as unknown variables.

The mass equation, Equation (19), is evaluated at the cell centers.

$$\frac{\partial M_k}{\partial t}+\oint_{A_k}\rho_k(u_k-u_b)\,dS=\dot{M}_k^s \tag{19}$$

After resolving all the equations, the phase fractions are computed by dividing the specific masses by the densities (found using the associated equation of state). The sum of the phase fractions in a cell generally does not equal unity:

$$\frac{m_{l,J}}{\rho_{l,J}}+\frac{m_{g,J}}{\rho_{g,J}}\neq 1 \tag{20}$$

This inequality reflects the fact that there is a discrepancy between the fluid densities (found using the state equation for the gas phase) and the fluid specific masses (found using the mass equations). The problem is resolved by adding the source term in the pressure equation, Equation (21), for the following time step:

$$\psi_{s,J}=\frac{AL_J}{\Delta t}\left(\frac{m_{l,J}}{\rho_{l,J}}+\frac{m_{g,J}}{\rho_{g,J}}-1\right) \tag{21}$$

This term ensures that mass is conserved over time, and that the sum of the phase fractions remains close to unity.

There are two main mechanisms that cause slug formation: liquid accumulation at low points and hydrodynamic instabilities. Both mechanisms can be captured in a regular 1D two-fluid model, provided that the grid is sufficiently refined.

For the slug regions, the velocity of the liquid is computed from an integral momentum balance for the mixture, Equation (18), called the mixture equation. For the gas velocity, a slip relationship is used: see Equation (22).

$$u_g = S_d \left(u_l + v_o \right) \tag{22}$$

In this work, the distribution slip ratio S_d is set to unity and the averaged drift velocity v_o to zero, which defines the no-slip condition. Another assumption in this work is that no gas entrainment occurs in a slug; thus, holdup equal to unity is assumed in the slug regions. As the slug travels along a pipe, it absorbs the liquid at its front and sheds the liquid at its tail. Thus, the front and tail velocities of a slug are not equal to the liquid velocity. The slug tail or bubble nose velocity is determined using the empirical propagation velocity u_{tail}, defined as follows:

$$u_{tail} = C_o u_l + U_o \tag{23}$$

where C_o captures the velocity profile effects, and U_o is the drift velocity in stagnant liquid. For the slug front velocity u_{front}, a mass balance across this front is valid:

$$u_{front} = \frac{H_{slug} u_{l,slug} - H_{bubble} u_{l,bubble}}{H_{slug} - H_{bubble}} \tag{24}$$

In this expression, the subscripts slug and bubble refer to the neighboring slug and bubble regions where this mass balance is defined.

5. Riser Dynamics

The global riser dynamics response was simulated using in-house code based on a full non-linear finite element method (FEM). Arbitrary riser configurations can be set in this program using a static non-linear FEM procedure. Then, dynamic time domain forces and moments can also be imposed on the riser model, and DEQ can be solved by stepwise numerical integration. The program models the riser by a series of two-dimensional beam column elements with six degrees of freedom. Effective tensions and bending moments are updated based on the non-linear geometrical stiffness. The effective weight is updated by the internal mass flow distribution. The program also considers drag forces from waves as well as inertia and added mass due to the surrounding sea.

The incremental formulation of the dynamic equilibrium equation for a discretized riser structure using a non-linear FEM can be expressed by Equation (3), Paz [11], repeated here for illustration.

$$M_{I_k} \Delta\ddot{r}_k + C_{I_k} \Delta\dot{r}_k + K_{I_k} \Delta r_k = F_{k+1}^{e\,*} - F_k^i \tag{25}$$

where k refers to the time step. The parameters $\Delta\ddot{r}, \Delta\dot{r}$ *and* Δr correspond to unknown increments in accelerations, velocities and displacements, respectively. M_I represents the global structural incremental mass matrix (average value within a time increment). This matrix comes from a local consistent mass matrix with different axial and lateral distributed mass (added mass). The local mass matrix is shown in Equation (26).

$$\begin{bmatrix} (\rho_0+\rho_a)l\frac{1}{3} & \cdots & \cdots & \cdots & \cdots & \cdots \\ 0 & (\rho_0+\rho_l)l\frac{156}{420} & \cdots & \cdots & \cdots & \cdots \\ 0 & -(\rho_0+\rho_l)l^2\frac{22}{420} & (\rho_0+\rho_l)l^3\frac{4}{420} & \cdots & \cdots & \cdots \\ (\rho_0+\rho_a)l\frac{1}{6} & 0 & 0 & (\rho_0+\rho_a)l\frac{1}{3} & \cdots & \cdots \\ 0 & (\rho_0+\rho_l)l\frac{54}{420} & -(\rho_0+\rho_l)l^2\frac{13}{420} & 0 & (\rho_0+\rho_l)l\frac{156}{420} & \cdots \\ 0 & (\rho_0+\rho_l)l^2\frac{13}{420} & -(\rho_0+\rho_l)l^3\frac{3}{420} & 0 & (\rho_0+\rho_l)l^2\frac{22}{420} & (\rho_0+\rho_l)l^3\frac{4}{420} \end{bmatrix} \quad (26)$$

Where ρ_0 is the dry element mass, ρ_a is the hydrodynamic mass in axial direction, ρ_l is the hydrodynamic mass in lateral direction, and l is the element length. This symmetric matrix is updated with the mass of the slug flow during the time domain simulation, see Equation (4).

Similarly, C_I stands for the global structural incremental damping matrix. A Rayleigh damping model is applied: see Equation (27).

$$C_{I_k} = \alpha_0 M_{I_k} + \alpha_1 K_{I_k} \quad (27)$$

In this expression, α_0 and α_1 represent the proportional damping coefficients. The global structural incremental stiffness matrix K_I is calculated based in a tangent stiffness, which can handle large displacements and rotations with small axial strains according to the corotational formulation, Crisfield [19], see Equation (28).

$$k_t = B^T C_l B + \frac{N}{l_c} zz^T + \frac{M_1 + M_2}{l_c^2}\left(rz^T + zr^T\right)$$

$$B = \begin{bmatrix} -\cos\beta & -\sin\beta & 0 & \cos\beta & \sin\beta & 0 \\ -\dfrac{\sin\beta}{l_c} & \dfrac{\cos\beta}{l_c} & 1 & \dfrac{\sin\beta}{l_c} & -\dfrac{\cos\beta}{l_c} & 0 \\ -\dfrac{\sin\beta}{l_c} & \dfrac{\cos\beta}{l_c} & 0 & \dfrac{\sin\beta}{l_c} & -\dfrac{\cos\beta}{l_c} & 1 \end{bmatrix} \tag{28}$$

$$C_l = \frac{EA}{l_o}\begin{bmatrix} 1 & 0 & 0 \\ 0 & 4\dfrac{I}{A} & 2\dfrac{I}{A} \\ 0 & 2\dfrac{I}{A} & 4\dfrac{I}{A} \end{bmatrix}$$

$$r^T = \begin{bmatrix} -\cos\beta & -\sin\beta & 0 & \cos\beta & \sin\beta & 0 \end{bmatrix}$$

$$z^T = \begin{bmatrix} \sin\beta & -\cos\beta & 0 & -\sin\beta & \cos\beta & 0 \end{bmatrix}$$

Here, k_t is the local variationally consistent tangent stiffness matrix. N is the axial force in the element. M_1 and M_2 are the local end moments of the element. l_c is the current element length. β is the current angle of the co-rotating frame with respect to the global coordinate system. E is the axial modulus of elasticity, A is the cross section area, and I is the moment of inertia.

Finally, in Equation (25), F^{e*} represents the time-varying external forces, see Equation (5). F^i stands for the internal forces, which is the sum of elastic, damping and inertia forces:

$$F^i = F^S + F^D + F^I \tag{29}$$

The global riser dynamics program performs iterations at each time step to ensure consistency between the forces and structural response at each finite element node. The Newmark method for stepwise integration is employed for the incremental solution procedure, Paz [11]. Into this algorithm the force balance iteration is implemented as follow:

1. Approximate displacement, velocity and acceleration response based in the last displacement increment (Δr_k).
2. Update increment mass (M_{Ik}), stiffness (K_{Ik}) and damping (C_{Ik}) matrixes.
3. Calculate internal elastic (F^S_{k+1}), damping (F^D_{k+1}) and inertia (F^I_{k+1}) forces.

4. Calculate the effective residual forces (ΔF_k).
5. Calculate the correction of the displacement increment (Δ).
6. Correct the last displacement increment (Δr_k^*).
7. Verify convergence. If convergence is not achieved go to step 1.
8. Calculate displacement, velocity and acceleration response for time $k+1$ based in balanced displacement increment (Δr_k^*).

To verify the reliability of the riser dynamics code used in the work, a series of numerical validations have been performed between results from the riser dynamics in-house code and recognized commercial software. The commercial software used for this validation is Flexcom.

The static configuration of a catenary riser has been calculated using non-linear finite element analysis (Figure 6). The riser of 770 m length is submerged into a sea with a main water level (MWL) of 300 m. To set this configuration, a horizontal force of 400 kN was applied at the top of the riser, and an effective weight of 0.58 kN/m was distributed along it. The external diameter of the riser is 400 mm with a thickness of 20 mm. For the axial and bending modulus of elasticity, a value of 206000 MPa was assumed. One hundred elements were used for the discretization. The boundary conditions at each end of the riser are fixed with respect to translation but free to rotate. Figure 7 shows the effective tension distribution, and Figure 8 shows the static bending moment. The results from the riser dynamics code exhibit excellent agreement with the result from the commercial software.

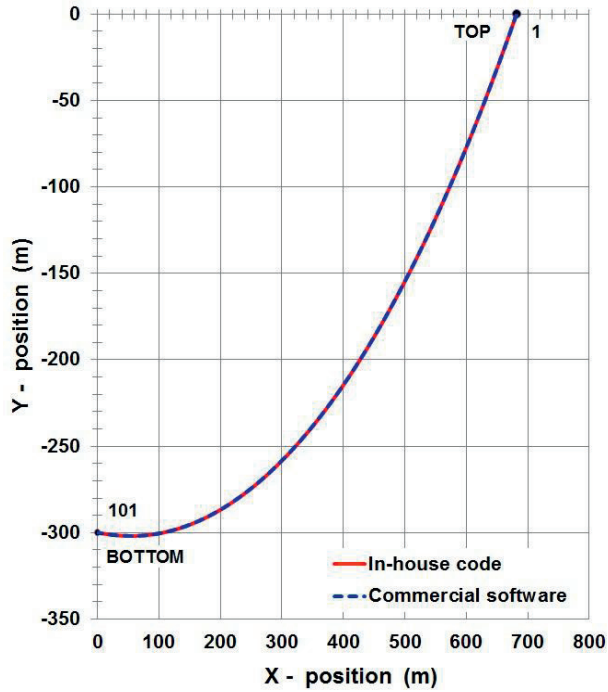

Figure 6. Static configuration.

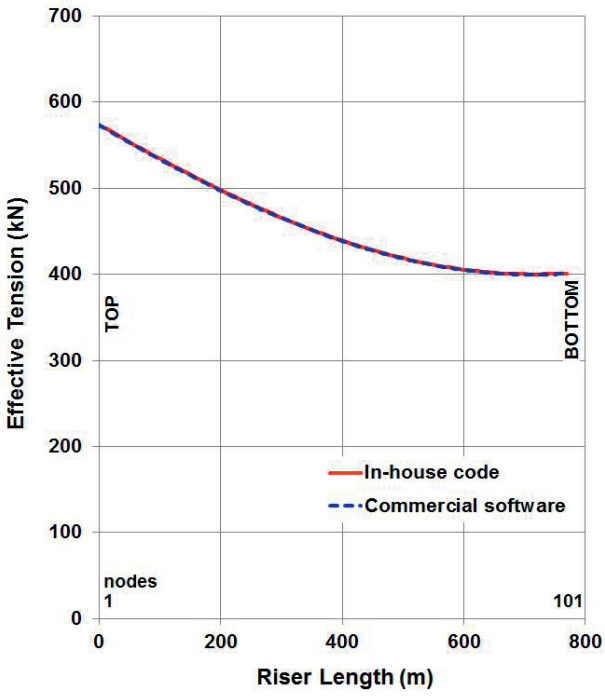

Figure 7. Static effective tension.

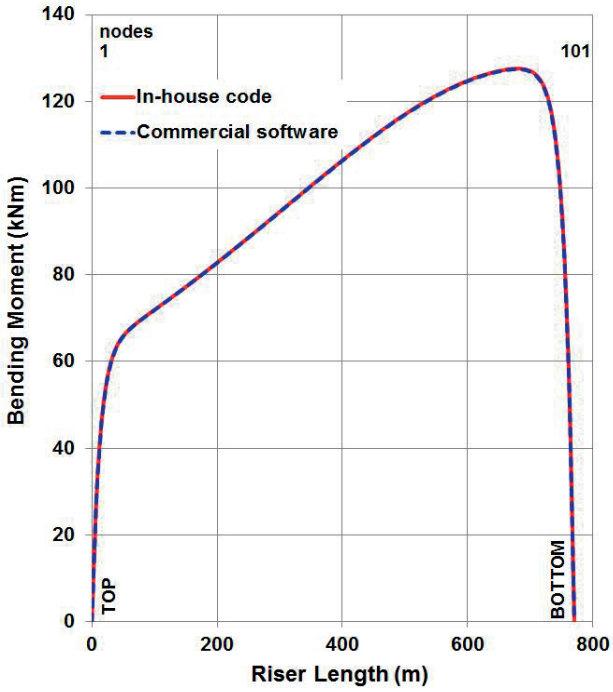

Figure 8. Static bending moment.

Continuing with the validation of the riser dynamics in-house code, a transient arbitrary load is applied at the middle of the riser. The load grows linearly from zero to a maximum value during 10 s, after which the load disappears (Figure 9). The direction of the load is vertical to MWL (Figure 10).

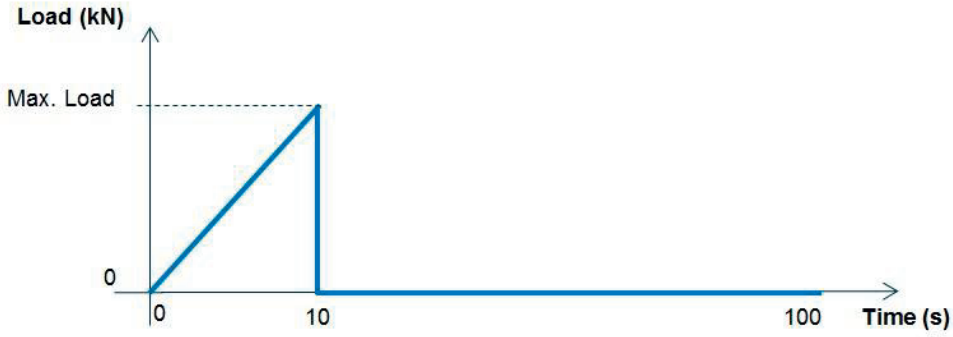

Figure 9. Arbitrary ramp load.

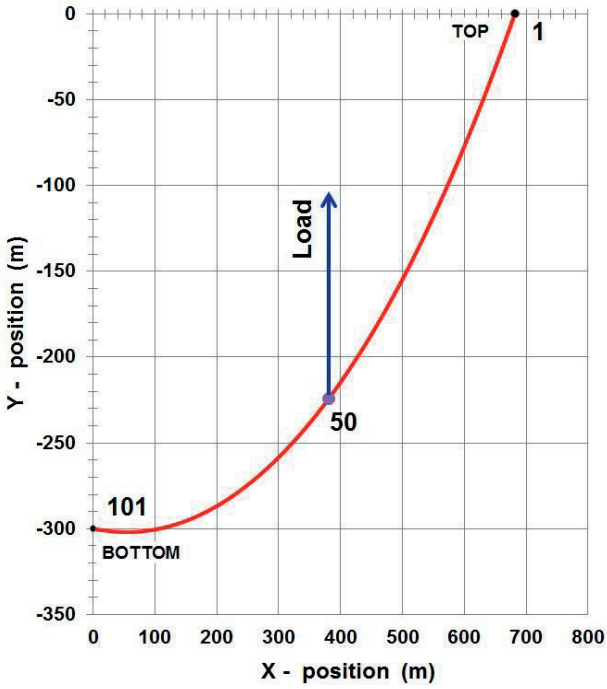

Figure 10. Node of application of ramp load.

The response considers the surrounding water with hydrodynamic coefficients of Cd = 1 (drag coefficient normal and tangential), Ca = 1 (added mass coefficient normal and tangential) and Cm = 2 (inertial mass coefficient).

The results show horizontal and vertical deformations of node 50 from its static configuration. One of the objectives of the validations is to demonstrate that the in-house code can capture the non-linearity of the response.

A first test is conducted by applying a maximum load of 1000 kN. Figure 11 and Figure 12 show the results of the horizontal and vertical deformations, respectively. The results come from the in-house code and from the commercial software using its non-linear model. Large displacements are presented. The agreement between the two programs is excellent.

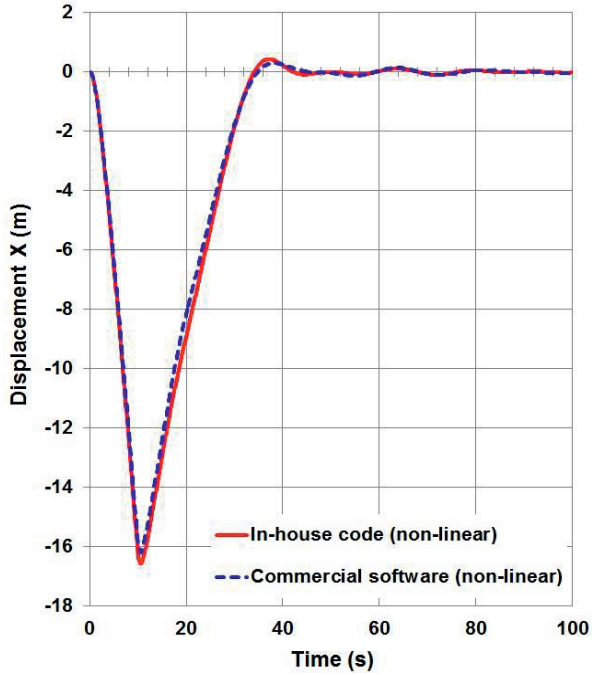

Figure 11. Horizontal deformation, non-linear models, 1000 kN.

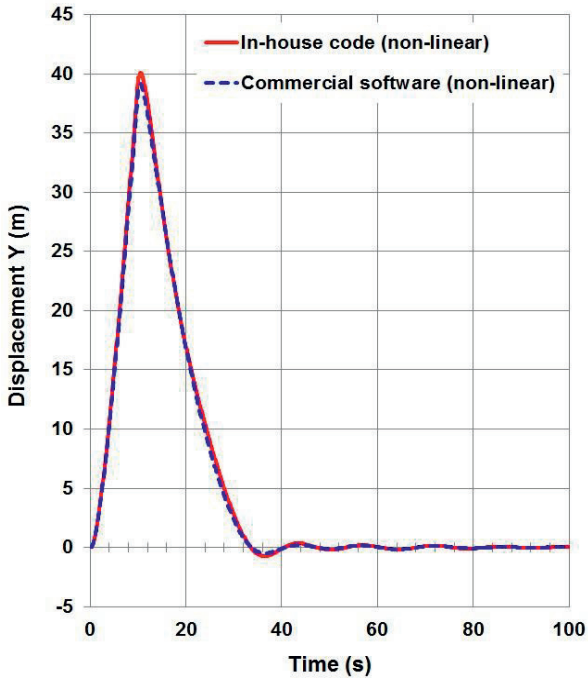

Figure 12. Vertical deformation, non-linear models, 1000 kN.

The same experiment was executed again, this time using the linear model of the commercial software. Figure 13 and Figure 14 show the results. It should be noted that the commercial software was not able to manage the large deformations due to the use of its linear model.

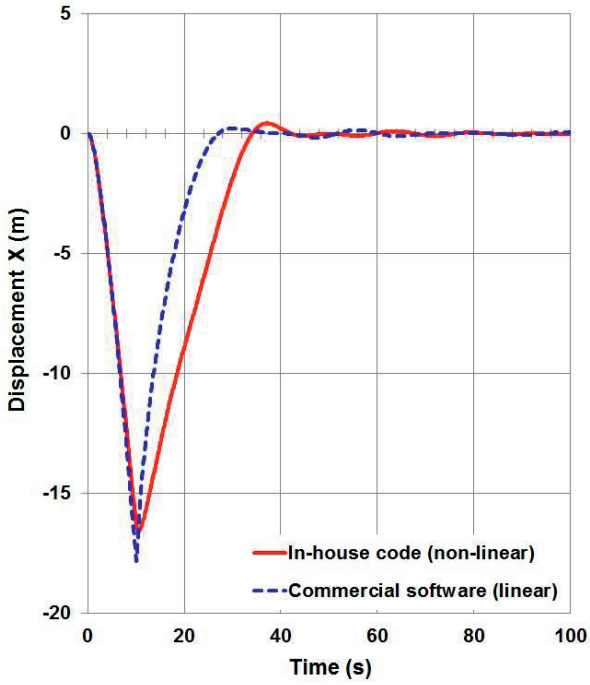

Figure 13. Horizontal deformation, non-linear vs. linear model, 1000 kN.

To generate small deformations, the same experiment was executed again, but with a maximum load of 100 kN. Figure 15 and Figure 16 show the results. Excellent agreement is observed between the two programs, each using its non-linear model.

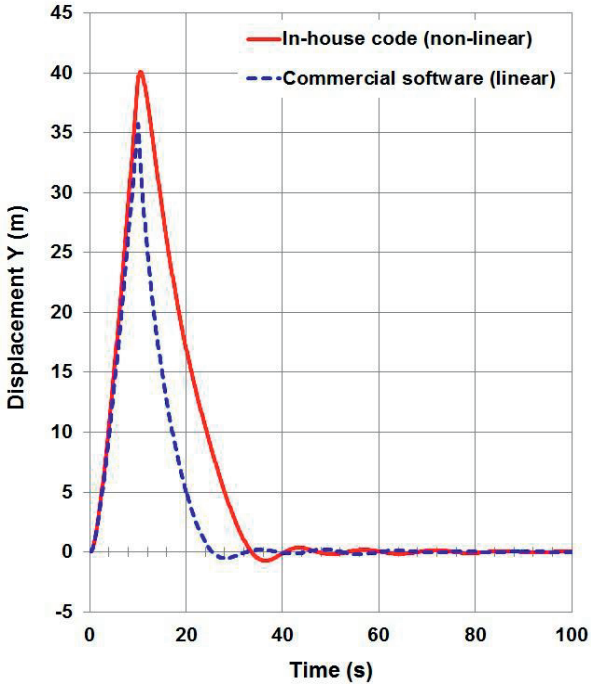

Figure 14. Vertical deformation, non-linear vs. linear model, 1000 kN.

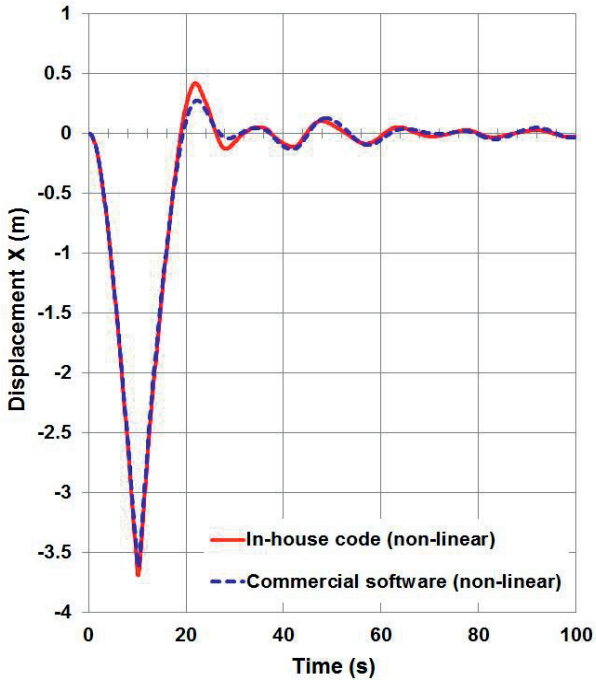

Figure 15. Horizontal deformation, non-linear models, 100 kN.

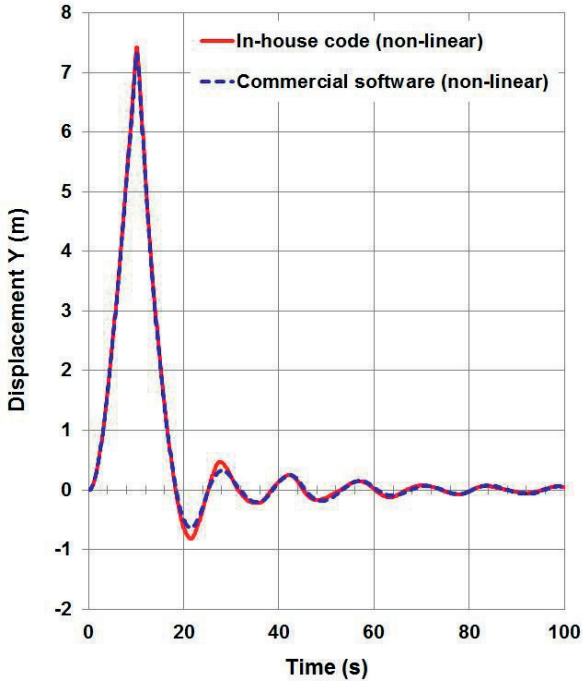

Figure 16. Vertical deformation, non-linear models, 100 kN.

In the final test conducted, the commercial software uses its linear model. Figure 17 and Figure 18 show the horizontal and vertical deformations. A good agreement between the two programs was found, as for small deformations the non-linear and linear models are closed.

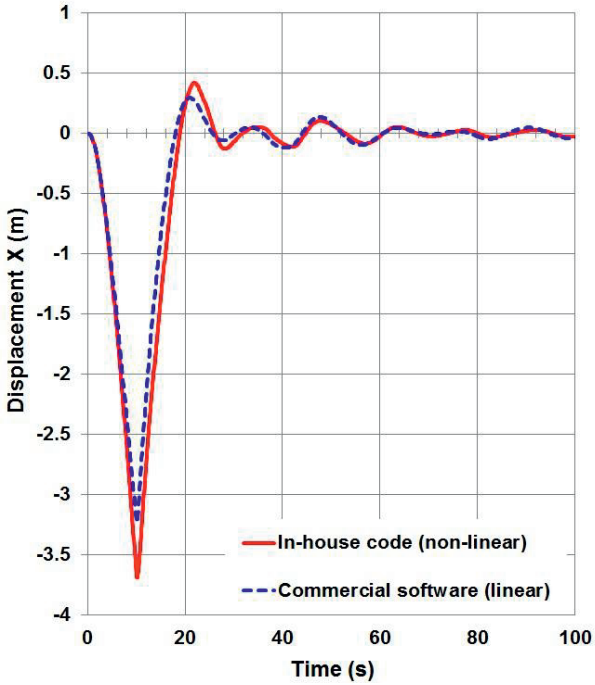

Figure 17. Horizontal deformation, non-linear vs. linear model, 100 kN.

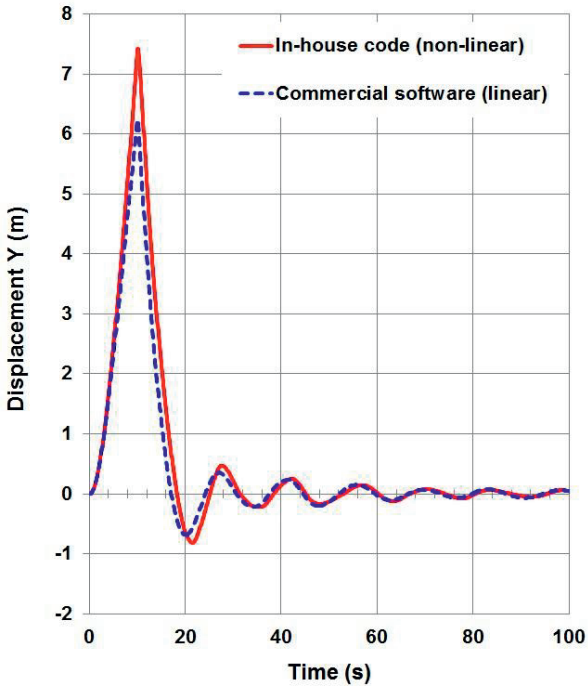

Figure 18. Vertical deformation, non-linear vs. linear model, 100 kN.

6. HLA Communication

Throughout the development of this work, the principles of re-use, interoperability, and distributed simulation have been followed. Re-use [20] stands for the re-use of existing software. The riser dynamics code is a program written in Fortran using non-fashioned modular programming. In this work, the riser dynamics program is working together with a fashioned object oriented program written in C++. This last program is the slug flow code. Interoperability [21] means that different systems created for distinct purposes are able to work together properly into a combined and consistent manner to achieve common objective. Thus, the riser dynamics program has been implemented to simulate the dynamic of flexible risers, and the slug flow code has been developed to simulate transient slug flow. One of the objectives of this work is to study the influence of slug pattern on the response of slender structures. Finally, distributed simulation [22] refers to the synchronized execution of different simulators installed in separate computers, even with distinct technology and even located in different geographic areas, using a network connection. The riser dynamics code and the slug flow code work as stand-alone simulators, and in many tests, they are operated using their own hardware resources (different computers linked by the internet).

The communication interface built to couple the riser dynamics code and the slug flow program was developed following the High Level Architecture (HLA) methodology, which is explained on the standard IEEE 1516 for distributed simulation systems [13], [14] and [15]. The main reason for using HLA for communication between the slug flow and the riser dynamics programs is that they are based on different programming language and data structure. They are also developed in different research groups, and might be modified independently. By keeping them separate, further developments may take place independently as long as the communication between the programs remains unchanged. It will also make it possible to apply other programs for riser dynamics or slug flow by introducing the communication part only.

High Level Architecture promotes the re-use and interoperability of distributed simulations. According to HLA terminology, the programs or simulation units are called

federates. They are combined to create one large simulation system, called a *federation*. The simulators (*federates*) are considered to be HLA compliant, which means they follow the HLA rules, interface specification and object model template.

The HLA rules [13] define how a *federate* and its family (*federation*) operate. These rules bind *federates* to HLA as the only methodology to exchange information. Meanwhile, the HLA interface specification [14] links a simulator to other simulators in the *federation*. It is a *document* that describes services that *federates* need to call to send or receive information. The interface specification makes each simulation be interoperable. Its instantiated program is called Run-Time Infrastructure (RTI). As each *federate* can be developed using different technologies and conventions, all necessary information that each *federate* needs to *publish* and/or *subscribe* are described in the object model template format (OMT) [15] using a universal language that each *federate* in the *federation* can understand.

The HLA provides two main prebuilt classes (object-oriented programming terminology, OOP) that contain the necessary services [14] to establish communication between *federates* and the RTI. Thus, when a *federate* needs to communicate with the RTI (*Call*), it invokes methods contained in a class named RTI Ambassador. Similarly, when the RTI needs to talk with a *federate* (*Callback*), it invokes methods contained in the Federate Ambassador class (Figure 19).

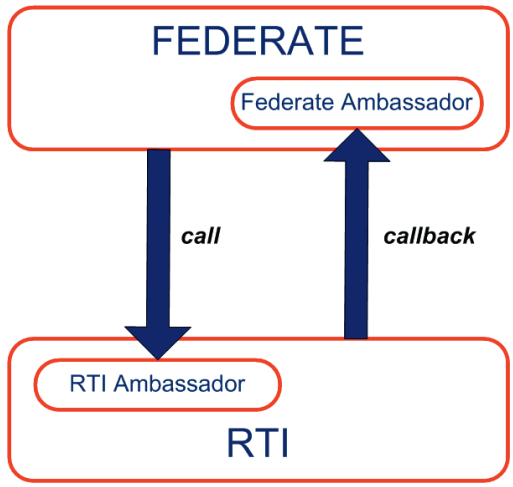

Figure 19. HLA – *Call* and *callback*.

The prebuilt classes are computational code written in C++ OOP. The class Federate Ambassador has been adapted and compiled together with each *federate* (the riser dynamics program and the slug flow program). As the riser dynamics program was written in Fortran, the class Federate Ambassador has been linked to it by creating a dynamic link library file (DLL).

Regarding the information that each *federate* needs to send and receive, the slug flow code is *subscribed* to the riser geometrical configuration represented by the angle of inclination of each element or pipe. (The slug flow code sees the riser as a series of pipes, and the slug flow sees a constant length of the riser along the simulation, which means, some axial deformation along the riser is neglected for the slug flow development). Furthermore, the slug flow program *publishes* the velocities of each phase, the internal fluid pressure and the liquid holdup. Similarly, the riser dynamics code is *subscribed* to the gas and liquid velocities, the internal pressure and the holdup. Consequently, this program *publishes* the geometrical position of each node.

Generally transient flow programs work using a variable time step following the CFL criterion [23] to avoid losing information when the wave velocity travels from the face of one control volume to the other. However, riser dynamics programs work using a constant time step to avoid instability. Thus, the communication interface is leading two programs with different progress in computational time; the slug flow program and the riser dynamic code. To manage the issue of the time step, the following procedure was considered. Considering that the time step for the riser dynamics program is higher than the variable time steps for the dynamic flow code (i.e. the riser program works with time steps of order 10^{-1} or less, and the dynamic flow program works with a time step of order 10^{-3} or less), a master time step is considered. The master time step is defined by the riser dynamics code. Thus, the computational time of the dynamic flow code starts to increase, and when this time matches the master time step, an exchange of information occurs. The computational time of the riser dynamics code is incremented by the master time step. The same process start again, the computational time of the dynamic flow code is newly incremented by a new calculated time step, and the process continues until the two computational times are matched again.

There is an issue regarding this method of managing the time step. The two computational times will never match. Thus, the last accumulated time step of the dynamic flow code is reduced arbitrarily to allow the two computational times to be

matched. Theoretically, a shorter time step fit the dynamic flow well; however, time steps that are too short can introduce instability problems.

The sequence for exchanging information through the federation is as follows:

1. The two computational times, one from each program, match (time k).
2. The slug flow program sends information to the riser dynamics code.
3. The riser dynamics code resolves its mathematical model using the received information for time k.
4. The riser dynamics code sends information to the slug flow program.
5. The slug flow program uses the received information to resolve its mathematical model for time k+1. This time k+1 belongs to the computational time of the slug flow program.

Numerical analysts could call this procedure as an explicit approach to resolve the whole set of mathematical models. An improved version of the federation could apply an implicit method, which means iterations when the two computational times match. An implicit method could increase the processing time considerably with negligible influence on the results.

7. Case Study

7.1 Effective tension variation

7.1.1 Objective

The objective of this test case is to conduct a numerical experiment to study an unsteady slug flow progressing through a flexible riser and to analyze the influence of this two-phase flow pattern on the change in the riser effective tension and the bending moment. The interaction between the slug flow and the dynamic response of a flexible riser is modeled by solving the fluid conservation equations (mass and momentum) for the internal two-phase flow and the dynamic equilibrium equation for the structure response. Additionally, the Morison equation is used to calculate the external hydrodynamic loads on the riser.

7.1.2 Case definition

To analyze the effective tension variation of a flexible riser due to an internal slug flow, a free-hanging catenary configuration was selected. This case represents a flexible riser 450 m in length submerged into the sea with a water depth of 300 m; 16.5 m of the riser is above the water surface. To establish this configuration, a horizontal force of 80.22 kN was applied to the top, and an effective weight of 0.59 kN/m was distributed along the riser. This riser has an equivalent homogeneous cross-section of 400.0 mm external diameter and 360.0 mm internal diameter. Figure 20 represents the static configuration of the riser. For the axial modulus of elasticity, a value of 206000 MPa was considered, with 10% for the bending modulus. These values are intended to model a flexible riser case where the two moduli are different. One hundred elements of equal length were used for the finite element model discretization. The boundary condition at the touchdown point is considered fixed but free to rotate, which also applies at the top of the riser.

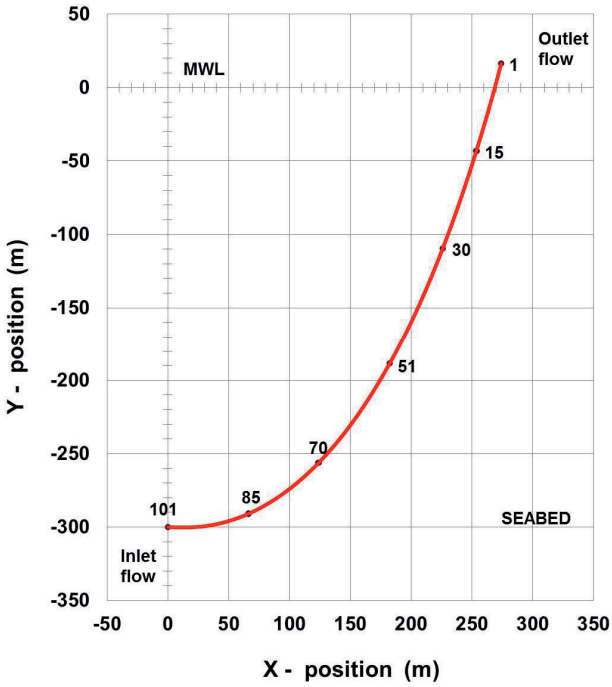

Figure 20. Catenary static riser configuration.

Mass flow rates of 8 kg/s for gas and 300 kg/s for liquid were used for the internal two-phase flow under isothermal conditions. Air and water were employed as the working substances. The gas density behavior follows the ideal gas law, and for the water, a density of 998.78 kg/m^3 was considered at a temperature of 290.15 K and 1 atmosphere pressure. At the outlet, a pressure of 101.325 kPa was determined.

Drag and added mass in the still water were determined using the Morison equation. Both the added mass and drag coefficients were 1.0 for the present calculations. Sea water density equal to 1025 kg/m^3 was assumed.

The simulation started with the riser completely filled with gas and pressurized at 1 atmosphere. The riser profile, boundary and initial conditions were selected to provide conditions for the generation of a series of random *hydrodynamic slugging* [24].

The distributed simulation was run for 1000 computational seconds, following a parallel and synchronized HLA procedure. For the global riser analysis program, a fixed time step of 0.1 s was used to maintain stability, and the two-phase flow code was implemented to work using a variable time step computed according to the *CFL* criterion.

7.1.3 Results from simulation

A non-linear static analysis was conducted before beginning the time integration procedure. Figure 21 shows the distribution of the effective and true tension along the riser as calculated by this analysis. As the initial flow condition was a stagnant non-compressed fluid, the difference between the true and effective tension is due to the external and internal static pressure, as described by Equation (6).

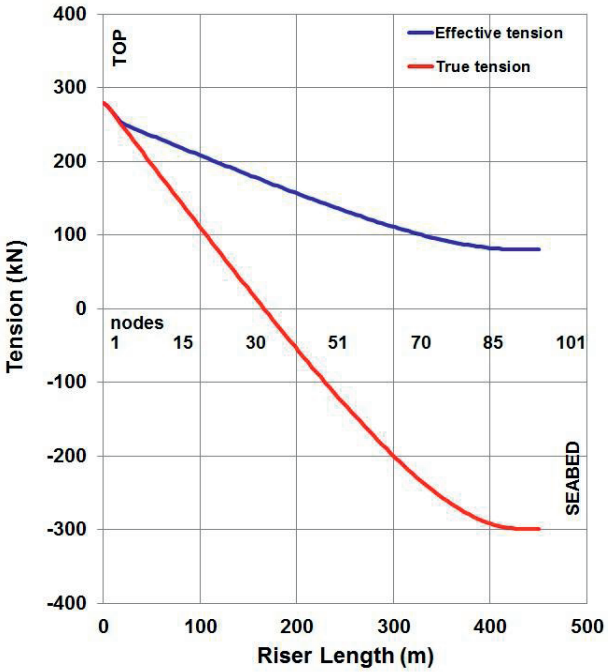

Figure 21. Effective and true tension distribution after static analysis.

Continuing with the static analysis, Figure 22 presents the bending moment distribution before the dynamic analysis starts. Because boundary conditions include free rotations at the riser ends, an abrupt increase in the bending moment is located at both ends, with the largest peak close to the seabed (maximum curvature).

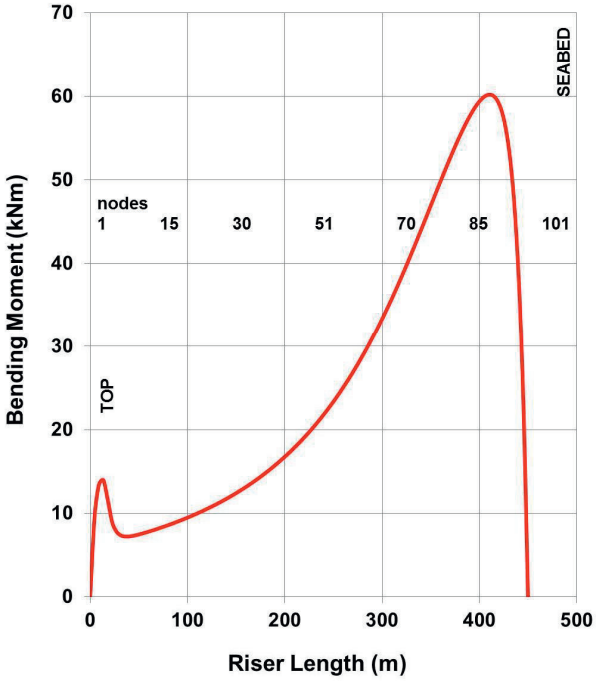

Figure 22. Bending moment distribution after static analysis.

The results from the dynamic analysis are presented in two parts. The initial part covers the startup phase of the process, and the second part covers the remaining simulation period. This approach to presenting the results was used because the startup sequence contains the largest displacements and bending moment variations. During this period, the effective tension and the two-phase flow pressure increase to reach a new dynamic equilibrium level. During the second part of the simulation, smaller deformations and tension variations were observed.

Figure 23 shows snapshots of the riser profile recorded during the startup period. A characteristic point of change in direction of the displacements (above and below the static riser profile) can be observed close to node 70. The greatest generation of random slugs occurs near node 85 due to the hydrodynamic and geometric conditions.

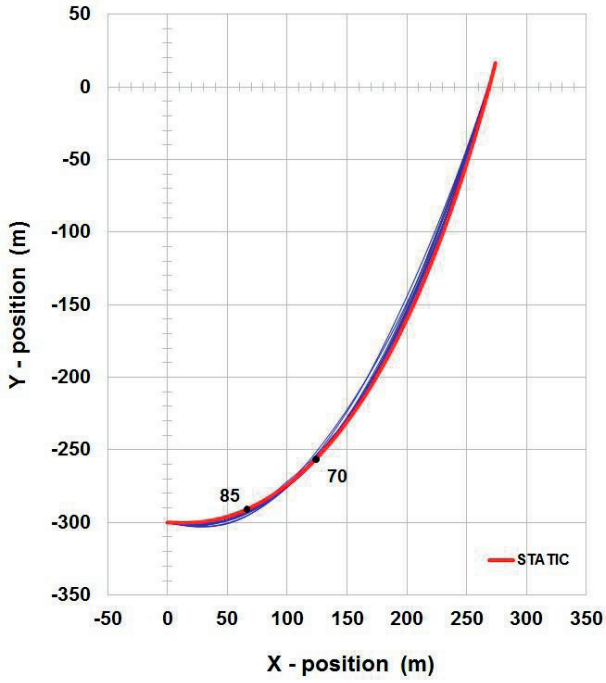

Figure 23. Snapshots of riser shapes during startup.

The behavior of the inlet internal pressure during the startup of the simulation is shown in Figure 24. A rapid increase in pressure as the slug flow approaches the riser is observed. At the end of the startup period, the inlet pressure increases to almost 24 times its initial value. This value is reached seconds after the first slugs cross the riser outlet. The dynamic steady state pressure (Figure 25) is the inlet pressure level necessary to maintain a continuous two-phase flow rate along the riser for the selected geometric configuration and boundary conditions. Figure 25 also shows the inlet pressure variations for the remaining part of the simulation. The pressure variations are caused by the transient change in the two-phase flow momentum formed by the liquid slugs and gas bubbles, the shapes and velocities of which change as they travel along the riser.

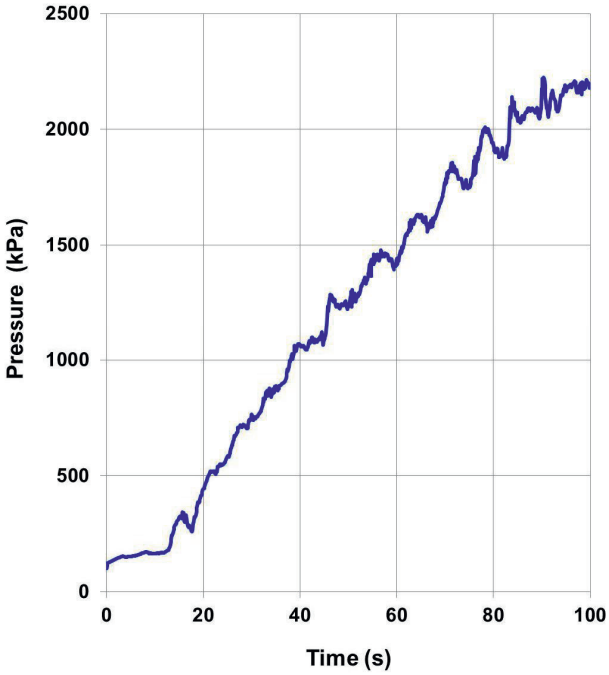

Figure 24. Time history of the internal flow inlet pressure recorded during startup.

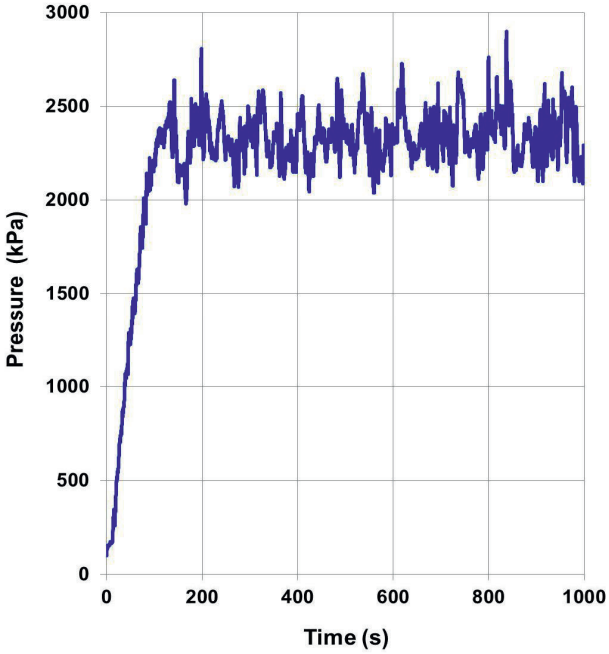

Figure 25. Time history of the internal flow inlet pressure recorded during the time integration.

Figure 26 and Figure 27 present, respectively, the liquid and gas flow rates at the riser outlet as a function of time during the last part of the startup period. These flow rates are represented by their equivalent liquid and gas superficial velocities.

These figures also show the holdup behavior at the outlet of the riser during the same period of time. A slug is crossing the riser outlet when the holdup reaches one, indicating that only liquid flow is produced. These figures clearly show that slugs of different sizes are crossing the riser outlet and that the first slug reaches the riser outlet approximately 77 s from the beginning of the simulation.

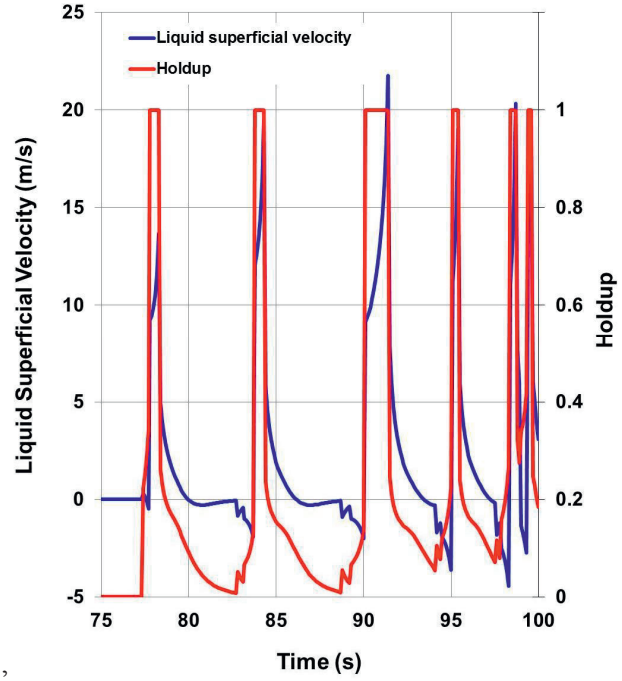

,

Figure 26. Time history of the outlet liquid flow rate recorded at the end of the startup.

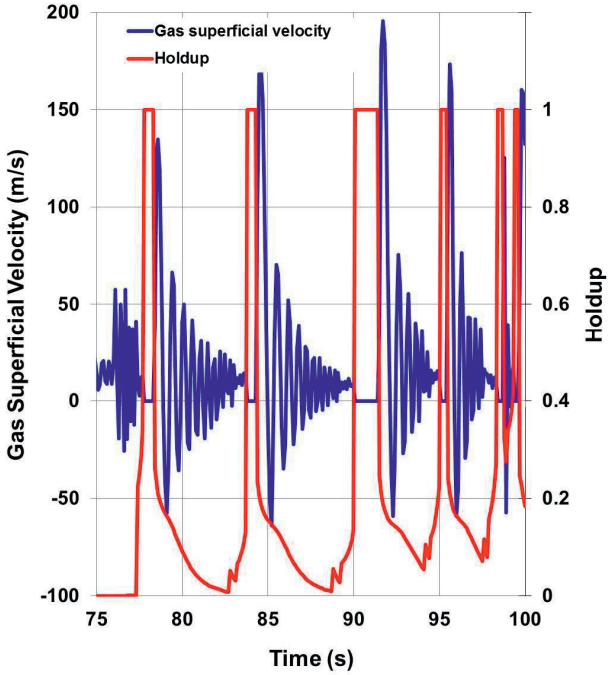

Figure 27. Time history of the outlet gas flow rate recorded at the end of the startup.

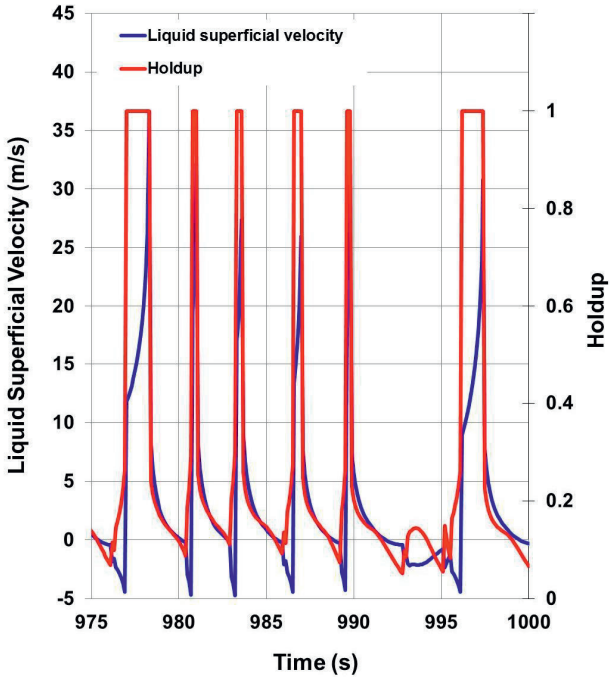

Figure 28. Time history of the outlet liquid flow rate recorded at the end of the time integration.

Unstable behavior of the gas superficial velocity after a slug crosses the riser outlet can be observed in Figure 27 due to the effect of the compressible flow on its density. In contrast, the liquid superficial velocity (incompressible flow) presents a more stable development (Figure 26). Similar behavior was predicted for the remaining simulation period, see Figure 28 and Figure 29.

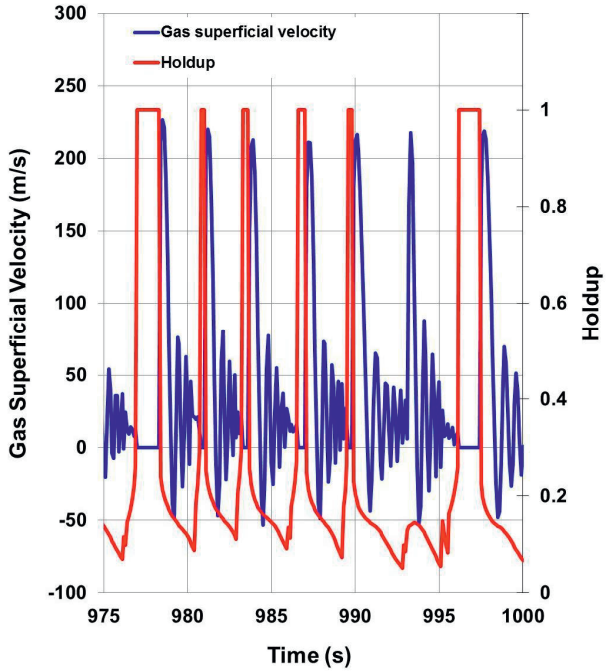

Figure 29. Time history of the outlet gas flow rate recorded at the end of the time integration.

For this work, Equation (6) is reordered to Equation (30) to enable a better understanding of the influence of slug flow on the true tension.

$$\begin{aligned} T_w &= T_e - \Delta PA + \sum \dot{m}_k u_k \quad ; \quad where \\ \Delta PA &= P_e A_e - P_i A_i \quad ; \quad and \\ \sum \dot{m}_k u_k &= \dot{m}_l u_l + \dot{m}_g u_g \end{aligned} \tag{30}$$

Therefore, in addition to the effective tension, there are contributions from the external and internal pressures multiplied by their respective cross-sections (*pressure*

tension ΔPA) and from the slug flow momentum (*momentum tension* $\sum \dot{m}_k u_k$). Clearly, the internal pressure and slug flow momentum work in favor of the true tension.

The time history of the effective tension at the top of the riser is shown in Figure 30 for the startup period. A rapid increase in the effective tension can be noted. This behavior is generated by the incoming slug flow. At the end of the startup, almost a double value of the effective tension was reached. The effective tension increment is accompanied by three other tensions. The first tension is the true tension, which almost follows the effective tension curve. The second tension is the tension generated by external and internal pressure variation. At the upper end of the riser, only internal pressure is involved, as this node is located above the MWL. The last tension is derived from the contribution of the flow momentum of the liquid and gas phases. The momentum tension works against the effective tension [see Equation (30)]. Based on Figure 30, a sequence of small fluctuations of the pressure and the momentum tensions at the end of the startup (approximate time 77 s) are observed when the first slugs are leaving the riser outlet. This condition leads to the differences between the effective and the true tension.

A better view of the most interesting part of the last figure is shown in Figure 31. This figure represents the last 25 seconds of the startup. The outlet holdup for the same period of time is also found in the figure. Clearly, the tension caused by the internal pressure and the momentum follows the slug development.

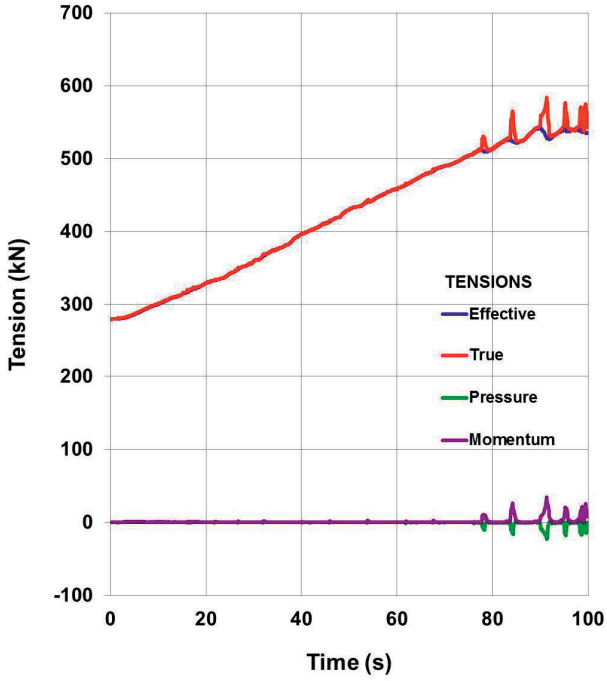

Figure 30. Time history of the top tensions recorded during startup.

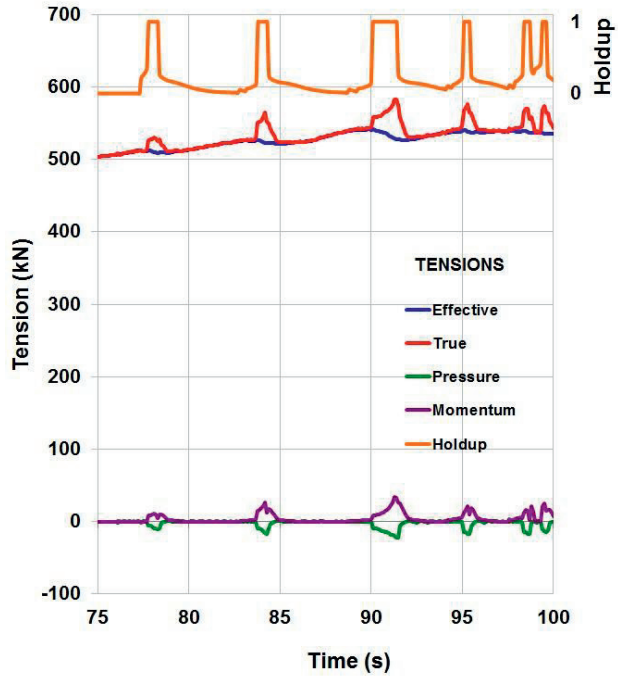

Figure 31. Time history of the top tensions recorded at the end of startup.

After the start-up period, the system will enter a state of *dynamic stabilization*. A sequence of slugs and bubbles travels along the riser with variable velocities and lengths. These slugs can rise, grow or vanish according to the two-phase flow mass and momentum balances. The variation of the top tension is shown in Figure 32. The rapid variation in the effective weight and centripetal forces by the slug flow produces changes in the effective tension. In this simulation, larger values of the true tensions were predicted in comparison to the effective tension, mostly due to the fluctuating two-phase flow momentum and the change in internal pressure.

A magnification of the last 25 seconds of the previous figure is shown in Figure 33. The holdup development at the outlet is also shown in this figure. Again, the influence of the traveling slugs on the increase in true tension is clearly visible.

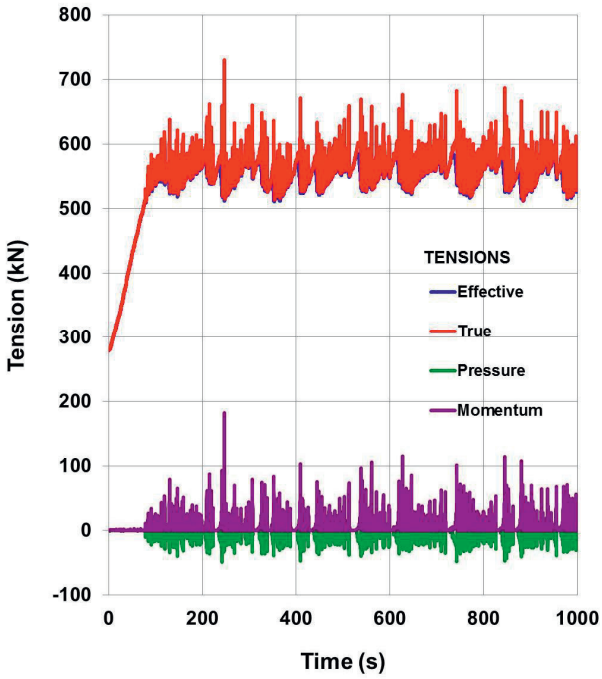

Figure 32. Time history of the top tensions recorded during time integration.

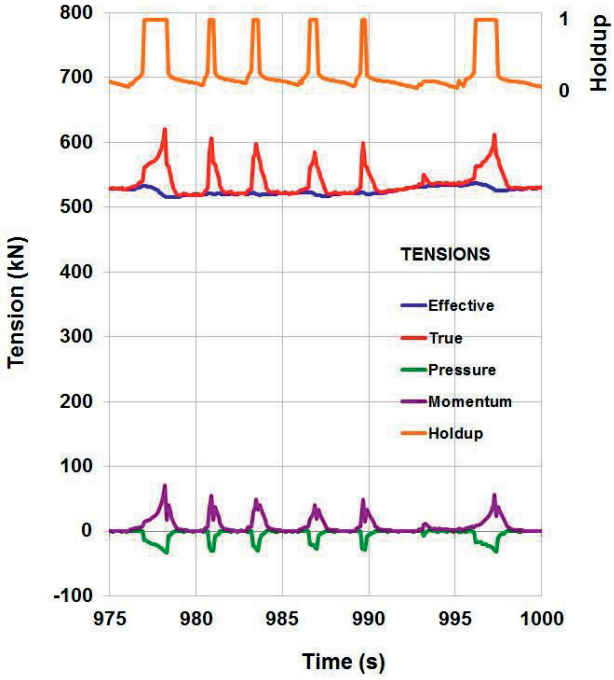

Figure 33. Time history of the top tensions recorded at the end of the time integration.

Figure 34 presents the tension variation at node 70 (the node closest to the characteristic point). The tension due to the external and internal pressure decreases because the internal pressure is increasing, and its tension works against the tension generated by the external pressure [see Equation (30)]. The value of the external pressure almost becomes constant due to the water column. Low values of the flow momentum tension are calculated because node 70 is close to the place where the slugs are originated (the liquid accumulation zone), a region where low values of liquid velocities are predicted. The growth of the internal pressure increases the true tension.

Figure 35 shows the tension components for the period when the entire riser is filled with a dynamic fluid/gas mixture (slug flow). After the dynamic stabilization, the main contribution to the variation in the true tension comes from the variation of the internal pressure. The true tension is lower than the effective tension due to the pressure generated by the external water column [see Equation (30)].

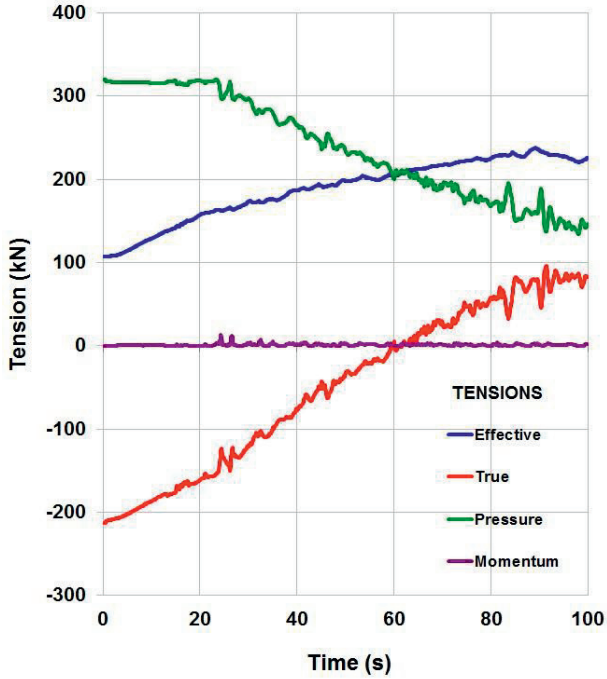

Figure 34. Time history of tensions at node 70 recorded during startup.

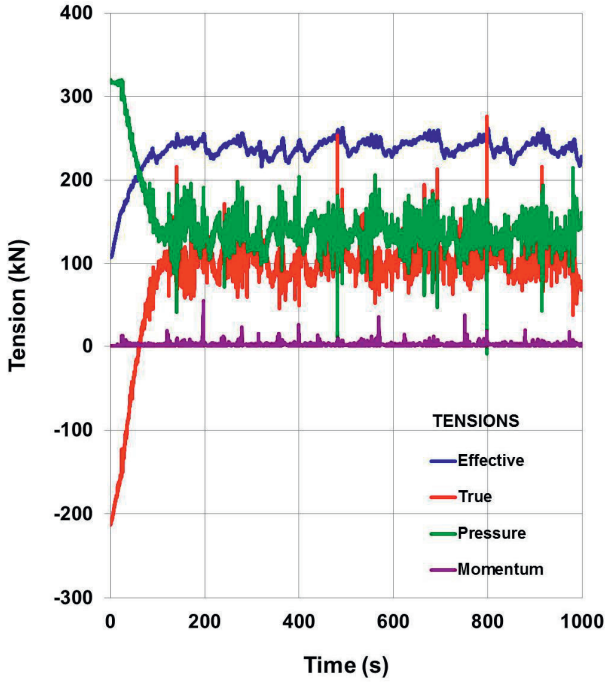

Figure 35. Time history of the tension components at node 70 recorded during the time integration.

As with the effective tension, another important influence from the slug flow is the change in the effective weight. The simulation shows a high variation of the effective weight as the slug flow was developing along the riser in an irregular manner. The slug flow is characterized by a constant variation in the liquid and gas mass flow rate distribution in the pipe.

Figure 36 shows the time history of the bending moments predicted during the startup for the selected nodes (see Figure 20). The bending moment begins to change as the slug flow travels through the riser from the inlet (node 101) to the outlet (node 1). The variations follow the static bending moment profile (Figure 22), where the maximum values are located near node 85 and the minimum near node 15. Correspondingly, Figure 37 shows the bending moment variation for the rest of the simulation (after 500 s) for the node that presented the highest fluctuations and the node in the middle of the riser. The largest variations are caused by the traveling slugs. These bending moment fluctuations are needed data for fatigue analysis that might be carried out by post-processing of the results.

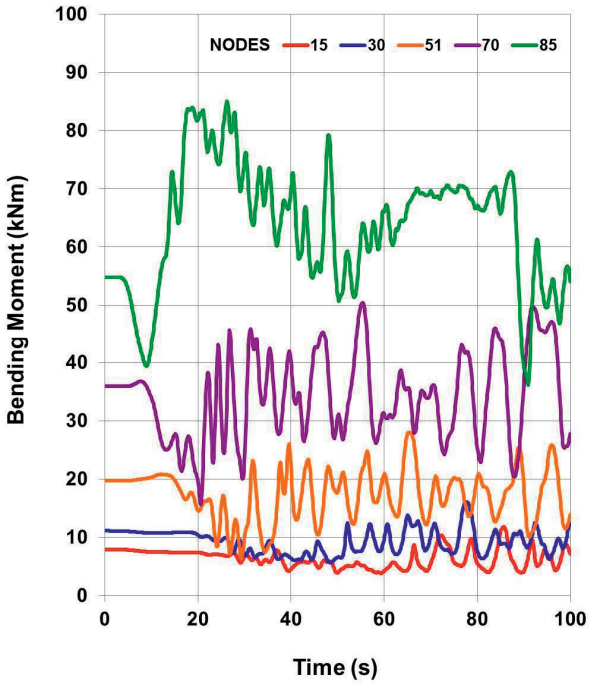

Figure 36. Time history of the bending moment recorded during startup.

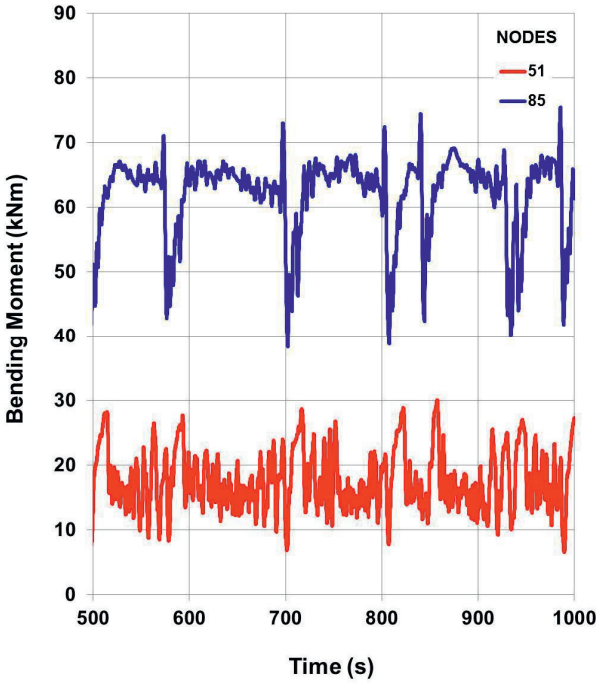

Figure 37. Time history of the bending moment recorded during time integration.

Figure 38 and Figure 39 show the deformation time histories for the selected nodes in the *x* and *y* directions, respectively, during the startup of the simulation. The interaction between the slug flow and the flexible riser structure generates irregular deformations along the time line of the simulation. This behavior is typical for risers with slug flow because this phenomenon itself exhibits an irregular and unstable behavior. As noted above, when the slug flow starts, the riser structure begins to move to the left in Figure 38 and will later begin to return to its original position. Similarly, in Figure 39, the approaching slug flow produces upward displacements, except for node 85, which is displaced downward.

The change in the direction of the deformation occurs between the region of the characteristic point (node 70) and the liquid accumulation zone (node 85). This region is characterized by the high-hitting jet streams of the two-phase flow followed by the accumulation of liquid and the succeeding generation of random slugs. The initial deformations of the riser attempt to regain their static configuration later. Thus, we suspect that the centripetal forces have a greater influence than the gravity forces during startup.

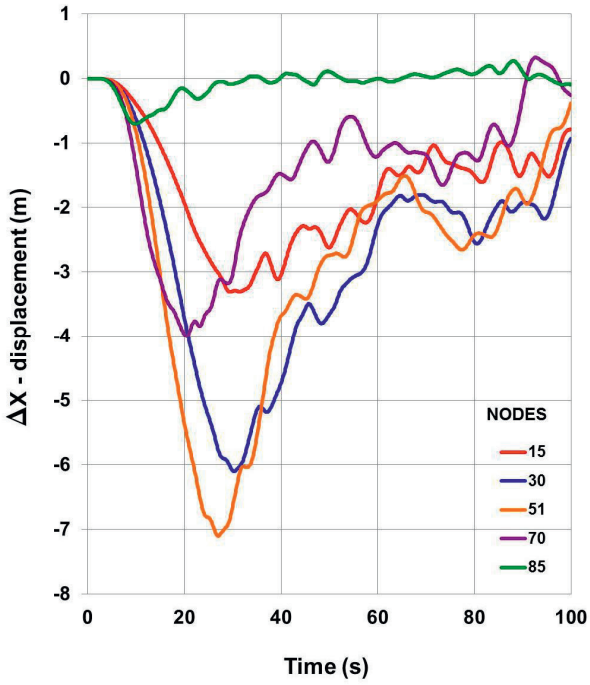

Figure 38. Time history of the ΔX displacements recorded during startup.

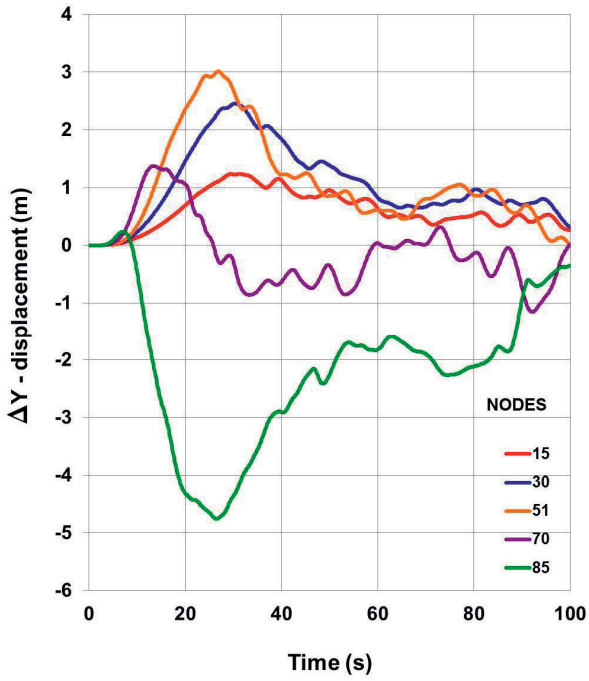

Figure 39. Time history of the ΔY displacements recorded during startup.

Deformations of nodes 51 and 85 for the last part of the simulation are shown in Figure 40 and Figure 41 (after 500 s) for the horizontal and vertical responses, respectively. Node 51, located in the middle of the riser, shows horizontal left and vertical upward displacements each time a slug is crossing. Thus, this node predominately experiences centripetal domain forces. Node 85 (region of liquid accumulation) is deforming horizontally to the right and vertically downward and thus primarily experiences gravity domain forces.

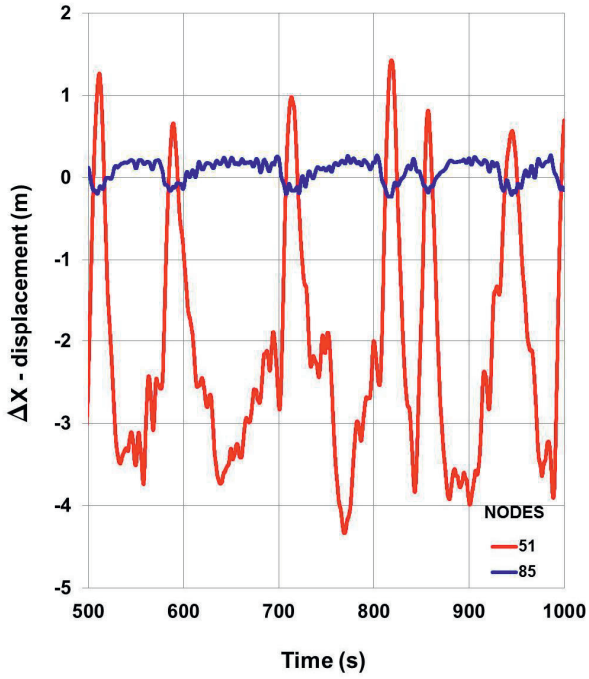

Figure 40. Time history of the ΔX displacements recorded during time integration.

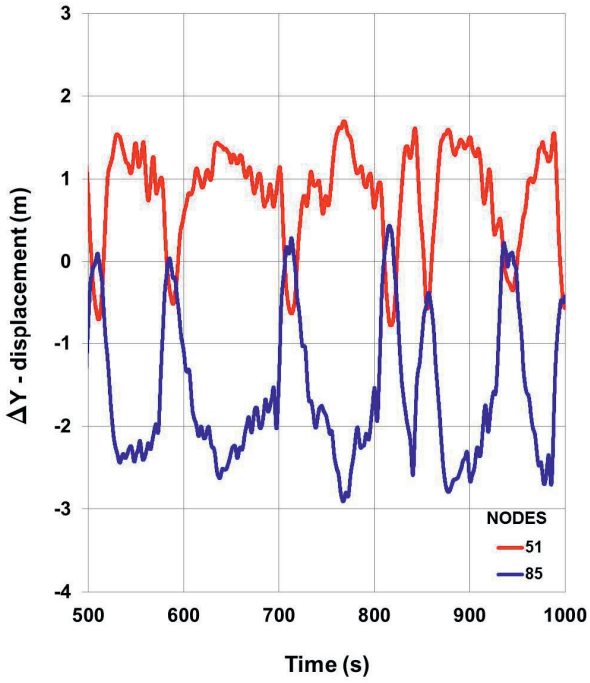

Figure 41. Time history of the ΔY displacements recorded during time integration.

In-plane displacements of the selected nodes are shown in Figure 42 for the startup period. A transition of node oscillations from the plane –x+y (nodes 15, 30, 51 and 70), crossing the plane –x-y (node 70) and up to the axis –y (node 85) is shown. The influence of the intense hitting of the two-phase flow jet stream at the characteristic point is observed (the flow jet stream generated this anticlockwise trajectory). Additionally, this graphic shows that after the initial deformation, each node tries to return to its static configuration.

Similarly, Figure 43 presents in-plane deformation of only two selected nodes during the entire simulation. In contrast to the startup, the nodes underwent smaller deformations, but similarly to the startup, the nodes tried to return to their static positions. These two graphs show that during the startup, the riser suffered the largest displacements.

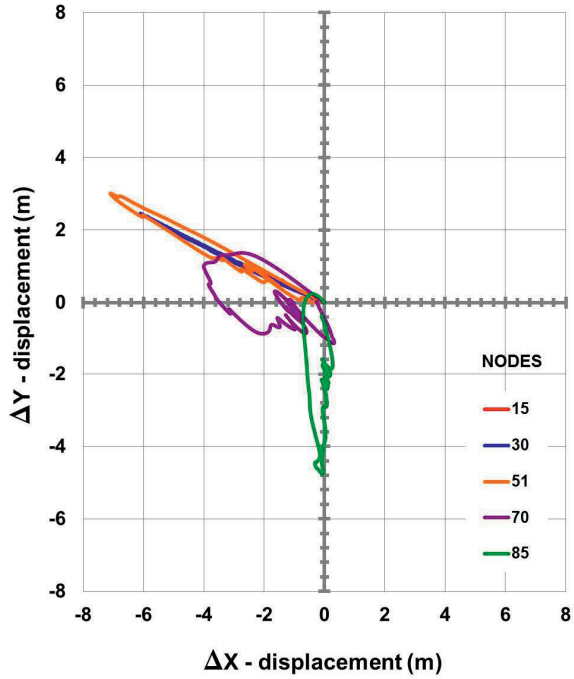

Figure 42. In-plane displacement of selected nodes recorded during startup.

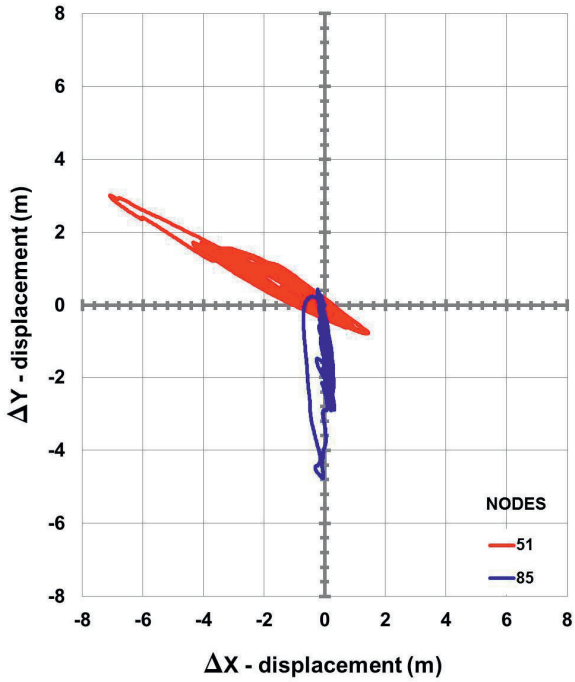

Figure 43. In-plane displacement of the selected nodes recorded during time integration.

A series of envelope figures is provided on the pages to follow. Envelopes of effective tension are presented in Figure 44. The hydrodynamic slug flow against a flexible riser produces a chaotic variation of the effective weight along the riser profile and in time because the non-homogenous dynamic distribution of the mass flow generated by the series of slugs traveling along the riser (the incompressible flow) alternates with the dynamic gas bubbles (the compressible flow). The effective tension increases (approximately doubles) during the startup and fluctuates throughout the remaining simulation period. This fluctuation is due to the random dynamic variation of the effective weights and the centripetal forces as the slugs and bubbles move along the riser.

Similarly, a considerable increase in the true tension can be observed in Figure 45. The highest increases are again recorded during startup, mostly as a consequence of the large increase in internal pressure. For the remaining simulation, the additional increase is due to the internal pressure fluctuation and the two-phase flow moment variation.

In this figure, a evident increment of the true tension can be observed along the region of the characteristic point and liquid accumulation zone for the remaining of the simulation. This situation is originated by the increase of the two-phase flow momentum at that area due to the liquid mass accumulation and the subsequent slug departure with a high velocity (slug generation).

The results shown in these last two figures have demonstrated that the slug flow produces an increase rather than a decrease in the effective and true tension of a flexible riser that initially was empty.

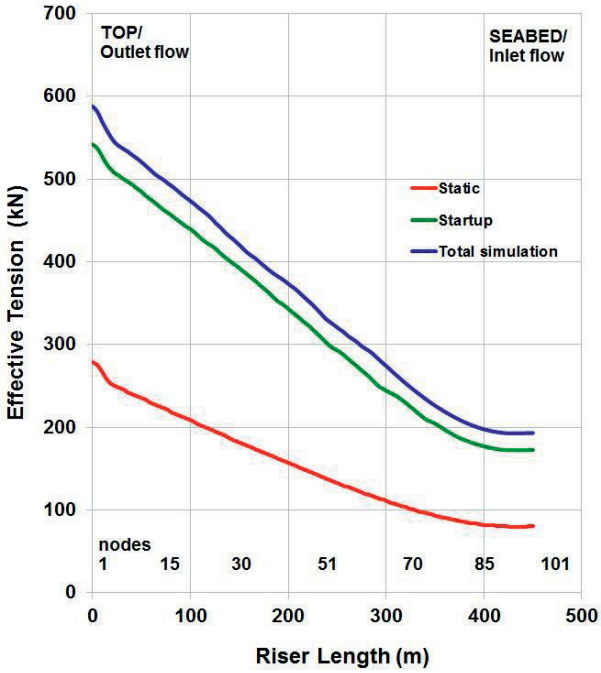

Figure 44. Envelope of the effective tension recorded during time integration.

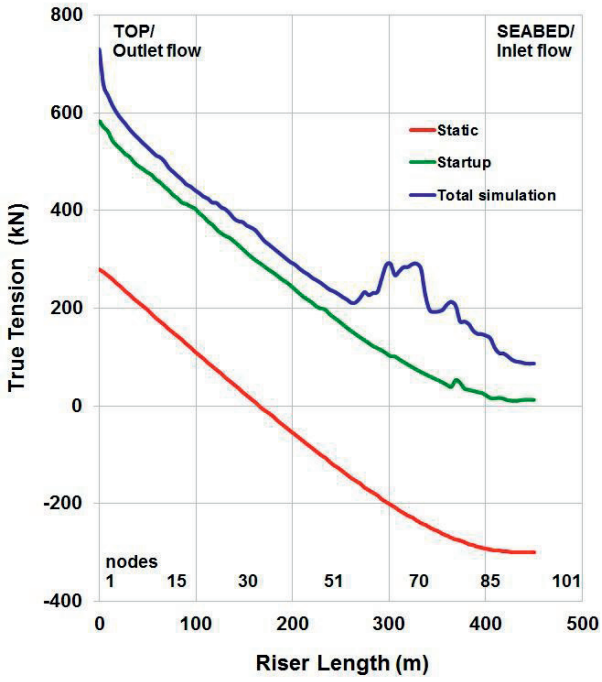

Figure 45. Envelope of the true tension recorded during time integration.

Regarding the bending moment, Figure 46 and Figure 47 present the maximum and minimum envelopes, respectively. Again, the highest variations of bending moment were recorded during the startup. Smaller variations were predicted for the remaining simulation. These variations occur mainly between the top of the riser and the characteristic point.

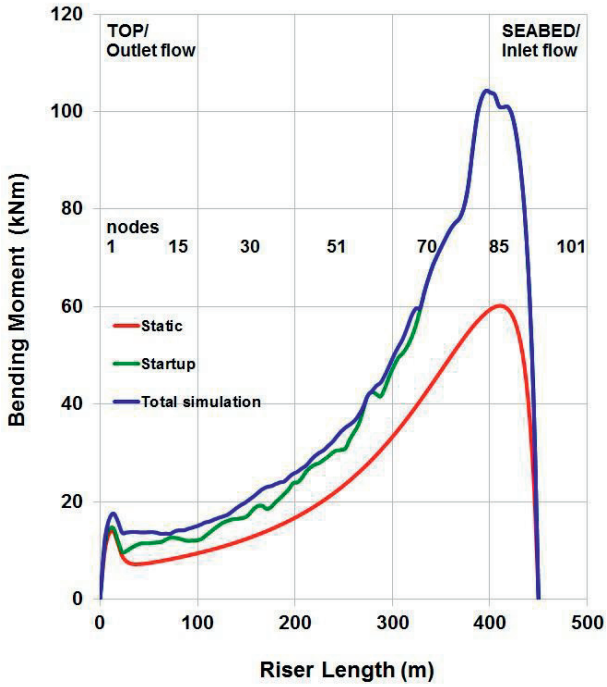

Figure 46. Envelope of the maximum bending moment recorded during time integration.

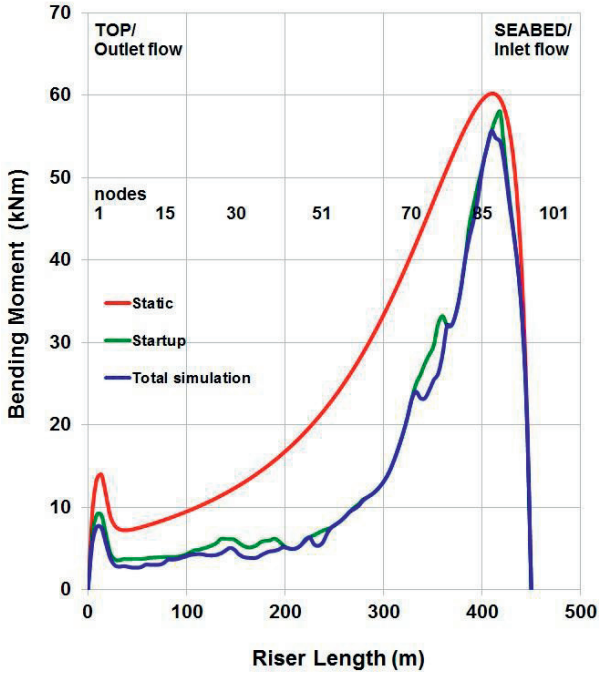

Figure 47. Envelope of the minimum bending moment recorded during time integration.

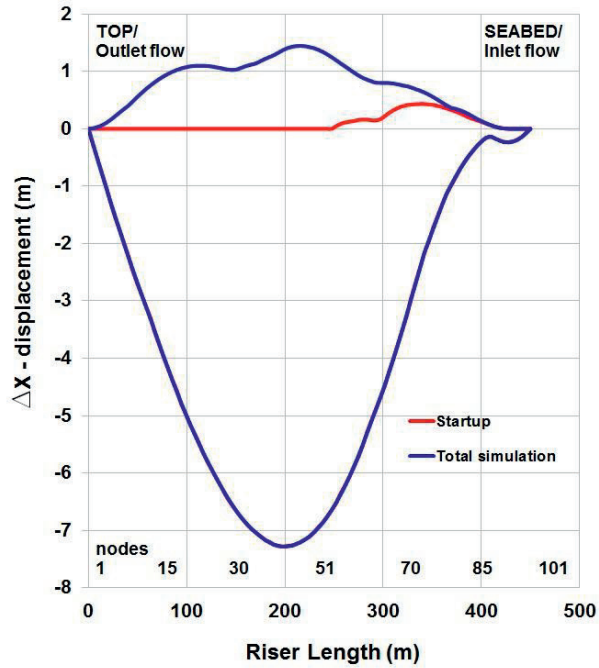

Figure 48. Envelope of the horizontal displacement recorded during time integration.

Figure 48 and Figure 49 show the envelopes of the maximum and minimum horizontal and vertical displacements along the riser. Again, the largest deformations are generated during startup. The influence of the slug generation zone and the characteristic point is also observed. These two graphs show that downstream from node 70, the riser is deformed on the plane –x+y. The centripetal force generated by the traveling slugs and bubbles exerted a greater influence. Upstream, the characteristic point of the deformation is mostly due to liquid accumulation for slug generation (gravity domain), as presented in Figure 49.

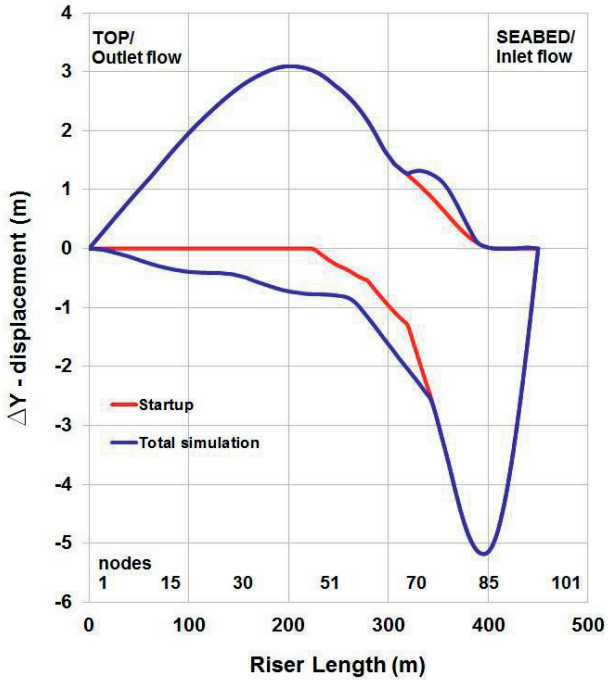

Figure 49. Envelope of the vertical displacement recorded during the time integration.

7.1.4 Discussion

The results demonstrated that the hydrodynamic slugs exhibit random and chaotic behavior; thus, irregular loads against the riser are generated, and the riser reacts by producing irregular responses. The increase and fluctuation of the effective tension resulted mainly from the centripetal force and the effective weight changes generated by the slug flow. Similarly, the true tension variation was attributed mainly to the internal

pressure variation, with a minor contribution from the two-phase flow momentum. Two regions separated by a characteristic point along the riser profile were also identified. One region was dominated mainly by centripetal forces, and the other region was dominated by gravity (the zone of liquid accumulation). Additionally, in this work, the highest variations (the displacements, tensions, bending moments and pressures) were recorded during the startup, with smaller variations thereafter.

7.2 Linear versus non-linear models for riser dynamics

7.2.1 Objective

The objective of this work is to conduct a numerical experiment to study the progress of unsteady slug flow through a hybrid riser and to analyze the influence of a linear and non-linear finite element model for the riser response on the riser dynamics and on the slug flow development. The interaction between the slug flow and the dynamic response of a hybrid riser is modeled by solving the fluid conservation equations (mass and momentum) for the internal two-phase flow and solving the dynamic equilibrium equation for the structure response. Additionally, the Morison equation is used to calculate external hydrodynamic loads on the riser during its oscillations in still water.

7.2.2 Case definition

A hybrid riser configuration subjected to slug flow has been selected to illustrate the difference between the results from linear and non-linear analyses of riser dynamics. This hybrid riser consists of a jumper of 600 m length, starting from the sea surface and followed by a rigid riser of 625 m ending at the seabed at a depth of 700 m. To establish this configuration, a horizontal force of 47.56 kN was applied to the top of the jumper. Similarly a force of 4000 kN was applied vertically at the top of the rigid riser and kept constant throughout the simulation, and finally, effective weights of 0.70 kN/m and 0.93 kN/m were distributed along the jumper and rigid riser, respectively.

Table 1 gives cross section data for the jumper and rigid part of the hybrid riser. One hundred elements of equal length were used for the finite element model discretization. The boundary conditions at the bottom end are defined as fixed positions but are free to rotate, which also applies at the top of the riser.

Mass flow rates of 10 kg/s for the gas and 200 kg/s for the liquid were imposed at the inlet of the hybrid riser for the transient two-phase flow under the isothermal conditions. Air and water were employed as the working media. The gas density behavior follows the ideal gas law, and for the water, a constant density of 998.78 kg/m^3 was assumed. A temperature of 290.15 K and a pressure of 1 atmosphere were considered as a reference. At the outlet of the hybrid riser, a pressure of 101.325 kPa was determined.

Hybrid Riser	**External Diameter (mm)**	**Internal Diameter (mm)**	**Axial Modulus of Elasticity (MPa)**	**Bending Modulus of Elasticity (MPa)**
Jumper	370	254	1.23E+4	4.89E+2
Rigid	364	316	2.07E+5	2.07E+5

Table 1 Hybrid riser – cross section data

The drag and added mass in still water were determined by the Morison equation. Both added mass and drag coefficients of 1.0 were used for these calculations. Sea water density equal to 1025 kg/m^3 was assumed.

The simulation began with the riser completely filled with gas and pressurized at 1 atmosphere. The riser profile, boundary and initial conditions were selected to provide the conditions for the generation of a series of random *hydrodynamic slugging*.

The simulation was run for 1000 seconds, following a synchronized HLA procedure. For the global riser dynamic program, a fixed time step of 0.1 s was used to maintain stability, and the two-phase flow code was implemented using a variable time step, computed according to the *CFL* criterion.

7.2.3 Results from simulation

Figure 50 represents the static configuration of the hybrid riser. This configuration was calculated by a non-linear finite element analysis before starting the

time integration. Figure 51 shows the distribution of the effective and true tension along the riser, as calculated by the static analysis. As the initial flow condition was an empty riser, the difference between the true and effective tension is due to the external pressure, according to Equation (6).

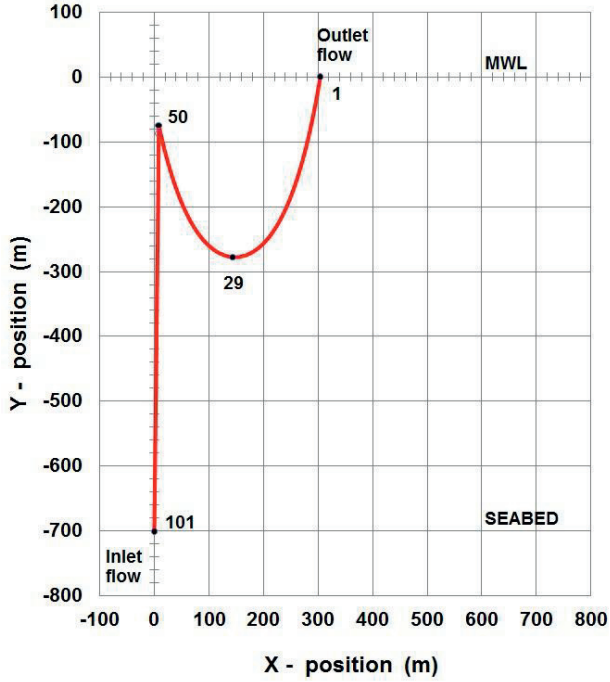

Figure 50**.** Hybrid riser static riser configuration.

Continuing with the static analysis, Figure 52 presents the static bending moment distribution. Because the boundary conditions include free rotations at the riser ends, zero bending moment was calculated at both ends and at the node representing the connection between the rigid riser and the jumper. The largest bending moment was predicted at the deepest point of the jumper (maximum curvature).

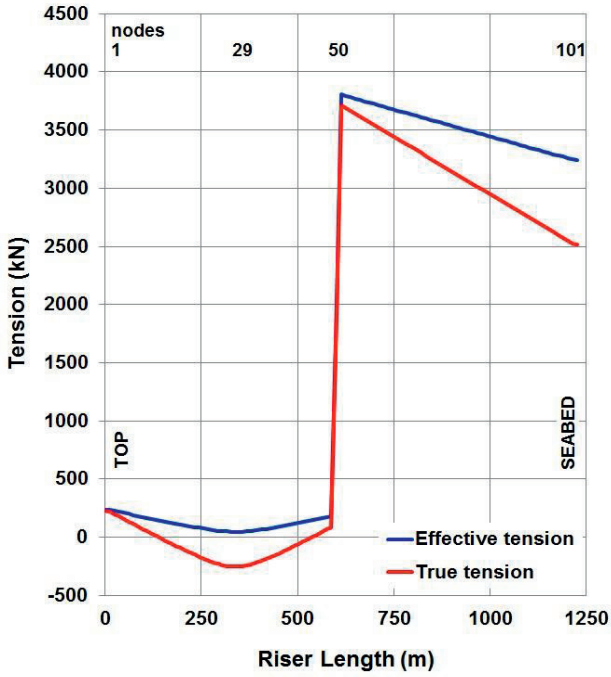

Figure 51. Effective and true tension distribution after static analysis.

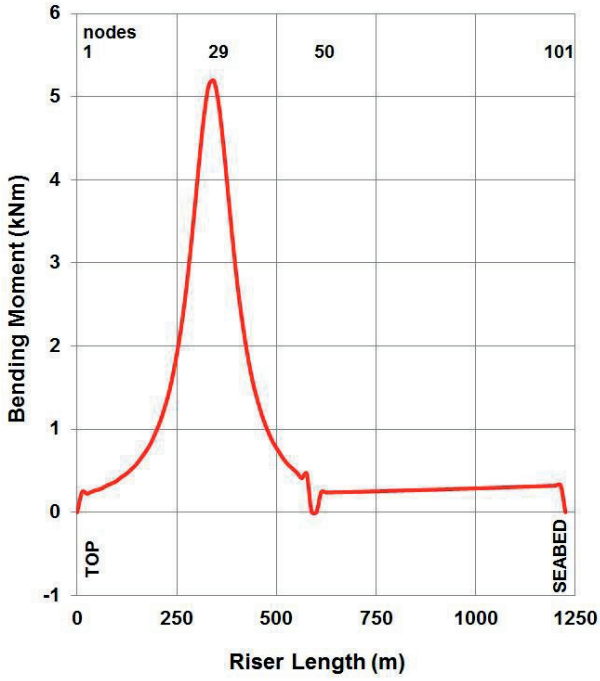

Figure 52. Bending moment distribution after static analysis.

To identify the difference between results from linear and non-linear calculations of riser dynamics on the coupled fluid-structure problem, the global riser dynamics program was run using both methods synchronized with the slug flow program. It is important to bear in mind that for both cases, the slug flow program solved the highly non-linear differential equations representing fluid conservation, see Equations (18) and (19).

The behavior of the inlet internal pressure during the time integration is shown in Figure 53 and Figure 54 for linear and non-linear simulations, respectively. A rapid increase in pressure as the slug flow approaches the riser is observed for both situations. The dynamic steady state flow is reached seconds after the first slugs cross the hybrid riser outlet. During this state, only fluctuations in the mean pressure are presented. This level of inlet pressure is necessary to maintain a continuous two-phase flow traveling along the hybrid riser for the selected geometry and boundary conditions. The pressure variations are caused by the transient changes in the two-phase flow momentum formed by the liquid slugs and gas bubbles. The shape and velocity of the slugs and bubbles change as they travel along the rigid riser and jumper.

Together with the inlet pressure, these figures also present outlet holdup development. The response of the linear approach generates a more stable slug flow, composed by a series of almost uniform traveling slugs. That situation is reflexed in the regular variation of the internal pressure. However, the response produced by the non-linear approach created the conditions for generating a more chaotic slug flow. Thus, Figure 54 presents non-uniform traveling slugs of different lengths. This situation generates the condition of more irregular fluctuations in the internal pressure.

Results will be presented on the following pages for the last part of the simulation, in order to avoid the influence of the transition from an unsteady to a dynamic steady state flow condition in the results.

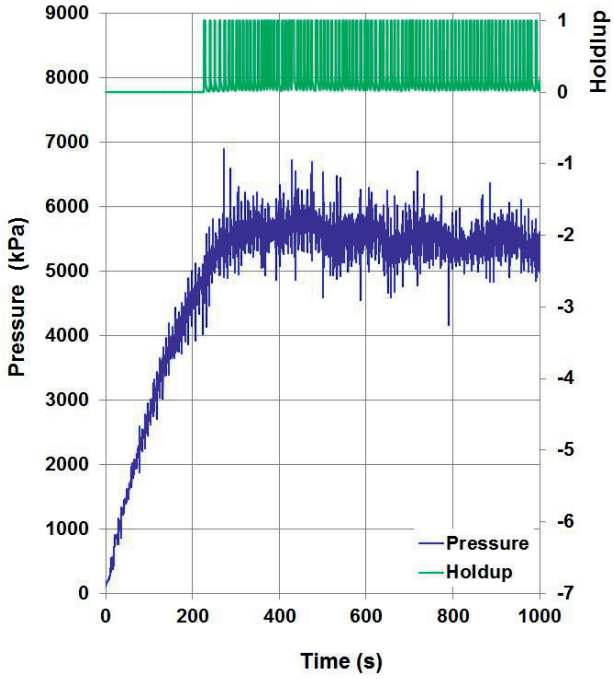

Figure 53. Time history of the internal flow inlet pressure – linear model.

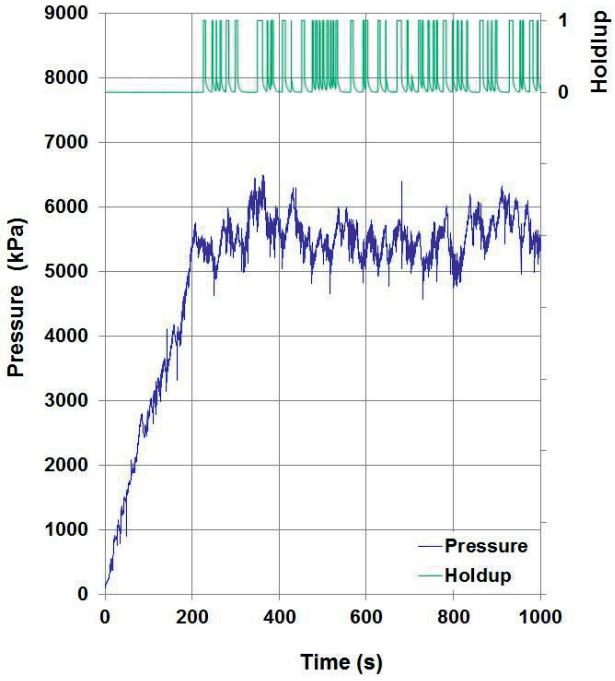

Figure 54. Time history of the internal flow inlet pressure – non-linear model.

The response calculated by the linear and non-linear approach strongly influences the development of the slug flow. That situation can be observed in Figure 55 and Figure 56, where the time histories of the liquid flow rate at the riser outlet for the last part of the simulation are presented. The flow rate is represented by its equivalent liquid superficial velocity.

A slug is crossing the riser outlet when the holdup reaches a value of unity, indicating that only liquid flow is produced. Based on the linear model (see Figure 55), uniform development of the holdup is predicted. On the other hand, for the non-linear model (see Figure 56), slugs with different lengths and shapes are generated. Hence, the two situations are observed to produce different liquid flow rate histories.

A similar effect is presented for the gas phase: see Figure 57 and Figure 58. The oscillation of the gas superficial velocity after a slug crosses the riser outlet is caused by the compressible flow on the gas density.

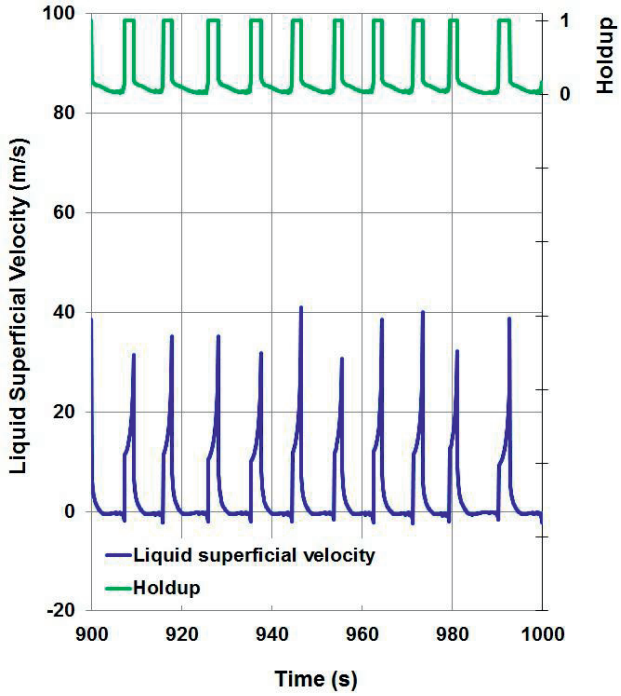

Figure 55**.** Time history of the outlet liquid flow rate - linear model.

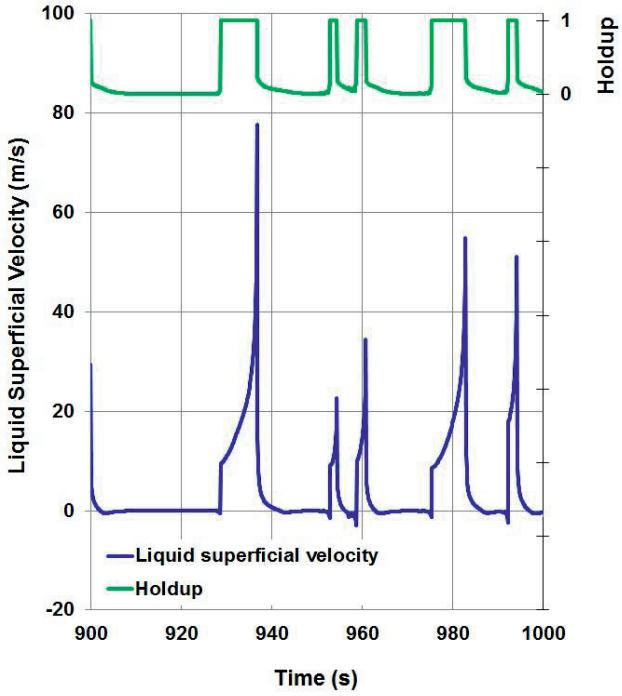

Figure 56. Time history of the outlet liquid flow rate – non-linear model.

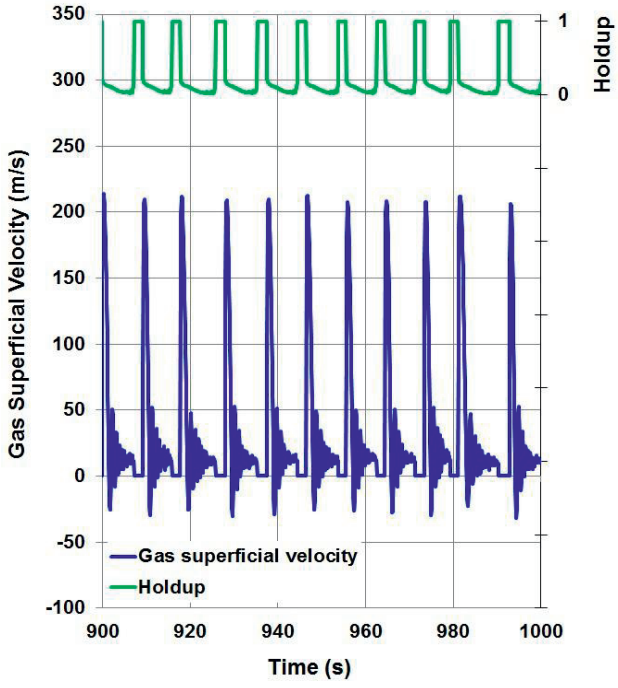

Figure 57. Time history of the outlet gas flow rate - linear model.

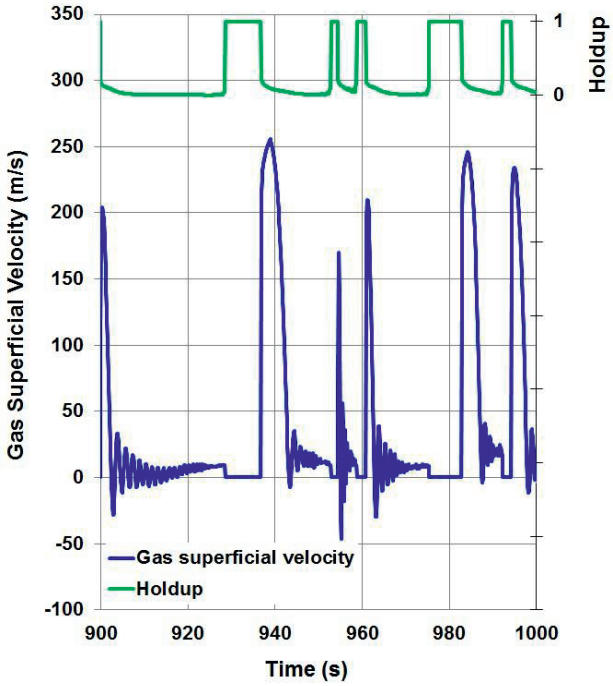

Figure 58. Time history of the outlet gas flow rate – non-linear model.

The forces on the riser generated by the slug flow are represented by the generation of the centrifugal force and the variation in the effective weight. The riser counteracts these forces by varying the effective tension. A linear model of the DEQ is not able to capture the influence of this variation on the stiffness matrix. The resulting effective and true tension variation and holdup for the linear model is shown in Figure 59. In contrast, the non-linear analysis can account for the stiffness variation caused by varying the effective tension, which leads to the results shown in Figure 60. The linear simulation calculated short effective tension oscillations that follow the slug flow development (almost a regular series of traveling slugs). In contrast, the non-linear model presents higher and irregular variation of the effective tension.

The true tension that also appears in these figures follows the slug flow development for both models. As the results presented in these two last figures come from the top of the riser, the true tension variation is mainly due to the change in the two-flow momentum, see Equation (6). Certainly, the linear and non-linear simulations estimate different dynamic riser shapes for the slug flow program, which in turn lead to different developments of the slug flow. The slug flow calculated by using non-linear

analysis is observed to be the most chaotic. Furthermore, incorrect values of the true tension may have been predicted for the linear model due to its missing capability to capture the influence of the effective tension variation on the stiffness matrix and its limitation to managing only short riser responses. This situation invalidates the use of data from a linear simulation in a stress analysis.

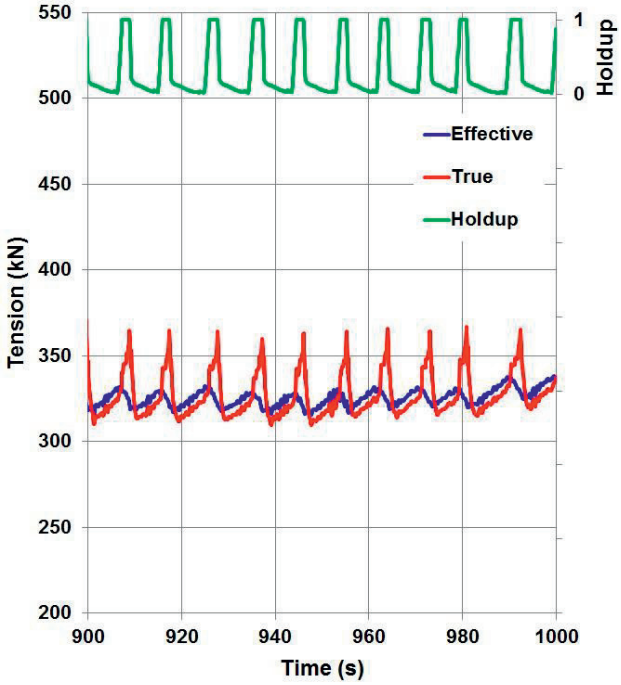

Figure 59. Time history of the top tensions - linear model.

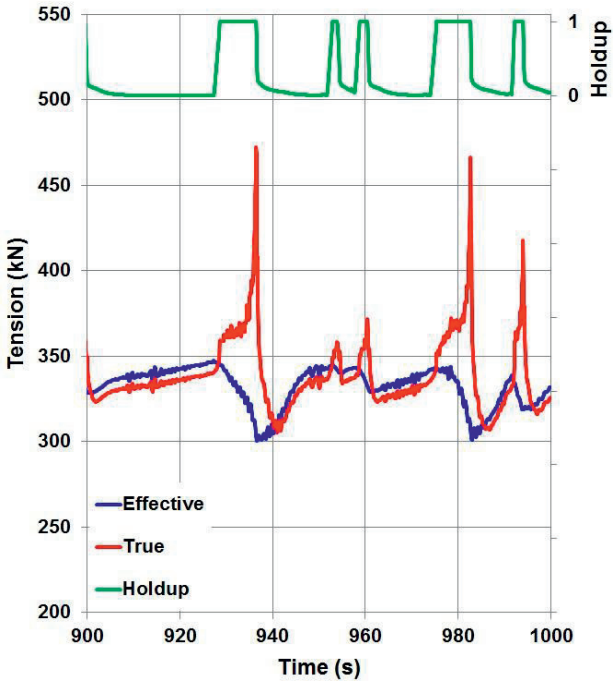

Figure 60. Time history of the top tensions - non-linear model.

Another important influence of the slug flow on the riser dynamics is the change in the effective weight. The simulations show a high variation of the effective weight as a slug flow propagates along the riser in an irregular manner. The slug flow is characterized by a continuous variation of liquid and gas mass flow rate distribution in the riser. Figure 61 and Figure 62 show time histories of the effective weight recorded at the deepest point of the jumper for the linear and non-linear analyses, respectively. The effective weight follows the slug flow development, as in the case of the true tension. Even if the variation of the effective weight along time is different for the two cases (from almost regular to more chaotic) the maximum and minimum values are the same because the extreme values indicate that the riser cross section is completely occupied by a liquid or gas phase. The effective weight variation and the centripetal force are the results of the slug flow in the riser, and the riser counteracts by changing the effective tension.

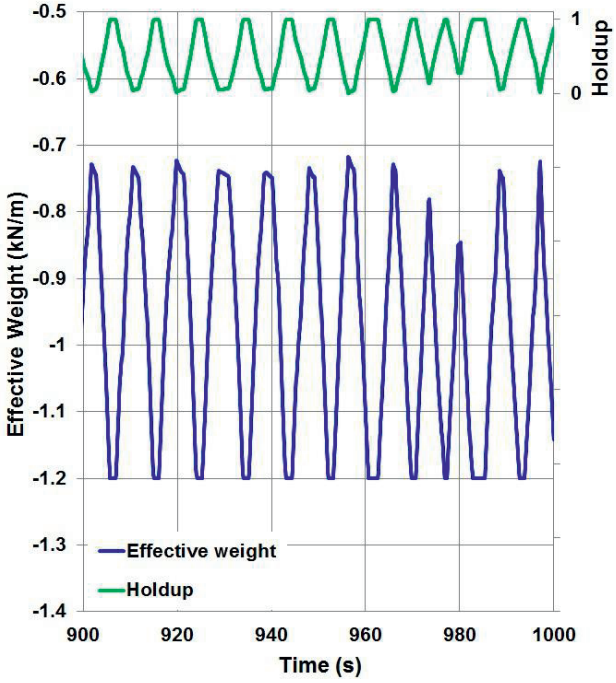

Figure 61. Time history of the effective weight - linear model.

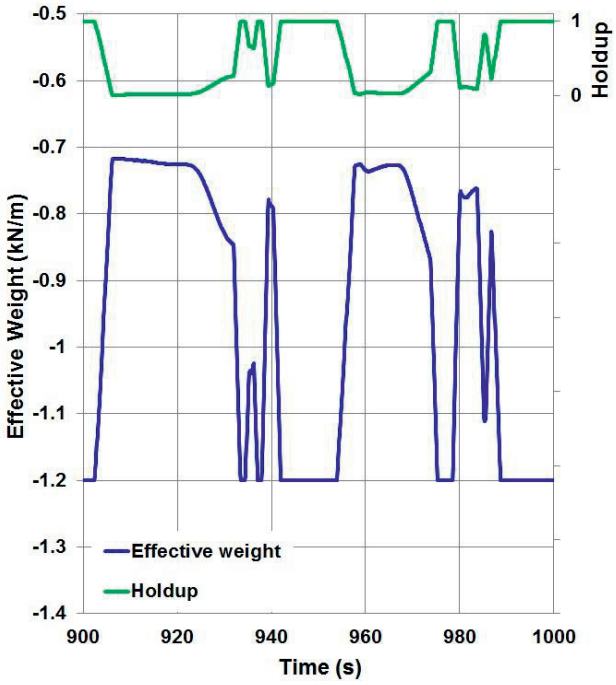

Figure 62. Time history of the effective weight – non-linear model.

Figure 63 and Figure 64 present the time histories of bending moments at the deepest point of the jumper from the two analysis procedures. The bending moment begins to change as the slug flow approaches the riser from the inlet (node 101) to the outlet (node 1). The bending moment variations follow the slug flow development irregularly for both cases. Characteristic amplitudes are higher for the linear analysis than for the non-linear, but the most important difference is that linear analysis gives almost periodical response, while the non-linear response is more stochastic.

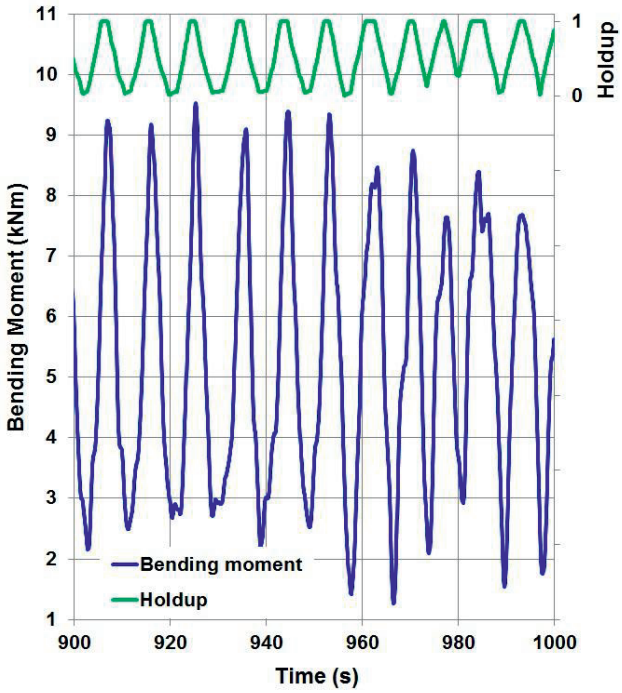

Figure 63. Time history of the bending moment – linear model.

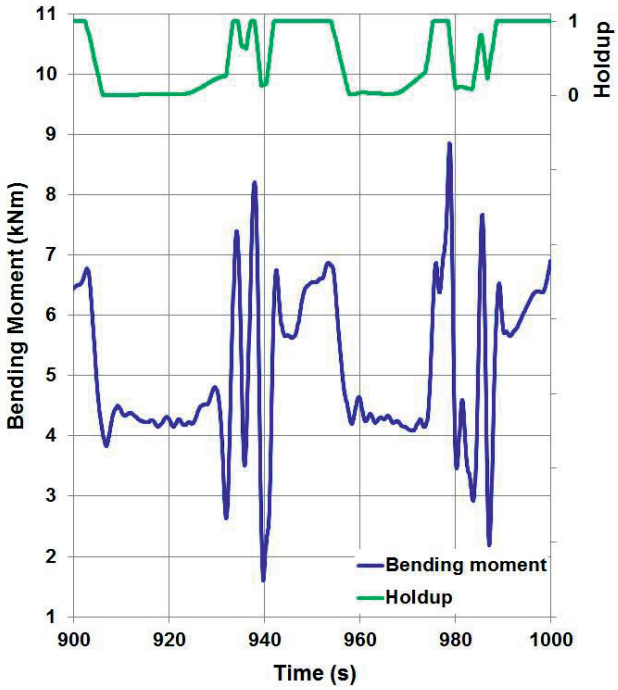

Figure 64. Time history of the bending moment – non-linear model.

The non-linear analysis shows a more irregular response. The modes presents by the non-linear model have low eigenfrequencies. This situation will not occur for the linear analysis, but will be present for the non-linear due to the character of the loads. The Linear analysis shows load periods of approximately 10 s, in contrast the non-linear analysis presents characteristic periods of 30 s.

The interaction between the slug flow and the riser structure generates irregular deformation time histories. This behavior is typical of risers with slug flow because this phenomenon itself has an irregular and unstable behavior. Figure 65 and Figure 66 show the deformation time histories at the deepest point of the jumper in the x and y directions from linear and non-linear simulations. Only small deformations were produced by the linear model, in contrast to the large displacements from the non-linear case. These large deformations are originated by the chaotic behavior of the slug flow due to the non-linear riser response provided by the riser dynamics code to the slug flow program. If this type of two-phase flow behavior occurs for the linear case, linear dynamic analysis would be unable to calculate such large displacements in a credible manner.

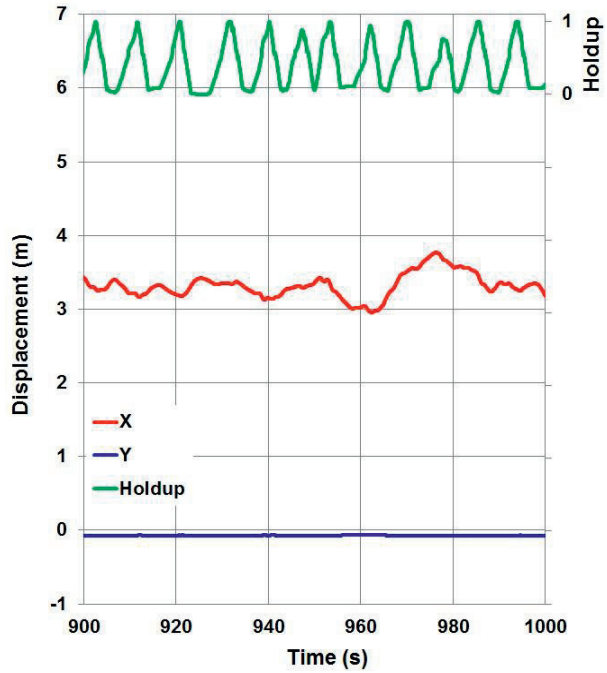

Figure 65. Time history of the X, Y displacements recorded at node 29 – linear model.

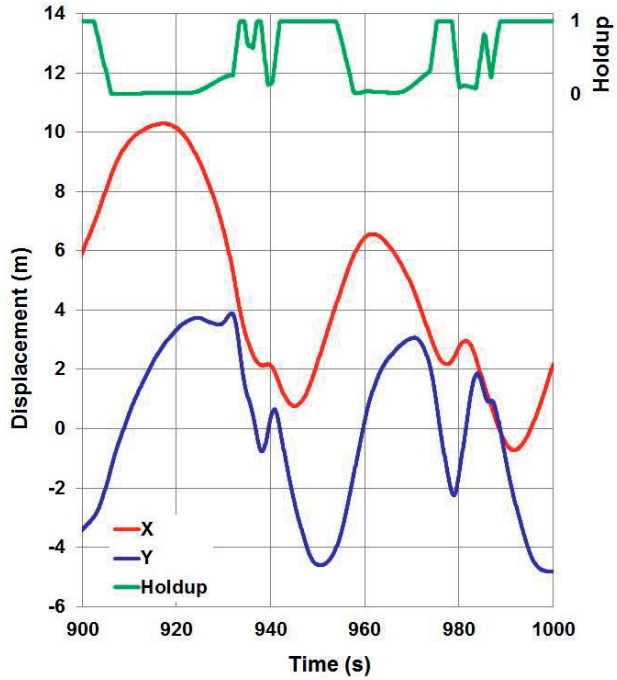

Figure 66. Time history of the X, Y displacements recorded at node 29 – non-linear model.

The non-linear case generated slugs of varying sizes, and the largest slugs led to stronger inertia effects on the jumper after its deepest point. On the other hand, a series of slugs of similar magnitude travelling continuously along the entire hybrid riser for the linear case did not lead to similar response amplitudes.

The deformations at the top of the rigid riser are shown in Figure 67 and Figure 68. Horizontal displacements with large fluctuations are presented for the non-linear case, while the linear case shows horizontal displacements with minor fluctuations. The vertical displacements for both cases are almost zero due the tension at the top of the rigid riser.

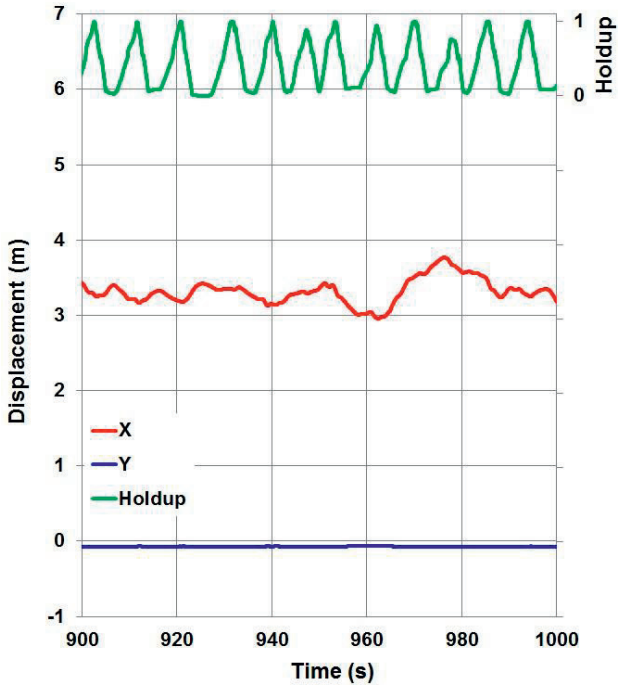

Figure 67**.** Time history of the X, Y displacements recorded at node 50 – linear model.

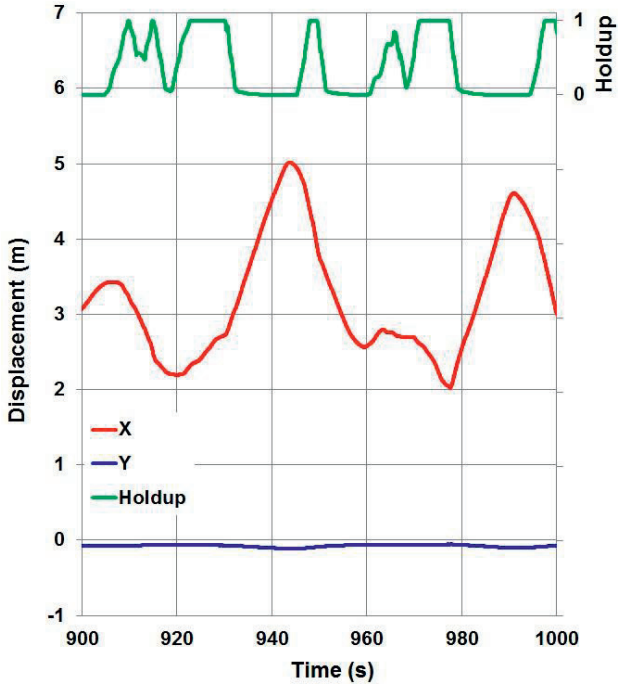

Figure 68. Time history of the X, Y displacements recorded at node 50 – non-linear model.

In-plane displacements of the deepest point of the jumper and the top point of the rigid riser are shown in Figure 69 and Figure 70, respectively. It is clearly seen the largest riser responses originated from the non-linear response model. The non-linear model generates larger displacements in the xy plane than the linear model. A similar situation can be observed at the top point of the rigid riser; however, this point has a predominant horizontal displacement for obvious reasons.

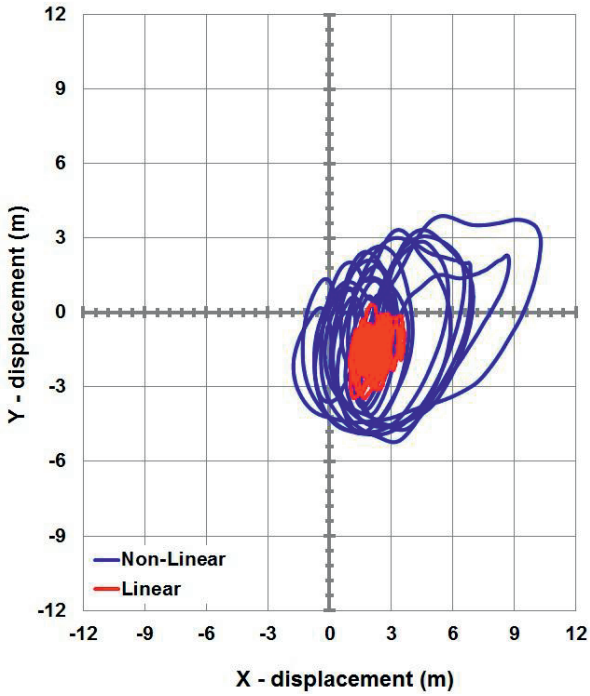

Figure 69. In-plane displacement at the deepest point of the jumper.

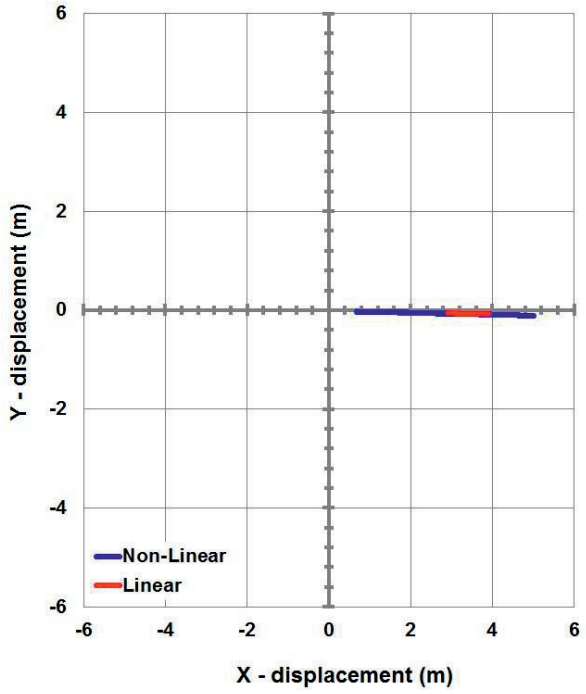

Figure 70. In-plane displacement at the top point of the rigid riser.

A series of extreme values are provided in the next several figures, which have been recorded between 500 s and the end of the simulation. Maximum values of effective tension are present in Figure 71 for both cases. The hydrodynamic slug flow traveling through a riser produces a chaotic variation of the effective weight in time and space due to the varying distribution of the mass flow generated by the slug flow. The linear model is to some extent able to capture the effective tension variation, but bear in mind that this variation will not influence the stiffness matrix. Figure 71 shows the same trend of variation in effective tension for both cases. An increment of effective tension is predicted in the jumper and a decrement in the rigid riser. Similarly, Figure 72 shows an increase in the true tension in the hybrid riser for both models. This situation is mainly due to the two-phase flow momentum and the internal pressure, which increase the true tension.

Figure 73 presents the envelope of the bending moment for both methods. The two results show the same trends of bending moment variation in both directions. Clearly, the linear model underestimated the bending stresses.

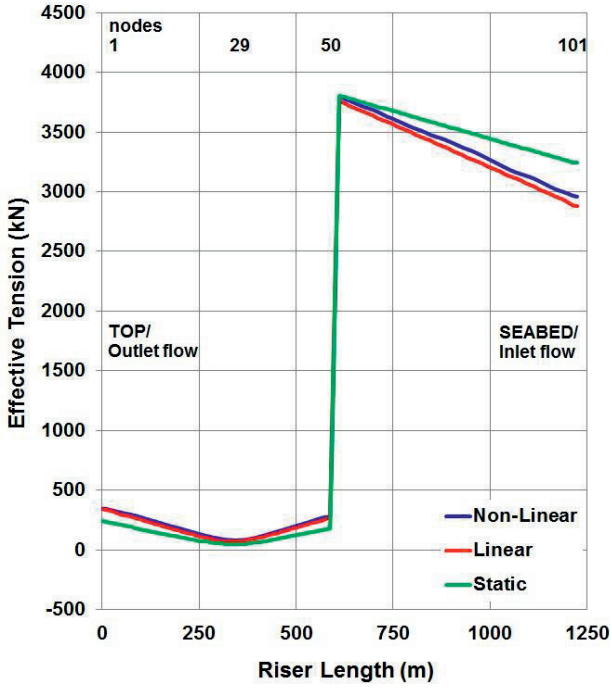

Figure 71. Maximum values of the effective tension recorded during time integration.

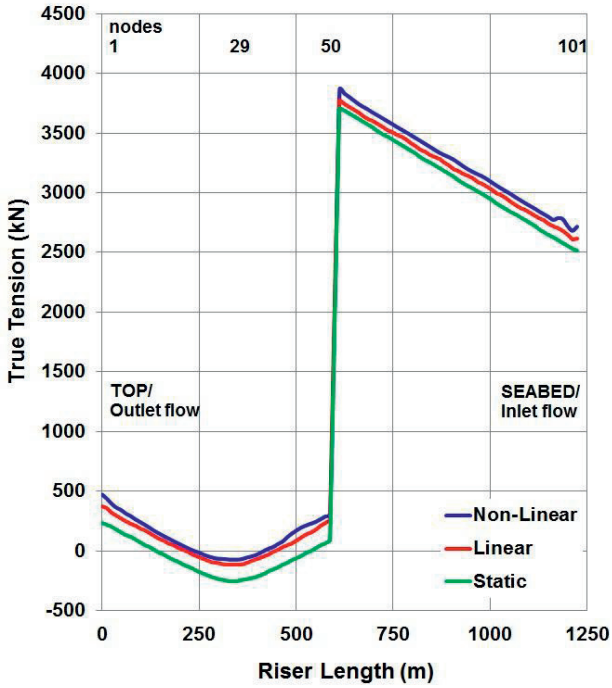

Figure 72. Maximum values of the true tension recorded during time integration.

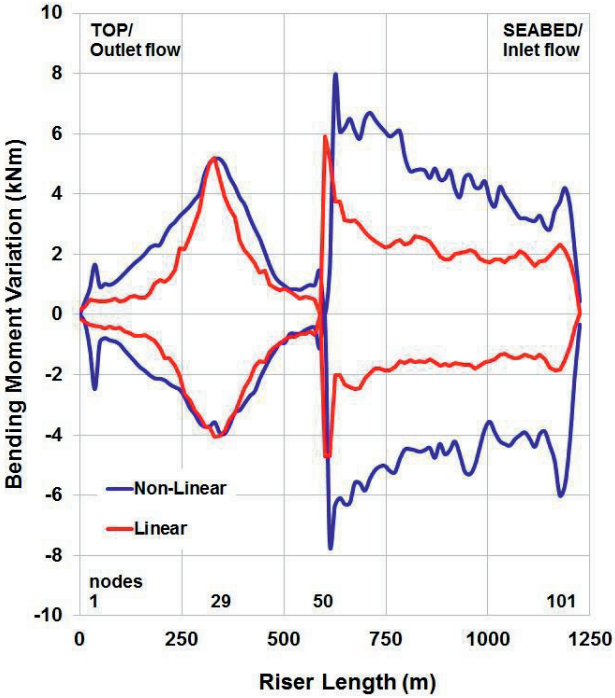

Figure 73. Envelope of the bending moment recorded during time integration.

Figure 74 and Figure 75 show the envelopes of horizontal and vertical displacements along the hybrid riser, respectively, for both methods. The largest displacements were generated at the jumper as expected. However, only the non-linear method was able to capture the largest deformations. As commented above, the non-linear DEQ created the condition for a more chaotic slug flow, and thus, the two-phase flow generated stronger centrifugal forces on the hybrid riser.

The horizontal displacement, shown in Figure 74, presents the largest displacements between the deepest point of the jumper and the upper end for both simulations, but the displacements are far larger for the non-linear analysis than for the linear analysis. The largest slugs generated during the non-linear simulation must overcome the downstream internal hydrostatic pressure when travelling by the deepest point of the jumper to continue flowing. Thus, the bubble upstream of these slugs is compressed, and its internal pressure becomes higher than the slug downstream internal pressure. Upon reaching that condition, the slug rises (blows out) with high velocity, thereby generating high centrifugal forces against the jumper. For the vertical displacement, Figure 75, gravity domain forces were more predominant for the linear model case. It is important to have a reliable prediction of the riser displacements to define spacing and thereby avoid collision between risers in an array on deep water.

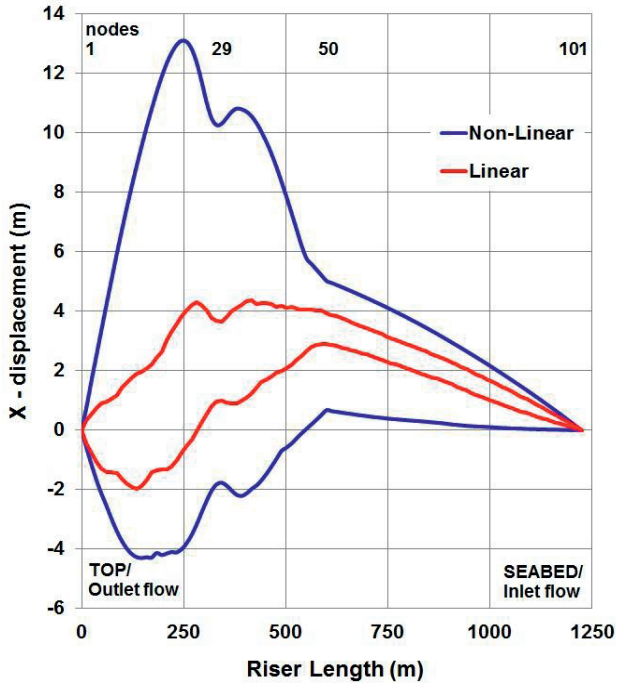

Figure 74. Envelope of the horizontal displacement recorded during time integration.

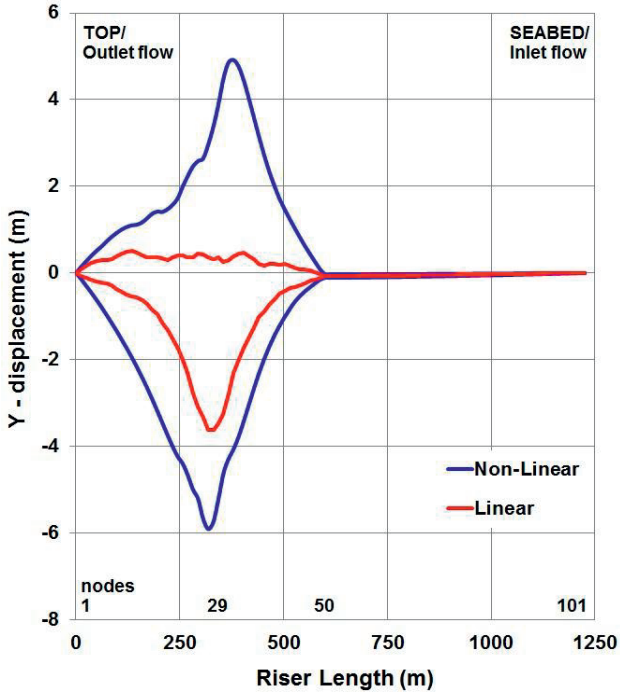

Figure 75. Envelope of the vertical displacement recorded during time integration.

The envelopes of the liquid and gas flow rates are presented in Figure 76 and Figure 77, respectively, for both cases. The highest liquid flow rate is predicted in the jumper for the non-linear simulation. The liquid flow rate is directly related to the liquid /slug velocity. The non-linear analysis generates more chaotic slug flow and also higher velocities, hence producing higher flow rates. A similar situation occurs for the gas flow rate. The two-phase flow development is observed to be strongly related to the riser response, and the external loads generated by the slug flow depend on its development.

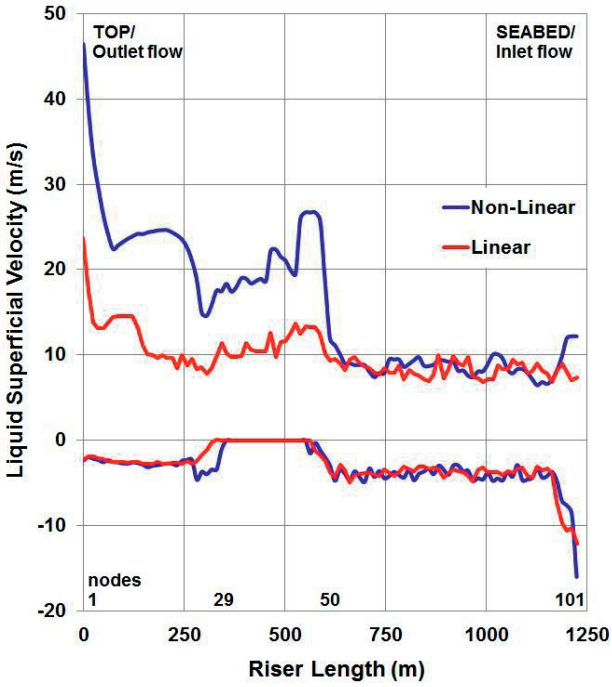

Figure 76. Envelope of the liquid flow rate recorded during time integration.

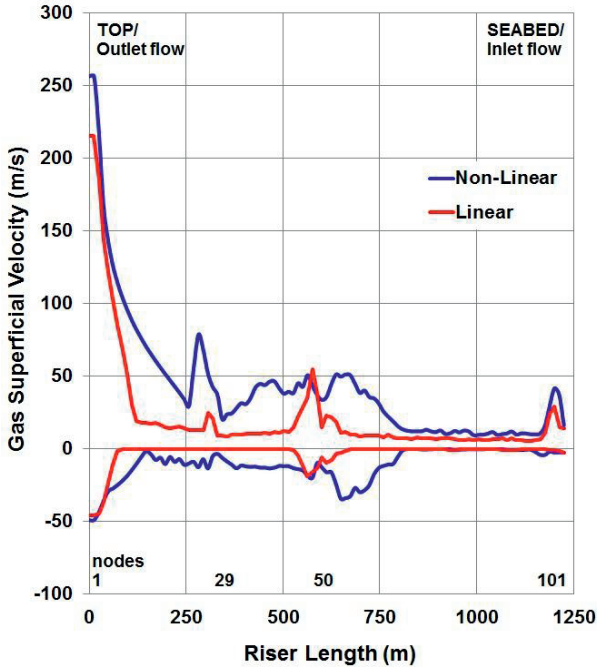

Figure 77. Envelope of the gas flow rate recorded during time integration.

7.2.4 Discussion

The main difference between the linear and the non-linear analysis is seen in the time histories of the previous figures. The non-linear model presents more irregular and longer characteristic periods which gives less high frequency vibration, but lower modes will be excited. The non-linear response is seen not to give a periodic solution. This might be caused by non-linear effects that may encourage other frequency components to occur, and then change that internal two-phase flow dynamics. The non-linear simulation capture this effect, but the linear model does not. The linear model presents almost a perfect periodical response pattern.

The linear riser response model will tend to under-predict the dynamic response as the observed variation in time of the effective tension is not reflected in the stiffness matrix. This result contrasts with the non-linear simulation, where changes in global geometry and effective tension will influence the stiffness matrix and thereby lead to a more chaotic dynamic response. Additionally, despite the ability to calculate the effective tension variation for the linear analysis, the results are suspected to be

incorrect due to the capacity of the linear model to work only with short responses. The different riser responses predicted by each model also influenced the slug flow development. The linear case generated a more regular development and the non-linear case a more chaotic behavior of the slug flow. Hence, the use of a linear model for this type of analysis is not recommended.

7.3 Validation against experiments

7.3.1 Objective

The objective of this test case is to validate the numerical results of the computer *federation* against experimental data and then to take advantage of the numerical simulation to obtain additional information that is difficult to obtain experimentally to gain a better understanding of the mechanics of this slug flow – riser dynamics interaction.

7.3.2 Experimental Facility

The following description of the laboratory test facility comes from the work of Valdivia et al. [5]. A laboratory-scale model was designed based on a steel catenary riser (prototype) of 1600 m submerged in a water depth of 900 m. The Buckingham-Pi theorem was applied to determine the dimensionless parameters for the scale reduction (geometry, structural and flow variables). The model consists of one horizontal section, lying on the floor, and one catenary-shaped section, suspended from the ceiling.

Figure 78 shows the components of the test facility. Water is supplied by a tank installed on the terrace of the laboratory, feeding a pump on the ground floor that pressurizes the liquid before it passes through a flow-meter. After this device, the water enters an injector. On the other side, a rotating compressor supplies pressurized air. The air flow rate is measured by a flow-meter before it is directed to the injector. The injector consists of a mixer and a transparent outlet pipe for visualization. The fluids leave the injector as a two-phase flow. Downstream, the two-phase flow enters the catenary riser model.

Five target points are positioned along the riser. The displacements of these points are captured by five cameras. The images are then processed to yield the frequency and amplitude of the oscillations. The top of the riser model is held up by a load-cell, which provides the assessment of the top tension. The load-cell is connected

to its frame support by a pin-joint designed to allow variations in the top angle of the catenary under dynamic loading.

The two-phase flow exits the riser model after the load-cell through a tube returning to the water tank, where the gas is vented to the atmosphere and the liquid is reinserted into the facility. All the signals generated by the instruments are transmitted to the data acquisition systems, where they are stored for later processing and analysis.

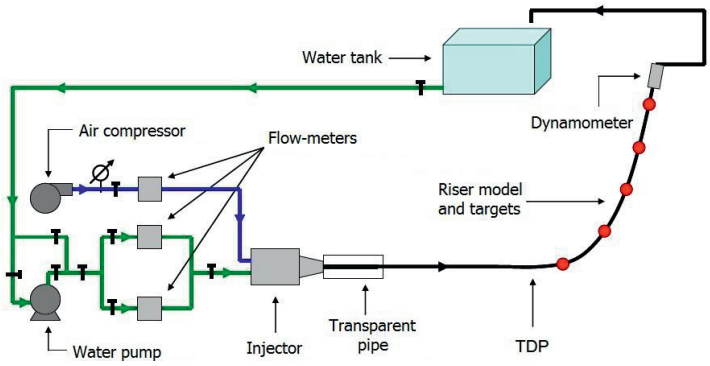

Figure 78. Arrangement of the experimental facility**.**

7.3.3 Results from simulations and validations

To validate the results of the HLA federation, the predicted response of a riser was compared against the experimental data from the work of Valdivia et al. [5]. The experimental model consists of a hose 28.7 m in length beginning as a horizontal line of 10.7 m ending at the touch down point (TDP). Then, a free-hanging line 18 m in length follows it, ending at the top of the riser. The model was established in air so that hydrodynamic effects (drag and added mass) do not have any influence. The hanging part of the riser has a horizontal and vertical projection of 11.5 m and 12.5 m, respectively.

According to the work of Valdivia et al. [5], the material selected for the riser model was silicone (specification 60/65 SHORE A) with a modulus of elasticity of 1255 kPa and a mass of 0.254 kg/m. The riser model has external and internal diameters of 0.025 m and 0.019 m, respectively.

In our work, to set up the riser configuration, a horizontal force of 15.4 N was applied at the top of the riser, and an effective weight of 2.5 N/m was distributed along the riser. One hundred elements of equal length were used for the finite element model.

The boundary condition at the touchdown point is considered fixed but free to rotate, which also applies at the top of the riser model.

Following the experimental procedure, superficial velocities of 0.55 m/s for the gas and 0.55 m/s for the liquid were imposed at the inlet of the horizontal line for the transient two-phase flow under isothermal conditions. Air and water were employed as the working substances according to the work of Valdivia et al. [5]. Thus, water was considered to have a density of 998.78 kg/m^3, and the air density was assumed to follow the ideal gas law. Additionally, a temperature of 290.15 K and a pressure of 1 atmosphere were used as a reference. At the outlet of the riser, a pressure of 101.325 kPa was set to represent an open water reservoir. These properties and boundary conditions were considered for the numerical simulation to obtain a good representation of the experiment.

The simulation began with the riser completely filled with gas and pressurized at 1 atmosphere. The riser profile, boundary and initial conditions provided the conditions for the generation of a series of random *hydrodynamic slugging* similar as reported by Valdivia et al. [5].

The distributed simulation was run for 300 seconds, following a parallel and synchronized HLA procedure. For the riser dynamics program, a fixed time step of 0.1 s was used to maintain stability, and the two-phase flow code used a variable time step to capture the information traveling with the flow velocity.

Figure 79 represents the static configuration of the catenary riser model. This configuration was calculated by a non-linear finite element method before beginning the simulation. The static riser profile matches the initial riser profile of the model. The location of node 62 can be observed in the figure. This node represents the position of the target point of camera 3 in the work of Valdivia et al. [5]. The predicted deformations of the riser model at this node will be validated in this work.

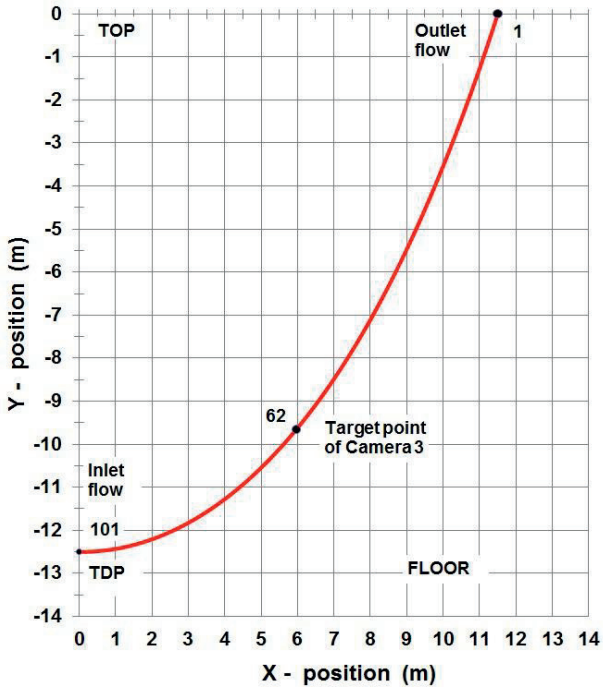

Figure 79. Riser model static configuration.

The static analysis also generated the following load profiles. Figure 80 shows the distribution of the effective and true tension along the riser. These tensions present the same load distribution as the initial condition is a dry riser outside the pool. Under these conditions, the effective tension is a consequence of the riser's own weight. Figure 81 presents the bending moment distribution before beginning the dynamic analysis. As the boundary conditions include free rotation at the riser ends, zero bending moment was calculated at these positions. The largest peak of the bending moment was predicted to be closer to the TDP.

Figure 80. Effective and true tension distribution after static analysis.

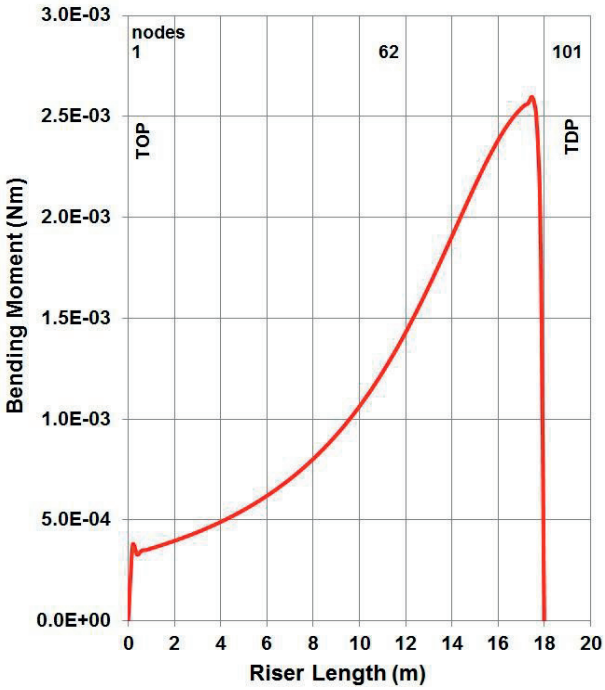

Figure 81. Bending moment distribution after static analysis.

The behavior of the internal pressure at the TDP during the time integration is shown in Figure 82 for the numerical simulation. The two-phase flow begins traveling along the horizontal pipe from the riser inlet. The internal pressure begins to grow when the slug flow reaches the TDP. A rapid increase in pressure is observed as the slug flow fills up the riser. The dynamic steady state flow is reached when the first slugs cross the riser outlet. During this state, only fluctuations in the mean pressure are presented. This level of inlet pressure is necessary to maintain a continuous two-phase flow rate along the riser for the defined configuration. The pressure variations are caused by transient changes in the two-phase flow momentum formed by liquid slugs (incompressible fluid) and gas bubbles (compressible fluid).

Together with the internal pressure, these figures also present the outlet holdup development. Chaotic slug flow development was predicted, and thus, the simulation presents non-uniform traveling slugs of different lengths and velocities. The shape and velocity of the slugs and bubbles change as they travel along the riser. This situation generates the conditions for irregular fluctuation of the internal pressure.

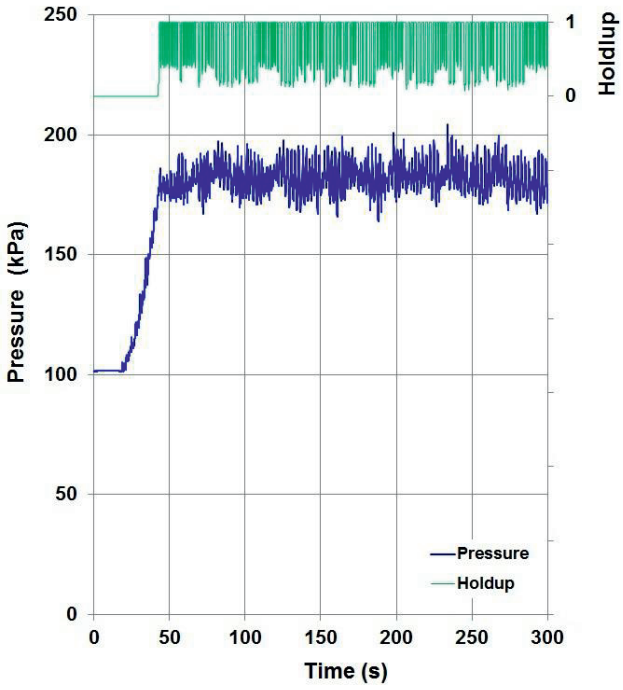

Figure 82. Time history of the internal flow inlet pressure.

Next, the numerical results will be presented for the last 120 s of the simulation, distant from the unsteady state flow period, to avoid the influence of the transition from unsteady to dynamic steady state flow in the results, the 120 s range will be applied for validation against the experimental results presented by Valdivia et al. [5].

The forces produced by the slug flow against the riser structure are represented by the generation of dynamic centrifugal forces and the variation of the effective weight. The riser counteracts these forces by an increase of the effective tension. The tension at the top of the riser registered by the dynamometer (load-cell) during the test is shown in Figure 83. Similarity, the effective tension at the top of the riser predicted by the simulation is shown in Figure 84. The tension recorded from the experiment is slightly higher than the tension predicted by the computer simulation. However, both results present a similar range of force variation. A similar behavior can be observed in Figure 85 and Figure 86, experimental and numerical results, respectively, for an additional test where the gas superficial velocity was reduced to 0.12 m/s.

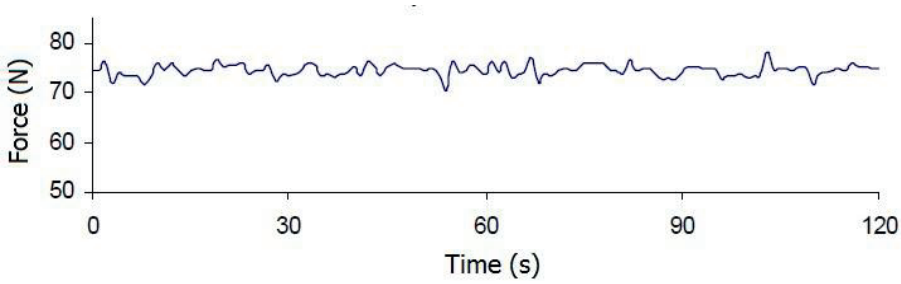

Figure 83. Time history of the top tension from experiment.

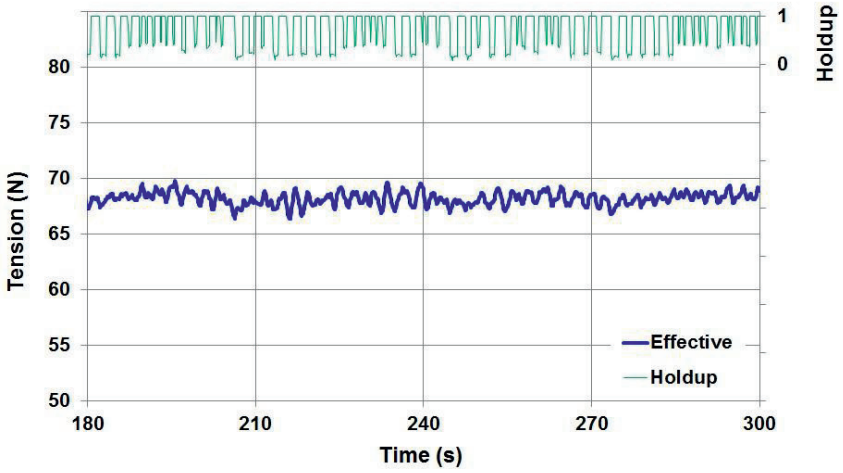

Figure 84. Time history of the top tension from numerical simulation.

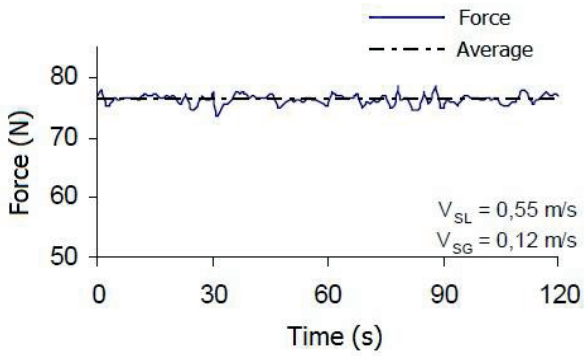

Figure 85. Time history of the top tension, Usl=0.55 m/s Usg=0.12 m/s, from experimental measurement.

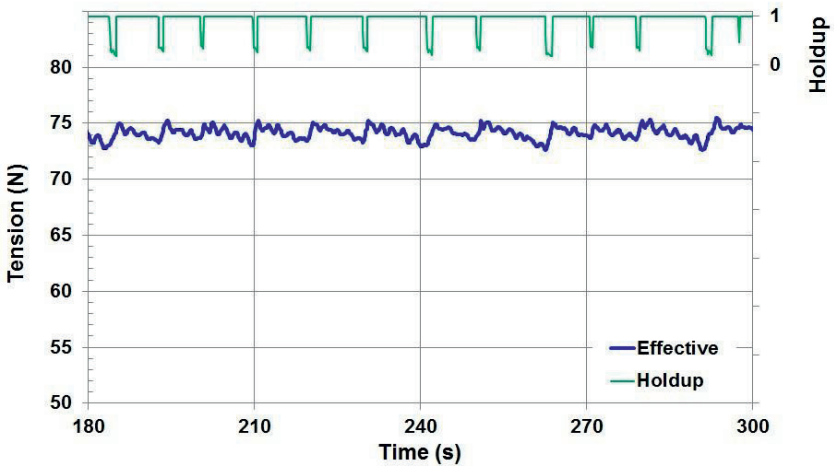

Figure 86. Time history of the top tension, Usl=0.55 m/s Usg=0.12 m/s, from numerical simulation.

The time history of the true tension at the top of the riser is shown in Figure 87 for the end of the simulation. This tension behavior follows the slug flow development. The true tension increase is due to the change in the two-flow momentum and the variation of the internal pressure generated by the slug flow. There is no influence of the external pressure, as the riser is outside the pool, see Equation (6). Clearly, the presence of slug flow involves an increase in axial stresses.

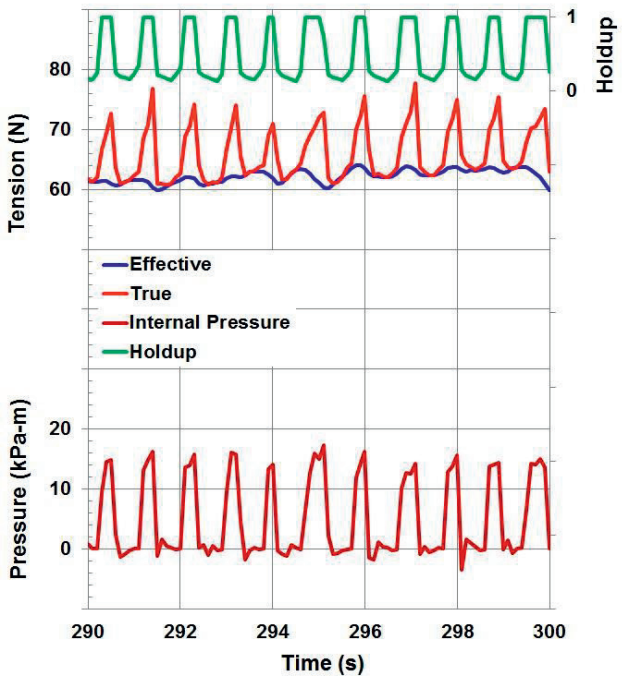

Figure 87. Time history of the true tension at the top.

The interaction between the slug flow and the riser structure generates irregular and variable deformations on the riser along the time domain of the simulation. This behavior is typical of risers with slug flow, as this phenomenon itself has an irregular and unstable behavior. Figure 88 and Figure 89 show the deformation time histories at target point 3 (node 62) of the riser in the *x* direction, normalized by its external diameter, for the numerical simulation and experimental testing, respectively. The oscillations are regarding a new generated equilibrium configuration when the two-phase flow reaches its dynamic steady state. The two graphics present irregular variable deformations as the slugs cross that node. The numerical result predicted slightly smaller deformations than the experimental data and the characteristic frequencies are also slightly different. The calculated average period for the simulation is 2.4 s with a variance of 0.36 s^2, similarly, the experimental data presents an average period equal to 1.7 s with a variance of 0.2 s^2. Based on additional numerical testing using different flow rates, the centripetal forces had more influence than the gravity forces for this riser configuration. Similar behavior was observed for the vertical deformation of the riser, as

shown in Figure 90 and Figure 91 for the numerical and experimental results, respectively.

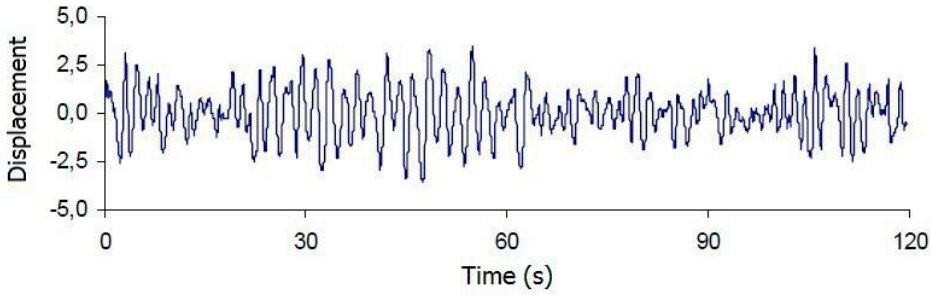

Figure 88. Time history of the ΔX/Do displacements from experimental measurement.

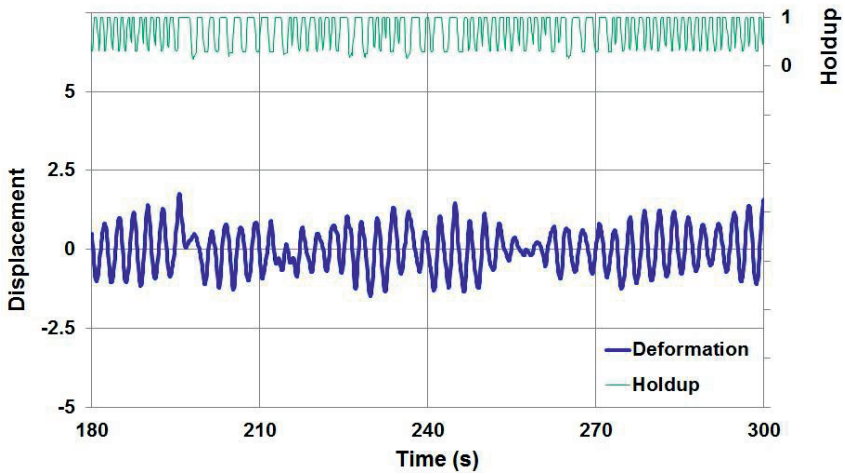

Figure 89. Time history of the ΔX/Do displacements from numerical simulation.

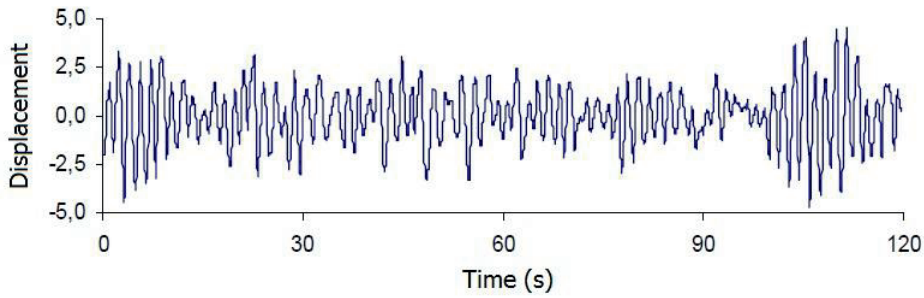

Figure 90. Time history of the ΔY/Do displacements from experimental measurement.

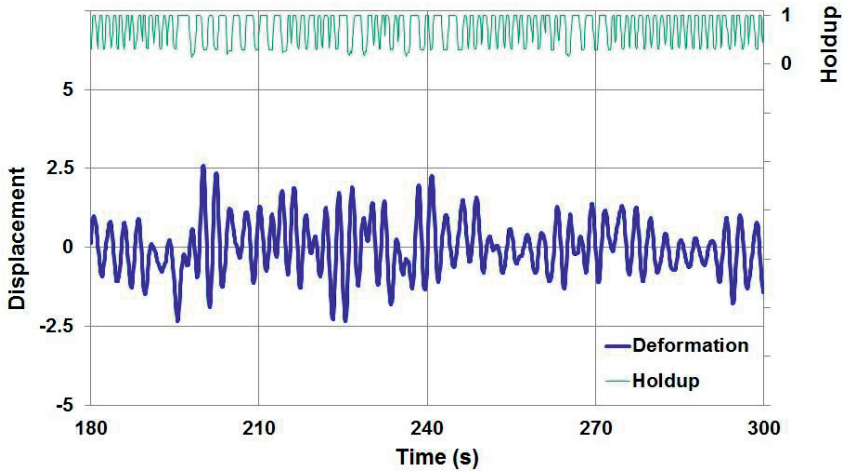

Figure 91. Time history of the ΔY/Do displacements from numerical simulation.

In-plane displacements of node 62 at target point 3 are shown in Figure 92 for the numerical simulation. A deformation into 2.5 times the external diameter was numerically predicted, as reported by Valdivia et al. [5] in its experimental investigation. The oscillation is around the new equilibrium configuration, involving the xy plane.

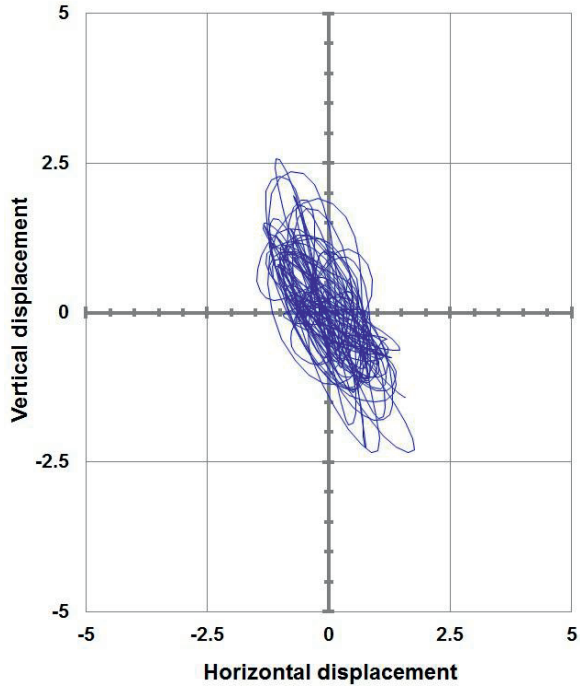

Figure 92. In-plane displacement at target point 3.

As the previous comparisons yielded acceptable agreement, a series of envelope figures are provided from the numerical simulation. The envelope of effective tension is presented in Figure 93. Hydrodynamic slugging traveling through a riser produces a chaotic variation of the effective weight along the structure in time due to the non-homogenous dynamic distribution of the mass flow generated by the series of slugs (the incompressible flow) alternating with the dynamic gas bubbles (the compressible flow). These slugs and bubbles also travel with different velocities. Centripetal forces are generated as the direction of these velocities changes due to the curvature. These centripetal forces work against the riser as centrifugal forces. The whole riser system reacts against these variable loads (weight and centripetal forces), increasing the effective tension. The effective tension variation exerts a strong influence on the riser response.

In this work, due to the presence of the hydrodynamic slugging, the drop in effective tension is increased by 60%. Additionally, it is possible to note a region that does not have variation of effective tension along it. This region, which follows the TDP, becomes tangent to the floor due to the weight of the two-phase flow and the low bending and axial stiffness of the riser model.

The envelope of the true tension distribution predicted by the simulation can be observed in Figure 94. The contribution of the tensions generated by the internal pressure and by the two-phase flow momentum in the increment of the true tension is very significant, see Equation (6). The result shown in this figure demonstrates that the slug flow produced an increase in the axial stresses of the riser of approximately 100%.

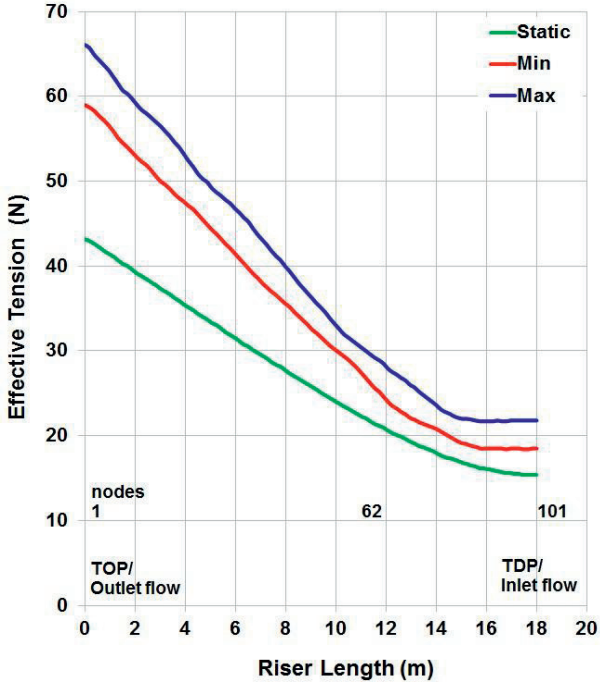

Figure 93. Envelope of the effective tension recorded during time integration.

Figure 95 presents the envelope of the bending moment distribution. The simulation predicted an increase in the maximum value of the bending moment of more than 100%. The highest bending moment is located close to the new TDP, as a region of the riser lies down due to the slug flow. Clearly, the slug flow produces a high variation in bending stresses.

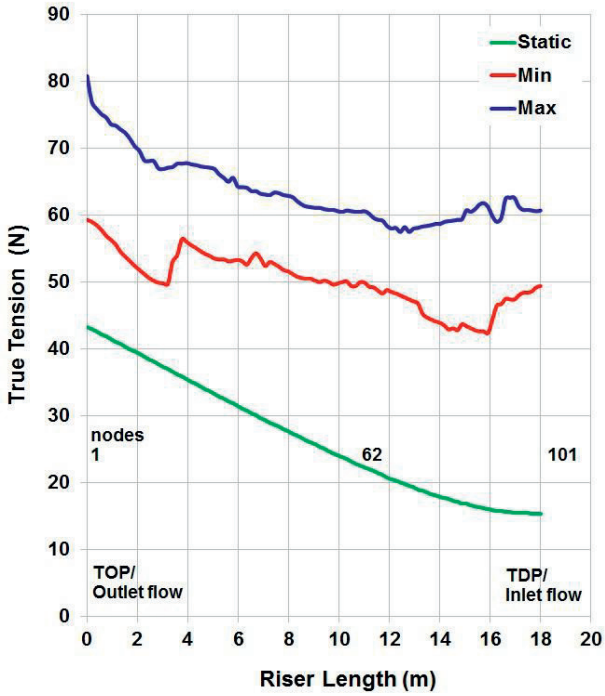

Figure 94. Envelope of the true tension recorded during time integration.

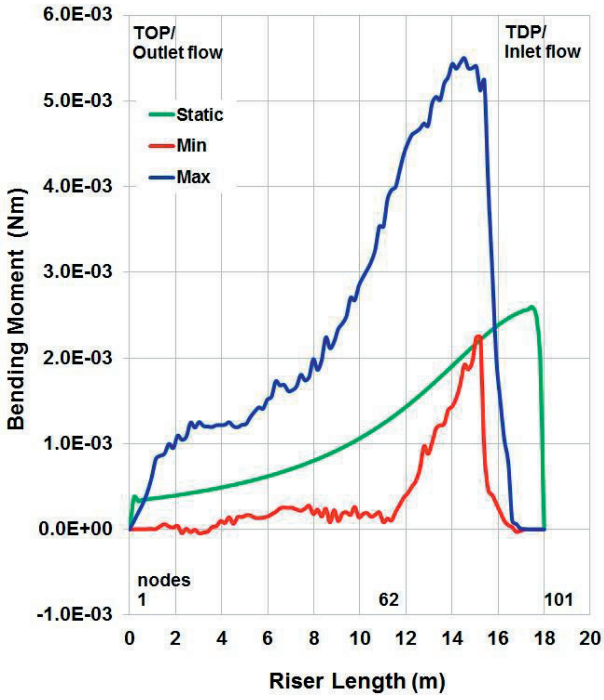

Figure 95. Envelope of the bending moment recorded during time integration.

Figure 96 and Figure 97 show the envelopes of the horizontal and vertical displacements along the riser, respectively. The largest displacements were generated close to target point 3. The riser geometry and the selected flow rate created the conditions for random slug flow, so the two-phase flow generated strong centrifugal forces against the riser. The centripetal forces are seen to dominate over the gravity forces on the generation of oscillations for this experiment. The gravity forces did not have a large influence on the vibrations due to the high frequency of slugs presented. This high slug frequency prevented the recovery of the riser deformation due to the slug weight. An in-plane view of the global riser deformation is shown in Figure 98.

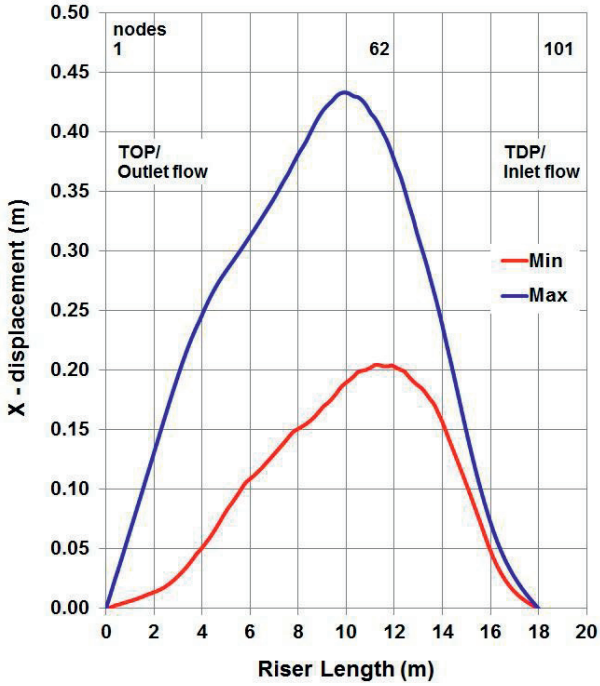

Figure 96. Envelope of the horizontal displacement recorded during time integration.

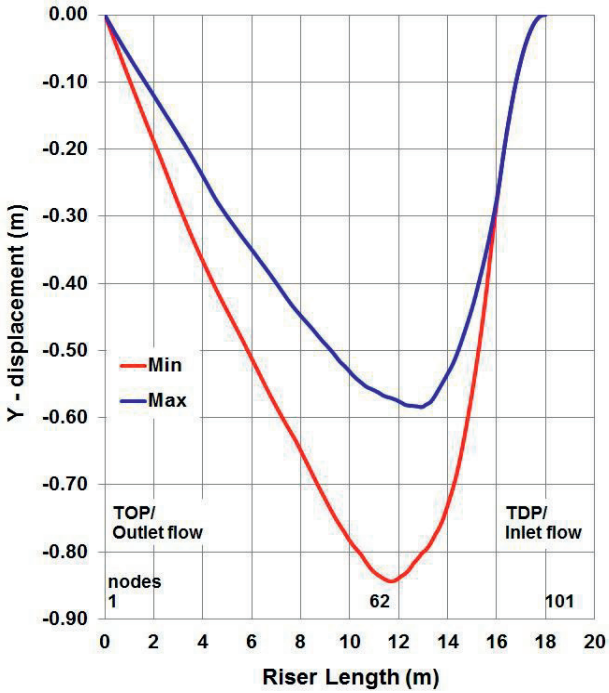

Figure 97. Envelope of the vertical displacement recorded during time integration.

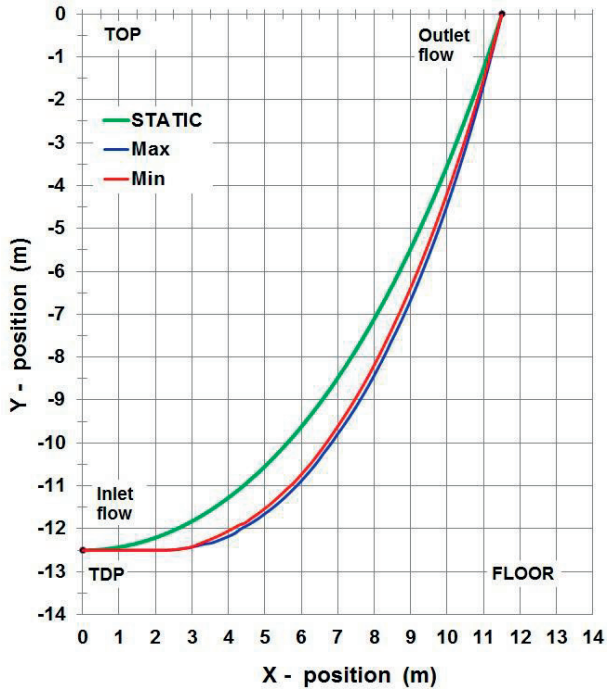

Figure 98. In-plane view of the global riser deformation.

It is obvious that the slug flow – riser dynamics interaction is a complex phenomenon. The two-phase flow development is influenced by the riser response, and the external loads generated by the slug flow depend on the two-phase flow development.

7.3.4 Discussion

Validations of the top tension variation and horizontal/vertical time-dependent deformation are presented. The numerical results present acceptable agreement with the experimental data. Given that agreement, a series of envelopes of effective and true tensions, bending moment and riser deformation are also presented, which allow us to better understand the phenomenon of slug flow - riser dynamics interaction. The influence of slug flow on the riser is mainly due to the centripetal force originated by the change in direction of the fluid particles and the time variable effective weight. On the other hand, the influence of the riser dynamics on the two-phase flow is due to the time variable geometrical profile of the riser. The dynamic riser shape is seen to directly influence the two-phase flow momentum.

The presence of slug flow through a flexible riser means an additional increase of stresses. These stresses can be quantified by the increase in true tension and bending moment. In this work, a considerable increase in true tension and bending moment are predicted.

8. Conclusion and further work

8.1 Main Conclusions

The goal of this work has been to develop an integrated model for simulating the behavior of slug flow – riser dynamics interaction. This has been achieved by using two *in-house* research codes, one for the transient slug flow and another for the global riser dynamic response. The programs were coupled, maintaining them as independent systems but interconnected by mutual information feedback. Two highly non-linear systems were possible to couple using this methodology.

This work also presents an innovative analysis technique in which each phenomenon (slug flow and riser dynamics) is simulated by an independent stand-alone program. Thus, each computer code can continue its own development and improvement independent of the other program.

In this thesis, three basic test cases were examined. The first case illustrates the influence of an internal unsteady slug flow on the effective tension in the riser. The centripetal force and the effective weight variations caused by the slug flow are seen to produce fluctuations of the effective tension. Variation in the true tension was originated mainly from the slug flow pressure fluctuation with minor influence from the slug flow momentum.

The purpose of the second test case has been to identify the difference between the results from linear and non-linear calculations of the dynamic response in marine risers subjected to internal slug flow. The linear model is valid for small changes of effective tension and geometry. However, slug flow may lead to significant variations. The case study shows that the linear model will under predict the riser response. It is hence recommended to apply a non-linear model for riser dynamics in this type of simulations.

In the last test case, experimental validation of the numerical results for a fluid-structure interaction problem was conducted. The experiment examined a transient slug flow through a catenary riser in a laboratory-scale model. The slug flow induced time-variant loads on the riser from centripetal acceleration and traveling slugs. The response of the riser also influenced the development of the internal two-phase flow. A considerable increase in stress was noted in this test case due to the considerable increase in the true tension and bending moment.

Although this work has attempted to explain the mechanics of the slug flow - riser dynamics interaction, each case/problem should be handled individually because this FSI is highly sensitive to flow rates, fluid physical properties, riser geometrical configuration and material properties (mainly axial and bending stiffness).

8.2 Suggestions for further work

The type of slug flow pattern originating in the tests was random *hydrodynamic slugging*. Investigation of the influence of *severe slugging* is recommended to attempt to generate periodic loads against the riser structure. Furthermore, a stochastic description of slug flow should be developed, and a slug spectrum could be applied in dynamic simulations to provide statistics predictions of fatigue and extreme responses.

Integrated simulation of slug flow and riser dynamics is suggested for other marine riser configurations, i.e., lazy-wave and steep-wave risers. The global configuration will strongly influence the slug flow development, creating conditions for the generation of other types of slug flow, such as *severe slugging*. The significance of slug flow on riser fatigue may also vary from one case to another. Both riser geometry and character of internal flow are of importance. Similar analyses could also be conducted for pipelines on uneven terrain and in free spans.

Oil, gas, water and solid particles are often present in the flow from wells to the production system. Hence, in a real offshore production, a more complex flow might be present. This type of analysis can be performed by improving the present two-phase flow code or replacing it with a more sophisticated commercial program for multiphase flow. It is also of interest to combine forces from slug flow with external hydrodynamic

forces from currents, waves and floater motions and thereby identify the significance of slug flow on the fatigue life of marine risers.

The present models for slug flow and riser dynamics are limited to a two-dimensional geometry of the riser. Both models might be developed to handle three-dimensional cases, which will make it possible to carry out more realistic simulations of risers and jumpers of arbitrary shape and environmental conditions.

Finally it is suggested to include a slug flow model in a general software system for analysis of slender marine structures. Such a system has recently been developed by Marintek in Trondheim with the name SIMO. Software integration of this type will make it easy to carry out combined simulation of internal flow and riser dynamics, and take this effect into account when designing complex riser systems.

Reference

[1] T.S. Yih, P. Griffith, Unsteady momentum fluxes in two-phase flows and the vibration of nuclear reactor components, Report 70318-58, MIT, Cambridge, Massachusetts, 1968.

[2] I.J. Fylling, N. Sødahl, A. Bech, On the effects of slug flow on the dynamic response of flexible risers and submerged hoses, *In: 4th International Conference of Floating Production Systems*, IBC Technical Services, London, UK; 1988.

[3] M.H. Patel, F.B. Seyed, Internal flow induced behaviour of flexible risers, *Engineering Structures* 11 (1989) 266-280.

[4] J.L. Riverin, E. Langre, M.J. Pettigrew, Fluctuating forces caused by internal two-phase flow on bends and tees, *Journal of Sound and Vibration* 298 (2006) 1088-1098.

[5] P.G. Valdivia, Experimental and numerical study of the motion dynamics of a catenary riser considering internal flow, Master in Science dissertation, UNICAMP, Brazil, 2008.

[6] A. Gama, L. Ferreira, P.H. Filho, Experimental study of the measurement of two-phase flow rate using pipe vibration, *In: 20th International Congress of Mechanical Engineering* COBEM2009, Brazil, 2009.

[7] J. Pontaza, R. Menon, Flow-induced vibrations of subsea jumpers due to internal multi-phase flow, *In: 30th International Conference on Ocean, Offshore and Arctic Engineering* OMAE2011, The Netherlands, 2011.

[8] E. Ita, Small scale experiments on severe slugging in flexible risers, Master in Science Dissertation. NTNU, Norway, 2011.

[9] V. Pessanha, T. Netto, P.C. Junior, Experimental study on severe slugging flow induced vibration on pipeline-riser system, Graduation project, UFRJ, Brazil, 2014.

[10] C.M. Larsen, Hydrodynamic loads on slender marine structures, Lecture notes, Norwegian University of Science and Technology, Trondheim, Norway, 2007.

[11] M. Paz, *Structural Dynamic – Theory and Computation,* Editorial Reverte S.A., Barcelona, Spain, 2002.

[12] C.P. Sparks, *Fundamentals of Marine Riser Mechanics – Basic Principles and Simplified Analysis*, PennWell Corp, Tulsa, OK, 2007.

[13] IEEE, IEEE Standard for Modelling and Simulation (M&S) High Level Architecture (HLA) – Framework and Rules, Std 1516, 2010.

[14] IEEE, IEEE Standard for Modelling and Simulation (M&S) High Level Architecture (HLA) – Federate Interface Specification, Std 1516.1, 2010.

[15] IEEE, IEEE Standard for Modelling and Simulation (M&S) High Level Architecture (HLA) – Object Model Template (OMT), Std 1516.2, 2010.

[16] F. Kuhl, R. Weatherly, J. Dahmann, *Creating Computer Simulation Systems – An Introduction to the High Level Architecture*, Prentice Hall, New Jersey, 2000.

[17] Pitch Technologies, Pitch pRTI^{TM} Evolved User's Guide, 2010.

[18] J. Kjølaas, Plug propagation in multiphase pipelines, PhD thesis, NTNU, Norway, 2007.

[19] M.A. Crisfield, *Non-linear Finite Element Analysis of Solids and Structures - Vol 1*, John Wiley & Sons Ltd., Chichester, England, 1991.

[20] C.A. Arnholm, Mixed Language Programming Using C++ and FORTRAN 77, <http://arnholm.org/software/cppf77/cppf77.htm>, 1997 (visited February 22, 2012).

[21] J. Searle, J. Brennan, General Interoperability Concepts. In Integration of Modelling and Simulation, pp. 3-1 – 3-8, Educational, Notes RTO-EN-MSG-043bis, Paper 3. Neuilly-sur-Seine, France: RTO, 2007.

[22] R.M. Fujimoto, *Parallel and Distributed Simulation Systems*, Wiley - Interscience Publication, New York, 2000.

[23] R. Courant, K. Friedrichs, H. Lewy, On the partial difference equations of mathematical physics, IBM J. Res. Dev. 11 (1967) 215-234.

[24] A. Ortega, Analysis of slug flow in horizontal pipelines by the two fluid model, Master thesis, PUC-RJ, Brazil, 2004.

Previous PhD theses published at the Department of Marine Technology
(earlier: Faculty of Marine Technology)
NORWEGIAN UNIVERSITY OF SCIENCE AND TECHNOLOGY

Report No.	Author	Title
	Kavlie, Dag	Optimization of Plane Elastic Grillages, 1967
	Hansen, Hans R.	Man-Machine Communication and Data-Storage Methods in Ship Structural Design, 1971
	Gisvold, Kaare M.	A Method for non-linear mixed -integer programming and its Application to Design Problems, 1971
	Lund, Sverre	Tanker Frame Optimalization by means of SUMT-Transformation and Behaviour Models, 1971
	Vinje, Tor	On Vibration of Spherical Shells Interacting with Fluid, 1972
	Lorentz, Jan D.	Tank Arrangement for Crude Oil Carriers in Accordance with the new Anti-Pollution Regulations, 1975
	Carlsen, Carl A.	Computer-Aided Design of Tanker Structures, 1975
	Larsen, Carl M.	Static and Dynamic Analysis of Offshore Pipelines during Installation, 1976
UR-79-01	Brigt Hatlestad, MK	The finite element method used in a fatigue evaluation of fixed offshore platforms. (Dr.Ing. Thesis)
UR-79-02	Erik Pettersen, MK	Analysis and design of cellular structures. (Dr.Ing. Thesis)
UR-79-03	Sverre Valsgård, MK	Finite difference and finite element methods applied to nonlinear analysis of plated structures. (Dr.Ing. Thesis)
UR-79-04	Nils T. Nordsve, MK	Finite element collapse analysis of structural members considering imperfections and stresses due to fabrication. (Dr.Ing. Thesis)
UR-79-05	Ivar J. Fylling, MK	Analysis of towline forces in ocean towing systems. (Dr.Ing. Thesis)
UR-80-06	Nils Sandsmark, MM	Analysis of Stationary and Transient Heat Conduction by the Use of the Finite Element Method. (Dr.Ing. Thesis)
UR-80-09	Sverre Haver, MK	Analysis of uncertainties related to the stochastic modeling of ocean waves. (Dr.Ing. Thesis)
UR-81-15	Odland, Jonas	On the Strength of welded Ring stiffened cylindrical Shells primarily subjected to axial Compression
UR-82-17	Engesvik, Knut	Analysis of Uncertainties in the fatigue Capacity of Welded Joints
UR-82-18	Rye, Henrik	Ocean wave groups
UR-83-30	Eide, Oddvar Inge	On Cumulative Fatigue Damage in Steel Welded Joints
UR-83-33	Mo, Olav	Stochastic Time Domain Analysis of Slender

		Offshore Structures
UR-83-34	Amdahl, Jørgen	Energy absorption in Ship-platform impacts
UR-84-37	Mørch, Morten	Motions and mooring forces of semi submersibles as determined by full-scale measurements and theoretical analysis
UR-84-38	Soares, C. Guedes	Probabilistic models for load effects in ship structures
UR-84-39	Aarsnes, Jan V.	Current forces on ships
UR-84-40	Czujko, Jerzy	Collapse Analysis of Plates subjected to Biaxial Compression and Lateral Load
UR-85-46	Alf G. Engseth, MK	Finite element collapse analysis of tubular steel offshore structures. (Dr.Ing. Thesis)
UR-86-47	Dengody Sheshappa, MP	A Computer Design Model for Optimizing Fishing Vessel Designs Based on Techno-Economic Analysis. (Dr.Ing. Thesis)
UR-86-48	Vidar Aanesland, MH	A Theoretical and Numerical Study of Ship Wave Resistance. (Dr.Ing. Thesis)
UR-86-49	Heinz-Joachim Wessel, MK	Fracture Mechanics Analysis of Crack Growth in Plate Girders. (Dr.Ing. Thesis)
UR-86-50	Jon Taby, MK	Ultimate and Post-ultimate Strength of Dented Tubular Members. (Dr.Ing. Thesis)
UR-86-51	Walter Lian, MH	A Numerical Study of Two-Dimensional Separated Flow Past Bluff Bodies at Moderate KC-Numbers. (Dr.Ing. Thesis)
UR-86-52	Bjørn Sortland, MH	Force Measurements in Oscillating Flow on Ship Sections and Circular Cylinders in a U-Tube Water Tank. (Dr.Ing. Thesis)
UR-86-53	Kurt Strand, MM	A System Dynamic Approach to One-dimensional Fluid Flow. (Dr.Ing. Thesis)
UR-86-54	Arne Edvin Løken, MH	Three Dimensional Second Order Hydrodynamic Effects on Ocean Structures in Waves. (Dr.Ing. Thesis)
UR-86-55	Sigurd Falch, MH	A Numerical Study of Slamming of Two-Dimensional Bodies. (Dr.Ing. Thesis)
UR-87-56	Arne Braathen, MH	Application of a Vortex Tracking Method to the Prediction of Roll Damping of a Two-Dimension Floating Body. (Dr.Ing. Thesis)
UR-87-57	Bernt Leira, MK	Gaussian Vector Processes for Reliability Analysis involving Wave-Induced Load Effects. (Dr.Ing. Thesis)
UR-87-58	Magnus Småvik, MM	Thermal Load and Process Characteristics in a Two-Stroke Diesel Engine with Thermal Barriers (in Norwegian). (Dr.Ing. Thesis)
MTA-88-59	Bernt Arild Bremdal, MP	An Investigation of Marine Installation Processes – A Knowledge - Based Planning Approach. (Dr.Ing. Thesis)
MTA-88-60	Xu Jun, MK	Non-linear Dynamic Analysis of Space-framed Offshore Structures. (Dr.Ing. Thesis)

MTA-89-61	Gang Miao, MH	Hydrodynamic Forces and Dynamic Responses of Circular Cylinders in Wave Zones. (Dr.Ing. Thesis)
MTA-89-62	Martin Greenhow, MH	Linear and Non-Linear Studies of Waves and Floating Bodies. Part I and Part II. (Dr.Techn. Thesis)
MTA-89-63	Chang Li, MH	Force Coefficients of Spheres and Cubes in Oscillatory Flow with and without Current. (Dr.Ing. Thesis
MTA-89-64	Hu Ying, MP	A Study of Marketing and Design in Development of Marine Transport Systems. (Dr.Ing. Thesis)
MTA-89-65	Arild Jæger, MH	Seakeeping, Dynamic Stability and Performance of a Wedge Shaped Planing Hull. (Dr.Ing. Thesis)
MTA-89-66	Chan Siu Hung, MM	The dynamic characteristics of tilting-pad bearings
MTA-89-67	Kim Wikstrøm, MP	Analysis av projekteringen for ett offshore projekt. (Licenciat-avhandling)
MTA-89-68	Jiao Guoyang, MK	Reliability Analysis of Crack Growth under Random Loading, considering Model Updating. (Dr.Ing. Thesis)
MTA-89-69	Arnt Olufsen, MK	Uncertainty and Reliability Analysis of Fixed Offshore Structures. (Dr.Ing. Thesis)
MTA-89-70	Wu Yu-Lin, MR	System Reliability Analyses of Offshore Structures using improved Truss and Beam Models. (Dr.Ing. Thesis)
MTA-90-71	Jan Roger Hoff, MH	Three-dimensional Green function of a vessel with forward speed in waves. (Dr.Ing. Thesis)
MTA-90-72	Rong Zhao, MH	Slow-Drift Motions of a Moored Two-Dimensional Body in Irregular Waves. (Dr.Ing. Thesis)
MTA-90-73	Atle Minsaas, MP	Economical Risk Analysis. (Dr.Ing. Thesis)
MTA-90-74	Knut-Aril Farnes, MK	Long-term Statistics of Response in Non-linear Marine Structures. (Dr.Ing. Thesis)
MTA-90-75	Torbjørn Sotberg, MK	Application of Reliability Methods for Safety Assessment of Submarine Pipelines. (Dr.Ing. Thesis)
MTA-90-76	Zeuthen, Steffen, MP	SEAMAID. A computational model of the design process in a constraint-based logic programming environment. An example from the offshore domain. (Dr.Ing. Thesis)
MTA-91-77	Haagensen, Sven, MM	Fuel Dependant Cyclic Variability in a Spark Ignition Engine - An Optical Approach. (Dr.Ing. Thesis)
MTA-91-78	Løland, Geir, MH	Current forces on and flow through fish farms. (Dr.Ing. Thesis)
MTA-91-79	Hoen, Christopher, MK	System Identification of Structures Excited by Stochastic Load Processes. (Dr.Ing. Thesis)
MTA-91-80	Haugen, Stein, MK	Probabilistic Evaluation of Frequency of Collision between Ships and Offshore Platforms. (Dr.Ing. Thesis)
MTA-91-81	Sødahl, Nils, MK	Methods for Design and Analysis of Flexible

		Risers. (Dr.Ing. Thesis)
MTA-91-82	Ormberg, Harald, MK	Non-linear Response Analysis of Floating Fish Farm Systems. (Dr.Ing. Thesis)
MTA-91-83	Marley, Mark J., MK	Time Variant Reliability under Fatigue Degradation. (Dr.Ing. Thesis)
MTA-91-84	Krokstad, Jørgen R., MH	Second-order Loads in Multidirectional Seas. (Dr.Ing. Thesis)
MTA-91-85	Molteberg, Gunnar A., MM	The Application of System Identification Techniques to Performance Monitoring of Four Stroke Turbocharged Diesel Engines. (Dr.Ing. Thesis)
MTA-92-86	Mørch, Hans Jørgen Bjelke, MH	Aspects of Hydrofoil Design: with Emphasis on Hydrofoil Interaction in Calm Water. (Dr.Ing. Thesis)
MTA-92-87	Chan Siu Hung, MM	Nonlinear Analysis of Rotordynamic Instabilities in Highspeed Turbomachinery. (Dr.Ing. Thesis)
MTA-92-88	Bessason, Bjarni, MK	Assessment of Earthquake Loading and Response of Seismically Isolated Bridges. (Dr.Ing. Thesis)
MTA-92-89	Langli, Geir, MP	Improving Operational Safety through exploitation of Design Knowledge - an investigation of offshore platform safety. (Dr.Ing. Thesis)
MTA-92-90	Sævik, Svein, MK	On Stresses and Fatigue in Flexible Pipes. (Dr.Ing. Thesis)
MTA-92-91	Ask, Tor Ø., MM	Ignition and Flame Growth in Lean Gas-Air Mixtures. An Experimental Study with a Schlieren System. (Dr.Ing. Thesis)
MTA-86-92	Hessen, Gunnar, MK	Fracture Mechanics Analysis of Stiffened Tubular Members. (Dr.Ing. Thesis)
MTA-93-93	Steinebach, Christian, MM	Knowledge Based Systems for Diagnosis of Rotating Machinery. (Dr.Ing. Thesis)
MTA-93-94	Dalane, Jan Inge, MK	System Reliability in Design and Maintenance of Fixed Offshore Structures. (Dr.Ing. Thesis)
MTA-93-95	Steen, Sverre, MH	Cobblestone Effect on SES. (Dr.Ing. Thesis)
MTA-93-96	Karunakaran, Daniel, MK	Nonlinear Dynamic Response and Reliability Analysis of Drag-dominated Offshore Platforms. (Dr.Ing. Thesis)
MTA-93-97	Hagen, Arnulf, MP	The Framework of a Design Process Language. (Dr.Ing. Thesis)
MTA-93-98	Nordrik, Rune, MM	Investigation of Spark Ignition and Autoignition in Methane and Air Using Computational Fluid Dynamics and Chemical Reaction Kinetics. A Numerical Study of Ignition Processes in Internal Combustion Engines. (Dr.Ing. Thesis)
MTA-94-99	Passano, Elizabeth, MK	Efficient Analysis of Nonlinear Slender Marine Structures. (Dr.Ing. Thesis)
MTA-94-100	Kvålsvold, Jan, MH	Hydroelastic Modelling of Wetdeck Slamming on Multihull Vessels. (Dr.Ing. Thesis)
MTA-94-102	Bech, Sidsel M., MK	Experimental and Numerical Determination of Stiffness and Strength of GRP/PVC Sandwich

		Structures. (Dr.Ing. Thesis)
MTA-95-103	Paulsen, Hallvard, MM	A Study of Transient Jet and Spray using a Schlieren Method and Digital Image Processing. (Dr.Ing. Thesis)
MTA-95-104	Hovde, Geir Olav, MK	Fatigue and Overload Reliability of Offshore Structural Systems, Considering the Effect of Inspection and Repair. (Dr.Ing. Thesis)
MTA-95-105	Wang, Xiaozhi, MK	Reliability Analysis of Production Ships with Emphasis on Load Combination and Ultimate Strength. (Dr.Ing. Thesis)
MTA-95-106	Ulstein, Tore, MH	Nonlinear Effects of a Flexible Stern Seal Bag on Cobblestone Oscillations of an SES. (Dr.Ing. Thesis)
MTA-95-107	Solaas, Frøydis, MH	Analytical and Numerical Studies of Sloshing in Tanks. (Dr.Ing. Thesis)
MTA-95-108	Hellan, Øyvind, MK	Nonlinear Pushover and Cyclic Analyses in Ultimate Limit State Design and Reassessment of Tubular Steel Offshore Structures. (Dr.Ing. Thesis)
MTA-95-109	Hermundstad, Ole A., MK	Theoretical and Experimental Hydroelastic Analysis of High Speed Vessels. (Dr.Ing. Thesis)
MTA-96-110	Bratland, Anne K., MH	Wave-Current Interaction Effects on Large-Volume Bodies in Water of Finite Depth. (Dr.Ing. Thesis)
MTA-96-111	Herfjord, Kjell, MH	A Study of Two-dimensional Separated Flow by a Combination of the Finite Element Method and Navier-Stokes Equations. (Dr.Ing. Thesis)
MTA-96-112	Æsøy, Vilmar, MM	Hot Surface Assisted Compression Ignition in a Direct Injection Natural Gas Engine. (Dr.Ing. Thesis)
MTA-96-113	Eknes, Monika L., MK	Escalation Scenarios Initiated by Gas Explosions on Offshore Installations. (Dr.Ing. Thesis)
MTA-96-114	Erikstad, Stein O., MP	A Decision Support Model for Preliminary Ship Design. (Dr.Ing. Thesis)
MTA-96-115	Pedersen, Egil, MH	A Nautical Study of Towed Marine Seismic Streamer Cable Configurations. (Dr.Ing. Thesis)
MTA-97-116	Moksnes, Paul O., MM	Modelling Two-Phase Thermo-Fluid Systems Using Bond Graphs. (Dr.Ing. Thesis)
MTA-97-117	Halse, Karl H., MK	On Vortex Shedding and Prediction of Vortex-Induced Vibrations of Circular Cylinders. (Dr.Ing. Thesis)
MTA-97-118	Igland, Ragnar T., MK	Reliability Analysis of Pipelines during Laying, considering Ultimate Strength under Combined Loads. (Dr.Ing. Thesis)
MTA-97-119	Pedersen, Hans-P., MP	Levendefiskteknologi for fiskefartøy. (Dr.Ing. Thesis)
MTA-98-120	Vikestad, Kyrre, MK	Multi-Frequency Response of a Cylinder Subjected to Vortex Shedding and Support Motions. (Dr.Ing. Thesis)
MTA-98-121	Azadi, Mohammad R. E., MK	Analysis of Static and Dynamic Pile-Soil-Jacket Behaviour. (Dr.Ing. Thesis)

MTA-98-122	Ulltang, Terje, MP	A Communication Model for Product Information. (Dr.Ing. Thesis)
MTA-98-123	Torbergsen, Erik, MM	Impeller/Diffuser Interaction Forces in Centrifugal Pumps. (Dr.Ing. Thesis)
MTA-98-124	Hansen, Edmond, MH	A Discrete Element Model to Study Marginal Ice Zone Dynamics and the Behaviour of Vessels Moored in Broken Ice. (Dr.Ing. Thesis)
MTA-98-125	Videiro, Paulo M., MK	Reliability Based Design of Marine Structures. (Dr.Ing. Thesis)
MTA-99-126	Mainçon, Philippe, MK	Fatigue Reliability of Long Welds Application to Titanium Risers. (Dr.Ing. Thesis)
MTA-99-127	Haugen, Elin M., MH	Hydroelastic Analysis of Slamming on Stiffened Plates with Application to Catamaran Wetdecks. (Dr.Ing. Thesis)
MTA-99-128	Langhelle, Nina K., MK	Experimental Validation and Calibration of Nonlinear Finite Element Models for Use in Design of Aluminium Structures Exposed to Fire. (Dr.Ing. Thesis)
MTA-99-129	Berstad, Are J., MK	Calculation of Fatigue Damage in Ship Structures. (Dr.Ing. Thesis)
MTA-99-130	Andersen, Trond M., MM	Short Term Maintenance Planning. (Dr.Ing. Thesis)
MTA-99-131	Tveiten, Bård Wathne, MK	Fatigue Assessment of Welded Aluminium Ship Details. (Dr.Ing. Thesis)
MTA-99-132	Søreide, Fredrik, MP	Applications of underwater technology in deep water archaeology. Principles and practice. (Dr.Ing. Thesis)
MTA-99-133	Tønnessen, Rune, MH	A Finite Element Method Applied to Unsteady Viscous Flow Around 2D Blunt Bodies With Sharp Corners. (Dr.Ing. Thesis)
MTA-99-134	Elvekrok, Dag R., MP	Engineering Integration in Field Development Projects in the Norwegian Oil and Gas Industry. The Supplier Management of Norne. (Dr.Ing. Thesis)
MTA-99-135	Fagerholt, Kjetil, MP	Optimeringsbaserte Metoder for Ruteplanlegging innen skipsfart. (Dr.Ing. Thesis)
MTA-99-136	Bysveen, Marie, MM	Visualization in Two Directions on a Dynamic Combustion Rig for Studies of Fuel Quality. (Dr.Ing. Thesis)
MTA-2000-137	Storteig, Eskild, MM	Dynamic characteristics and leakage performance of liquid annular seals in centrifugal pumps. (Dr.Ing. Thesis)
MTA-2000-138	Sagli, Gro, MK	Model uncertainty and simplified estimates of long term extremes of hull girder loads in ships. (Dr.Ing. Thesis)
MTA-2000-139	Tronstad, Harald, MK	Nonlinear analysis and design of cable net structures like fishing gear based on the finite element method. (Dr.Ing. Thesis)
MTA-2000-140	Kroneberg, André, MP	Innovation in shipping by using scenarios. (Dr.Ing. Thesis)
MTA-2000-141	Haslum, Herbjørn Alf, MH	Simplified methods applied to nonlinear motion of

		spar platforms. (Dr.Ing. Thesis)
MTA-2001-142	Samdal, Ole Johan, MM	Modelling of Degradation Mechanisms and Stressor Interaction on Static Mechanical Equipment Residual Lifetime. (Dr.Ing. Thesis)
MTA-2001-143	Baarholm, Rolf Jarle, MH	Theoretical and experimental studies of wave impact underneath decks of offshore platforms. (Dr.Ing. Thesis)
MTA-2001-144	Wang, Lihua, MK	Probabilistic Analysis of Nonlinear Wave-induced Loads on Ships. (Dr.Ing. Thesis)
MTA-2001-145	Kristensen, Odd H. Holt, MK	Ultimate Capacity of Aluminium Plates under Multiple Loads, Considering HAZ Properties. (Dr.Ing. Thesis)
MTA-2001-146	Greco, Marilena, MH	A Two-Dimensional Study of Green-Water Loading. (Dr.Ing. Thesis)
MTA-2001-147	Heggelund, Svein E., MK	Calculation of Global Design Loads and Load Effects in Large High Speed Catamarans. (Dr.Ing. Thesis)
MTA-2001-148	Babalola, Olusegun T., MK	Fatigue Strength of Titanium Risers – Defect Sensitivity. (Dr.Ing. Thesis)
MTA-2001-149	Mohammed, Abuu K., MK	Nonlinear Shell Finite Elements for Ultimate Strength and Collapse Analysis of Ship Structures. (Dr.Ing. Thesis)
MTA-2002-150	Holmedal, Lars E., MH	Wave-current interactions in the vicinity of the sea bed. (Dr.Ing. Thesis)
MTA-2002-151	Rognebakke, Olav F., MH	Sloshing in rectangular tanks and interaction with ship motions. (Dr.Ing. Thesis)
MTA-2002-152	Lader, Pål Furset, MH	Geometry and Kinematics of Breaking Waves. (Dr.Ing. Thesis)
MTA-2002-153	Yang, Qinzheng, MH	Wash and wave resistance of ships in finite water depth. (Dr.Ing. Thesis)
MTA-2002-154	Melhus, Øyvin, MM	Utilization of VOC in Diesel Engines. Ignition and combustion of VOC released by crude oil tankers. (Dr.Ing. Thesis)
MTA-2002-155	Ronæss, Marit, MH	Wave Induced Motions of Two Ships Advancing on Parallel Course. (Dr.Ing. Thesis)
MTA-2002-156	Økland, Ole D., MK	Numerical and experimental investigation of whipping in twin hull vessels exposed to severe wet deck slamming. (Dr.Ing. Thesis)
MTA-2002-157	Ge, Chunhua, MK	Global Hydroelastic Response of Catamarans due to Wet Deck Slamming. (Dr.Ing. Thesis)
MTA-2002-158	Byklum, Eirik, MK	Nonlinear Shell Finite Elements for Ultimate Strength and Collapse Analysis of Ship Structures. (Dr.Ing. Thesis)
IMT-2003-1	Chen, Haibo, MK	Probabilistic Evaluation of FPSO-Tanker Collision in Tandem Offloading Operation. (Dr.Ing. Thesis)
IMT-2003-2	Skaugset, Kjetil Bjørn, MK	On the Suppression of Vortex Induced Vibrations of Circular Cylinders by Radial Water Jets. (Dr.Ing. Thesis)
IMT-	Chezhian, Muthu	Three-Dimensional Analysis of Slamming. (Dr.Ing.

2003-3		Thesis)
IMT-2003-4	Buhaug, Øyvind	Deposit Formation on Cylinder Liner Surfaces in Medium Speed Engines. (Dr.Ing. Thesis)
IMT-2003-5	Tregde, Vidar	Aspects of Ship Design: Optimization of Aft Hull with Inverse Geometry Design. (Dr.Ing. Thesis)
IMT-2003-6	Wist, Hanne Therese	Statistical Properties of Successive Ocean Wave Parameters. (Dr.Ing. Thesis)
IMT-2004-7	Ransau, Samuel	Numerical Methods for Flows with Evolving Interfaces. (Dr.Ing. Thesis)
IMT-2004-8	Soma, Torkel	Blue-Chip or Sub-Standard. A data interrogation approach of identity safety characteristics of shipping organization. (Dr.Ing. Thesis)
IMT-2004-9	Ersdal, Svein	An experimental study of hydrodynamic forces on cylinders and cables in near axial flow. (Dr.Ing. Thesis)
IMT-2005-10	Brodtkorb, Per Andreas	The Probability of Occurrence of Dangerous Wave Situations at Sea. (Dr.Ing. Thesis)
IMT-2005-11	Yttervik, Rune	Ocean current variability in relation to offshore engineering. (Dr.Ing. Thesis)
IMT-2005-12	Fredheim, Arne	Current Forces on Net-Structures. (Dr.Ing. Thesis)
IMT-2005-13	Heggernes, Kjetil	Flow around marine structures. (Dr.Ing. Thesis
IMT-2005-14	Fouques, Sebastien	Lagrangian Modelling of Ocean Surface Waves and Synthetic Aperture Radar Wave Measurements. (Dr.Ing. Thesis)
IMT-2006-15	Holm, Håvard	Numerical calculation of viscous free surface flow around marine structures. (Dr.Ing. Thesis)
IMT-2006-16	Bjørheim, Lars G.	Failure Assessment of Long Through Thickness Fatigue Cracks in Ship Hulls. (Dr.Ing. Thesis)
IMT-2006-17	Hansson, Lisbeth	Safety Management for Prevention of Occupational Accidents. (Dr.Ing. Thesis)
IMT-2006-18	Zhu, Xinying	Application of the CIP Method to Strongly Nonlinear Wave-Body Interaction Problems. (Dr.Ing. Thesis)
IMT-2006-19	Reite, Karl Johan	Modelling and Control of Trawl Systems. (Dr.Ing. Thesis)
IMT-2006-20	Smogeli, Øyvind Notland	Control of Marine Propellers. From Normal to Extreme Conditions. (Dr.Ing. Thesis)
IMT-2007-21	Storhaug, Gaute	Experimental Investigation of Wave Induced Vibrations and Their Effect on the Fatigue Loading of Ships. (Dr.Ing. Thesis)
IMT-2007-22	Sun, Hui	A Boundary Element Method Applied to Strongly Nonlinear Wave-Body Interaction Problems. (PhD Thesis, CeSOS)
IMT-2007-23	Rustad, Anne Marthine	Modelling and Control of Top Tensioned Risers. (PhD Thesis, CeSOS)
IMT-2007-24	Johansen, Vegar	Modelling flexible slender system for real-time simulations and control applications

IMT-2007-25	Wroldsen, Anders Sunde	Modelling and control of tensegrity structures. (PhD Thesis, CeSOS)
IMT-2007-26	Aronsen, Kristoffer Høye	An experimental investigation of in-line and combined inline and cross flow vortex induced vibrations. (Dr. avhandling, IMT)
IMT-2007-27	Gao, Zhen	Stochastic Response Analysis of Mooring Systems with Emphasis on Frequency-domain Analysis of Fatigue due to Wide-band Response Processes (PhD Thesis, CeSOS)
IMT-2007-28	Thorstensen, Tom Anders	Lifetime Profit Modelling of Ageing Systems Utilizing Information about Technical Condition. (Dr.ing. thesis, IMT)
IMT-2008-29	Refsnes, Jon Erling Gorset	Nonlinear Model-Based Control of Slender Body AUVs (PhD Thesis, IMT)
IMT-2008-30	Berntsen, Per Ivar B.	Structural Reliability Based Position Mooring. (PhD-Thesis, IMT)
IMT-2008-31	Ye, Naiquan	Fatigue Assessment of Aluminium Welded Box-stiffener Joints in Ships (Dr.ing. thesis, IMT)
IMT-2008-32	Radan, Damir	Integrated Control of Marine Electrical Power Systems. (PhD-Thesis, IMT)
IMT-2008-33	Thomassen, Paul	Methods for Dynamic Response Analysis and Fatigue Life Estimation of Floating Fish Cages. (Dr.ing. thesis, IMT)
IMT-2008-34	Pákozdi, Csaba	A Smoothed Particle Hydrodynamics Study of Two-dimensional Nonlinear Sloshing in Rectangular Tanks. (Dr.ing.thesis, IMT/ CeSOS)
IMT-2007-35	Grytøyr, Guttorm	A Higher-Order Boundary Element Method and Applications to Marine Hydrodynamics. (Dr.ing.thesis, IMT)
IMT-2008-36	Drummen, Ingo	Experimental and Numerical Investigation of Nonlinear Wave-Induced Load Effects in Containerships considering Hydroelasticity. (PhD thesis, CeSOS)
IMT-2008-37	Skejic, Renato	Maneuvering and Seakeeping of a Singel Ship and of Two Ships in Interaction. (PhD-Thesis, CeSOS)
IMT-2008-38	Harlem, Alf	An Age-Based Replacement Model for Repairable Systems with Attention to High-Speed Marine Diesel Engines. (PhD-Thesis, IMT)
IMT-2008-39	Alsos, Hagbart S.	Ship Grounding. Analysis of Ductile Fracture, Bottom Damage and Hull Girder Response. (PhD-thesis, IMT)
IMT-2008-40	Graczyk, Mateusz	Experimental Investigation of Sloshing Loading and Load Effects in Membrane LNG Tanks Subjected to Random Excitation. (PhD-thesis, CeSOS)
IMT-2008-41	Taghipour, Reza	Efficient Prediction of Dynamic Response for Flexible amd Multi-body Marine Structures. (PhD-thesis, CeSOS)
IMT-2008-42	Ruth, Eivind	Propulsion control and thrust allocation on marine vessels. (PhD thesis, CeSOS)
IMT-2008-43	Nystad, Bent Helge	Technical Condition Indexes and Remaining Useful

		Life of Aggregated Systems. PhD thesis, IMT
IMT-2008-44	Soni, Prashant Kumar	Hydrodynamic Coefficients for Vortex Induced Vibrations of Flexible Beams, PhD thesis, CeSOS
IMT-2009-45	Amlashi, Hadi K.K.	Ultimate Strength and Reliability-based Design of Ship Hulls with Emphasis on Combined Global and Local Loads. PhD Thesis, IMT
IMT-2009-46	Pedersen, Tom Arne	Bond Graph Modelling of Marine Power Systems. PhD Thesis, IMT
IMT-2009-47	Kristiansen, Trygve	Two-Dimensional Numerical and Experimental Studies of Piston-Mode Resonance. PhD-Thesis, CeSOS
IMT-2009-48	Ong, Muk Chen	Applications of a Standard High Reynolds Number Model and a Stochastic Scour Prediction Model for Marine Structures. PhD-thesis, IMT
IMT-2009-49	Hong, Lin	Simplified Analysis and Design of Ships subjected to Collision and Grounding. PhD-thesis, IMT
IMT-2009-50	Koushan, Kamran	Vortex Induced Vibrations of Free Span Pipelines, PhD thesis, IMT
IMT-2009-51	Korsvik, Jarl Eirik	Heuristic Methods for Ship Routing and Scheduling. PhD-thesis, IMT
IMT-2009-52	Lee, Jihoon	Experimental Investigation and Numerical in Analyzing the Ocean Current Displacement of Longlines. Ph.d.-Thesis, IMT.
IMT-2009-53	Vestbøstad, Tone Gran	A Numerical Study of Wave-in-Deck Impact usin a Two-Dimensional Constrained Interpolation Profile Method, Ph.d.thesis, CeSOS.
IMT-2009-54	Bruun, Kristine	Bond Graph Modelling of Fuel Cells for Marine Power Plants. Ph.d.-thesis, IMT
IMT 2009-55	Holstad, Anders	Numerical Investigation of Turbulence in a Sekwed Three-Dimensional Channel Flow, Ph.d.-thesis, IMT.
IMT 2009-56	Ayala-Uraga, Efren	Reliability-Based Assessment of Deteriorating Ship-shaped Offshore Structures, Ph.d.-thesis, IMT
IMT 2009-57	Kong, Xiangjun	A Numerical Study of a Damaged Ship in Beam Sea Waves. Ph.d.-thesis, IMT/CeSOS.
IMT 2010-58	Kristiansen, David	Wave Induced Effects on Floaters of Aquaculture Plants, Ph.d.-thesis, CeSOS.
IMT 2010-59	Ludvigsen, Martin	An ROV-Toolbox for Optical and Acoustic Scientific Seabed Investigation. Ph.d.-thesis IMT.
IMT 2010-60	Hals, Jørgen	Modelling and Phase Control of Wave-Energy Converters. Ph.d.thesis, CeSOS.
IMT 2010- 61	Shu, Zhi	Uncertainty Assessment of Wave Loads and Ultimate Strength of Tankers and Bulk Carriers in a Reliability Framework. Ph.d. Thesis, IMT/ CeSOS
IMT 2010-62	Shao, Yanlin	Numerical Potential-Flow Studies on Weakly-Nonlinear Wave-Body Interactions with/without Small Forward Speed, Ph.d.thesis,CeSOS.
IMT 2010-63	Califano, Andrea	Dynamic Loads on Marine Propellers due to Intermittent Ventilation. Ph.d.thesis, IMT.

IMT 2010-64	El Khoury, George	Numerical Simulations of Massively Separated Turbulent Flows, Ph.d.-thesis, IMT
IMT 2010-65	Seim, Knut Sponheim	Mixing Process in Dense Overflows with Emphasis on the Faroe Bank Channel Overflow. Ph.d.thesis, IMT
IMT 2010-66	Jia, Huirong	Structural Analysis of Intect and Damaged Ships in a Collission Risk Analysis Perspective. Ph.d.thesis CeSoS.
IMT 2010-67	Jiao, Linlin	Wave-Induced Effects on a Pontoon-type Very Large Floating Structures (VLFS). Ph.D.-thesis, CeSOS.
IMT 2010-68	Abrahamsen, Bjørn Christian	Sloshing Induced Tank Roof with Entrapped Air Pocket. Ph.d.thesis, CeSOS.
IMT 2011-69	Karimirad, Madjid	Stochastic Dynamic Response Analysis of Spar-Type Wind Turbines with Catenary or Taut Mooring Systems. Ph.d.-thesis, CeSOS.
IMT - 2011-70	Erlend Meland	Condition Monitoring of Safety Critical Valves. Ph.d.-thesis, IMT.
IMT – 2011-71	Yang, Limin	Stochastic Dynamic System Analysis of Wave Energy Converter with Hydraulic Power Take-Off, with Particular Reference to Wear Damage Analysis, Ph.d. Thesis, CeSOS.
IMT – 2011-72	Visscher, Jan	Application of Particla Image Velocimetry on Turbulent Marine Flows, Ph.d.Thesis, IMT.
IMT – 2011-73	Su, Biao	Numerical Predictions of Global and Local Ice Loads on Ships. Ph.d.Thesis, CeSOS.
IMT – 2011-74	Liu, Zhenhui	Analytical and Numerical Analysis of Iceberg Collision with Ship Structures. Ph.d.Thesis, IMT.
IMT – 2011-75	Aarsæther, Karl Gunnar	Modeling and Analysis of Ship Traffic by Observation and Numerical Simulation. Ph.d.Thesis, IMT.
IMT – 2011-76	Wu, Jie	Hydrodynamic Force Identification from Stochastic Vortex Induced Vibration Experiments with Slender Beams. Ph.d.Thesis, IMT.
IMT – 2011-77	Amini, Hamid	Azimuth Propulsors in Off-design Conditions. Ph.d.Thesis, IMT.
IMT – 2011-78	Nguyen, Tan-Hoi	Toward a System of Real-Time Prediction and Monitoring of Bottom Damage Conditions During Ship Grounding. Ph.d.thesis, IMT.
IMT- 2011-79	Tavakoli, Mohammad T.	Assessment of Oil Spill in Ship Collision and Grounding, Ph.d.thesis, IMT.
IMT- 2011-80	Guo, Bingjie	Numerical and Experimental Investigation of Added Resistance in Waves. Ph.d.Thesis, IMT.
IMT- 2011-81	Chen, Qiaofeng	Ultimate Strength of Aluminium Panels, considering HAZ Effects, IMT
IMT- 2012-82	Kota, Ravikiran S.	Wave Loads on Decks of Offshore Structures in Random Seas, CeSOS.

IMT-2012-83	Sten, Ronny	Dynamic Simulation of Deep Water Drilling Risers with Heave Compensating System, IMT.
IMT-2012-84	Berle, Øyvind	Risk and resilience in global maritime supply chains, IMT.
IMT-2012-85	Fang, Shaoji	Fault Tolerant Position Mooring Control Based on Structural Reliability, CeSOS.
IMT-2012-86	You, Jikun	Numerical studies on wave forces and moored ship motions in intermediate and shallow water, CeSOS.
IMT-2012-87	Xiang ,Xu	Maneuvering of two interacting ships in waves, CeSOS
IMT-2012-88	Dong, Wenbin	Time-domain fatigue response and reliability analysis of offshore wind turbines with emphasis on welded tubular joints and gear components, CeSOS
IMT-2012-89	Zhu, Suji	Investigation of Wave-Induced Nonlinear Load Effects in Open Ships considering Hull Girder Vibrations in Bending and Torsion, CeSOS
IMT-2012-90	Zhou, Li	Numerical and Experimental Investigation of Station-keeping in Level Ice, CeSOS
IMT-2012-91	Ushakov, Sergey	Particulate matter emission characteristics from diesel engines operating on conventional and alternative marine fuels, IMT
IMT-2013-1	Yin, Decao	Experimental and Numerical Analysis of Combined In-line and Cross-flow Vortex Induced Vibrations, CeSOS
IMT-2013-2	Kurniawan, Adi	Modelling and geometry optimisation of wave energy converters, CeSOS
IMT-2013-3	Al Ryati, Nabil	Technical condition indexes doe auxiliary marine diesel engines, IMT
IMT-2013-4	Firoozkoohi, Reza	Experimental, numerical and analytical investigation of the effect of screens on sloshing, CeSOS
IMT-2013-5	Ommani, Babak	Potential-Flow Predictions of a Semi-Displacement Vessel Including Applications to Calm Water Broaching, CeSOS
IMT-2013-6	Xing, Yihan	Modelling and analysis of the gearbox in a floating spar-type wind turbine, CeSOS
IMT-7-2013	Balland, Océane	Optimization models for reducing air emissions from ships, IMT
IMT-8-2013	Yang, Dan	Transitional wake flow behind an inclined flat plate: Computation and analysis, IMT
IMT-9-2013	Abdillah, Suyuthi	Prediction of Extreme Loads and Fatigue Damage for a Ship Hull due to Ice Action, IMT
IMT-10-2013	Ramírez, Pedro Agustín Pérez	Ageing management and life extension of technical systems: Concepts and methods applied to oil and gas facilities, IMT
IMT-11-2013	Chuang, Zhenju	Experimental and Numerical Investigation of Speed Loss due to Seakeeping and Maneuvering. IMT

IMT-12-2013	Etemaddar, Mahmoud	Load and Response Analysis of Wind Turbines under Atmospheric Icing and Controller System Faults with Emphasis on Spar Type Floating Wind Turbines, IMT
IMT-13-2013	Lindstad, Haakon	Strategies and measures for reducing maritime CO2 emissions, IMT
IMT-14-2013	Haris, Sabril	Damage interaction analysis of ship collisions, IMT
IMT-15-2013	Shainee, Mohamed	Conceptual Design, Numerical and Experimental Investigation of a SPM Cage Concept for Offshore Mariculture, IMT
IMT-16-2013	Gansel, Lars	Flow past porous cylinders and effects of biofouling and fish behavior on the flow in and around Atlantic salmon net cages, IMT
IMT-17-2013	Gaspar, Henrique	Handling Aspects of Complexity in Conceptual Ship Design, IMT
IMT-18-2013	Thys, Maxime	Theoretical and Experimental Investigation of a Free Running Fishing Vessel at Small Frequency of Encounter, CeSOS
IMT-19-2013	Aglen, Ida	VIV in Free Spanning Pipelines, CeSOS
IMT-1-2014	Song, An	Theoretical and experimental studies of wave diffraction and radiation loads on a horizontally submerged perforated plate, CeSOS
IMT-2-2014	Rogne, Øyvind Ygre	Numerical and Experimental Investigation of a Hinged 5-body Wave Energy Converter, CeSOS
IMT-3-2014	Dai, Lijuan	Safe and efficient operation and maintenance of offshore wind farms ,IMT
IMT-4-2014	Bachynski, Erin Elizabeth	Design and Dynamic Analysis of Tension Leg Platform Wind Turbines, CeSOS
IMT-5-2014	Wang, Jingbo	Water Entry of Freefall Wedged – Wedge motions and Cavity Dynamics, CeSOS
IMT-6-2014	Kim, Ekaterina	Experimental and numerical studies related to the coupled behavior of ice mass and steel structures during accidental collisions, IMT
IMT-7-2014	Tan, Xiang	Numerical investigation of ship's Continuous-Mode Icebreaking in Level Ice, CeSOS
IMT-8-2014	Muliawan, Made Jaya	Design and Analysis of Combined Floating Wave and Wind Power Facilities, with Emphasis on Extreme Load Effects of the Mooring System, CeSOS
IMT-9-2014	Jiang, Zhiyu	Long-term response analysis of wind turbines with an emphasis on fault and shutdown conditions, IMT
IMT-10-2014	Dukan, Fredrik	ROV Motion Control Systems, IMT
IMT-11-2014	Grimsmo, Nils I.	Dynamic simulations of hydraulic cylinder for heave compensation of deep water drilling risers, IMT
IMT-12-2014	Kvittem, Marit I.	Modelling and response analysis for fatigue design of a semisubmersible wind turbine, CeSOS
IMT-13-2014	Akhtar, Juned	The Effects of Human Fatigue on Risk at Sea, IMT

IMT-14-2014	Syahroni, Nur	Fatigue Assessment of Welded Joints Taking into Account Effects of Residual Stress, IMT
IMT-1-2015	Bøckmann, Eirik	Wave Propulsion of ships, IMT
IMT-2-2015	Wang, Kai	Modelling and dynamic analysis of a semi-submersible floating vertical axis wind turbine, CeSOS
IMT-3-2015	Fredriksen, Arnt Gunvald	A numerical and experimental study of a two-dimensional body with moonpool in waves and current, CeSOS
IMT-4-2015	Jose Patricio Gallardo Canabes	Numerical studies of viscous flow around bluff bodies, IMT
IMT-5-2015	Vegard Longva	Formulation and application of finite element techniques for slender marine structures subjected to contact interactions, IMT
IMT-6-2015	Jacobus De Vaal	Aerodynamic modelling of floating wind turbines, CeSOS
IMT-7-2015	Fachri Nasution	Fatigue Performance of Copper Power Conductors, IMT
IMT-8-2015	Oleh I Karpa	Development of bivariate extreme value distributions for applications in marine technology, CeSOS
IMT-9-2015	Daniel de Almeida Fernandes	An output feedback motion control system for ROVs, AMOS
IMT-10-2015	Bo Zhao	Particle Filter for Fault Diagnosis: Application to Dynamic Positioning Vessel and Underwater Robotics, CeSOS
IMT-11-2015	Wenting Zhu	Impact of emission allocation in maritime transportation, IMT
IMT-12-2015	Amir Rasekhi Nejad	Dynamic Analysis and Design of Gearboxes in Offshore Wind Turbines in a Structural Reliability Perspective, CeSOS
IMT-13-2015	Arturo Jesús Ortega Malca	Dynamic Response of Flexibles Risers due to Unsteady Slug Flow, CeSOS